

POLITECNICO DI TORINO

---

DIPARTIMENTO ENERGIA

Corso di Laurea Magistrale in Ingegneria Elettrica

# Tethered UAV

Feasibility study for the propulsion system of a tethered UAV



**POLITECNICO  
DI TORINO**

**Advisor:**

Prof. Fabrizio Dabbene

**Co-Advisors:**

Prof. Giorgio Guglieri

Prof. Liwei Zhang

Dr. Elisabetta Punta

**Candidate:**

Eugenio MERCATALI

---

ACADEMIC YEAR 2018-2019

## **Abstract**

While the UAV market is growing exponentially, new architectures are investigated to overcome limitations of conventional platforms. Tethered UAVs leverage vertical take-off capabilities and flight control flexibility but at the same time eliminate energy restrictions due to battery lifetime. A cable solution is promising as it allows potentially unlimited flight time: vehicles are able to perform longer mission or carry on heavier payloads. These features make tethered UAVs suitable for applications where endurance is key element, such as permanent surveillance, temporary ad-hoc networks, traffic and crowded management and monitoring.

Even though tethered UAV technology is still emerging, some industrial applications are already available in the market. The purpose of this thesis is to design and simulate the power system of a tethered UAV heavier from the one available on the market. As a matter of fact nowadays are developed only lighter solution than the project's one. The main goal is the design, modelling and simulation the propulsion system of the tethered UAV, which comprises the propeller sizing, the electric motor choice and the motor control. In order to reduce time and cost is used MATLAB/Simulink to simulate the motor paired with the propeller.

The model of the propulsion system is implemented in the multicopter dynamic model for a realistic simulation of the UAV behaviour. To estimate the weight of the cable it has to be designed. The cable has to be able to transmit the power required by the vehicle from the ground to the air module. On this operation plays a crucial role the voltage level of power transmission because it affects the cable's weight and the choice of the power converter aboard and on the ground station. Finally safety system design is considered to improve UAV redundancy and to increase the multirotor robustness.

# Contents

<b>List of Tables</b>	5
<b>List of Figures</b>	6
<b>1 Introduction</b>	9
1.1 Tethered UAVs	9
1.2 Industrial Tethered UAVs	11
1.2.1 Zoe	11
1.2.2 Orion	12
1.2.3 XD-motion	12
1.2.4 Watt 200	13
1.2.5 Summary Table	13
1.3 Research Projects	14
1.4 Thesis Objective	16
<b>2 Propeller Choice and Simulation</b>	19
2.1 Blade Element Theory	19
2.1.1 Inflow Factors	21
2.1.2 Axial and Angular Flow Conservation of Momentum	22
2.1.3 Iterative Procedure for Blade Element Theory	22
2.2 Propeller Design	23
2.2.1 Variable Pitch	29
<b>3 Motor Type and Modelling</b>	32
3.1 Motor Type	32
3.2 Brushless DC Motor	35
3.2.1 Stator Cores	35
3.2.2 PM Rotor	36
3.2.3 Position Sensors	36
3.2.4 Drive Mode	37
3.2.5 Mathematical Model	38
3.2.6 Characteristic Analysis	41

<b>4</b>	<b>Simulation for BLDC Motor Drives</b>	<b>44</b>
4.1	Mechanical Model of the Electrical Motor . . . . .	44
4.2	Electromagnetic Model of the Motor . . . . .	45
4.2.1	BEMF Calculation . . . . .	45
4.2.2	Current Calculation . . . . .	47
4.3	Hall Effect Sensor . . . . .	47
4.4	Torque Computation . . . . .	49
4.5	Inverter . . . . .	49
4.6	Simulation Results . . . . .	50
4.6.1	Open Loop . . . . .	50
4.6.2	Characteristic . . . . .	53
4.6.3	Closed Loop with Trapezoidal Control . . . . .	54
4.6.4	Hysteresis Control . . . . .	57
4.7	Result Comparison . . . . .	61
<b>5</b>	<b>Quadcopter Simulation</b>	<b>64</b>
5.1	Notation and Assumptions . . . . .	64
5.2	Model Description . . . . .	65
5.2.1	Autopilot . . . . .	66
5.2.2	Electromechanical Actuators . . . . .	69
5.2.3	Quadcopter dynamics . . . . .	70
5.2.4	Navigation and Sensors . . . . .	71
5.2.5	Tether cable . . . . .	72
5.3	Results . . . . .	72
<b>6</b>	<b>Power Supply System</b>	<b>79</b>
6.1	Voltage Level for Power Transmission . . . . .	79
6.2	On-Off Board Power Electronics . . . . .	80
6.2.1	On Board Power Electronics . . . . .	80
6.2.2	Off-Board Power Electronics . . . . .	82
6.3	Cable Sizing . . . . .	82
<b>7</b>	<b>Safety System</b>	<b>86</b>
7.1	Short-Circuit Protection . . . . .	86
7.1.1	Overload Protection . . . . .	86
7.1.2	Short Circuit Protection . . . . .	88
7.2	Backup Battery Sizing . . . . .	89
<b>8</b>	<b>Conclusions and Future Developments</b>	<b>92</b>
8.1	Thesis Results . . . . .	92
8.2	Future Development . . . . .	93
	<b>Bibliography</b>	<b>94</b>

# List of Tables

2.1	System specifications with T-Motor MF3218 propeller . . . . .	24
2.2	System specs with T-Motor MF3218 . . . . .	25
2.3	System specs with T-Motor P28x8,4” . . . . .	25
2.4	System specs with T-Motor FA36,2x11,8” . . . . .	25
2.5	System specs with T-Motor FA36,2x11,8”, selig airfoils and variable chord	29
4.1	Function of the BEMF in relation to the rotor position . . . . .	46
4.2	Gate state . . . . .	51
5.1	Power results summary . . . . .	74
5.2	Power results summary . . . . .	78
6.1	Electrical and mechanical specifications of BCM6123xD1E5135yzz . .	81
6.2	ESC electrical and mechanical specifications . . . . .	82
6.3	DCDC converter for on-board equipment electrical and mechanical specifications . . . . .	82
6.4	Mechanical and electrical specifications of the cable . . . . .	84

# List of Figures

1.1	Tethered UAV example . . . . .	10
1.2	Zoe tethered drone . . . . .	11
1.3	XD-motion tethered UAV camera . . . . .	12
1.4	Watt 200 tethered drone . . . . .	13
1.5	Power supply system of tethered Hexarotor [1] . . . . .	15
1.6	Power conversion unit proposed for UAV [1] . . . . .	16
2.1	Propeller profile in BET . . . . .	19
2.2	Propeller section in BET . . . . .	20
2.3	Torque comparison of a single motor with three different propellers . . . . .	26
2.4	Comparison between thrust provided from a single motor of the UAV with different propellers . . . . .	26
2.5	Power required by a single motor with different propeller . . . . .	27
2.6	Propeller's airfoils analyzed . . . . .	27
2.7	T-Motor FA36,2x11,8" profile . . . . .	28
2.8	Lift and drag coefficient . . . . .	30
2.9	Thrust generated by the propeller in relation with its pitch and its angular speed . . . . .	31
2.10	Iso-thrust curve at hover and maximum speed changing as the pitch varies . . . . .	31
3.1	Comparison between BLDC and PMSM magnetic induction waveform . . . . .	33
3.2	Comparison between BLDC and PMSM stator windings . . . . .	34
3.3	Cross sectional image of a BLDC . . . . .	36
3.4	Full-bridge driving circuit . . . . .	37
3.5	Equivalent circuit of the BLDC motor . . . . .	40
3.6	Equivalent circuit with two phase exited . . . . .	42
3.7	Mechanical characteristic . . . . .	43
4.1	Motor mechanical model . . . . .	44
4.2	Torque load in relation with propeller pitch and velocity . . . . .	45
4.3	BEMF trends . . . . .	46
4.4	Electrical circuit of the motor . . . . .	47
4.5	Sector evaluation with hall effect sensor . . . . .	48
4.6	Hall effect sensor block . . . . .	48
4.7	Torque computation . . . . .	49

4.8	Inverter block . . . . .	49
4.9	Decoder block . . . . .	50
4.10	Speed response to a step in open loop . . . . .	51
4.11	Torque response to a step in open loop . . . . .	52
4.12	Current response to a step in open loop . . . . .	52
4.13	Mechanical characteristic . . . . .	53
4.14	Speed regulator . . . . .	54
4.15	Speed response to a ramp in closed loop . . . . .	55
4.16	Torque response in closed loop . . . . .	55
4.17	Current response to a ramp . . . . .	56
4.18	Power response to a ramp . . . . .	57
4.19	Reference current . . . . .	58
4.20	Inverter's current and voltage behaviour with an hysteresis regulator . . . . .	58
4.21	Speed response to a ramp in closed loop with hysteresis control . . . . .	59
4.22	Torque response to a ramp in closed loop with hysteresis control . . . . .	60
4.23	Current response to a ramp in closed loop with hysteresis control . . . . .	60
4.24	Power response to a ramp in closed loop with hysteresis control . . . . .	61
4.25	Current comparison with and without hysteresis current regulator . . . . .	62
4.26	Current comparison with and without hysteresis current regulator . . . . .	62
4.27	Current comparison with and without hysteresis current regulator . . . . .	63
4.28	Power comparison with and without hysteresis current regulator . . . . .	63
5.1	Angular speed convention . . . . .	65
5.2	Roll Controller . . . . .	67
5.3	Altitude Controller . . . . .	68
5.4	Forward Controller . . . . .	68
5.5	Single electromechanical actuator . . . . .	70
5.6	Quadcopter behaviour with NED=[0.5,-0.5,-10] input . . . . .	73
5.7	Speed trend with NED=[0.5,-0.5,-10] input . . . . .	74
5.8	Thrust trend with NED=[0.5,-0.5,-10] input . . . . .	75
5.9	Power trend with NED=[0.5,-0.5,-10] input . . . . .	75
5.10	Dynamic response with different NED input . . . . .	76
5.11	Comparison between reference thrust with different desired altitude . . . . .	76
5.12	Comparison between reference speed with different working altitude . . . . .	77
5.13	Comparison between required power with different working altitude . . . . .	77
5.14	Dynamic response to variable NED input . . . . .	78
6.1	Current circulating in the cable with different voltage levels . . . . .	80
6.2	Simplified model of the BCM . . . . .	82
6.3	1B6X1.2 cable section . . . . .	83
7.1	Intervention range of the C curve . . . . .	87
7.2	Position trend from 0m to 100m and from 100m to 0m . . . . .	89
7.3	Power consumption for the landing phase . . . . .	90

# Nomenclature

BET	[-]	Blade Element Theory
$\theta$	[°]	Pitch angle
$V_1$	[m/s]	local flow velocity vector
$V_0$	[m/s]	Axial flow at the propeller disk
$V_2$	[m/s]	Angular flow velocity vector
$\phi$	[°]	Difference between pitch angle and attack angle
$\Delta T$	[N]	Section's thrust
$\Delta Q$	[Nm]	Section's torque
$\Delta L$	[N]	Section's lift
$\Delta D$	[N]	Section's drag
$C_L$	[-]	Lift coefficient
$C_D$	[-]	Drag coefficient
$V_\infty$	[m/s]	Multicopter forward velocity
$\Omega r$	[rad/s]	Blade section's angular speed
$\alpha$	[°]	Angle of attack of the blade section
$\rho$	[kg/m <sup>3</sup> ]	Air density
$V_S$	[m/s]	Slipstream velocity
$a$	[-]	Axial inflow factor
$b$	[-]	Angular inflow factor
$V_{\theta(\text{splitstream})}$	[m/s]	Velocity in the splitstream
$V_{\theta(\text{freestream})}$	[m/s]	Velocity in the freestream
$T_{tot}$	[N]	Total thrust
TRMTOW	[-]	Thrust Ratio at Max Takeoff Weight
$M_{tot}$	[kg]	Total mass

# Chapter 1

## Introduction

### 1.1 Tethered UAVs

Small Unmanned Aerial Vehicles are at the center of research and development in the aircraft environment because of their wide spreading. The exploration of Unmanned Aerial Vehicle (UAV) technology was made for military purposes till late 1990's [2] when it was observed a fast increase in civilian applications, thanks to the advances in avionics system that have allowed a rapid growth in UAV technology.

The increasing demand of UAV system is related to the Vertical Take-Off and Landing (VTOL) capability of the vehicle which make it suitable for several civilian applications. In the UAV's market within the civilian environment, the multirotor aerial vehicles are replacing helicopters. The main reason why multirotor are replacing helicopters are the advantage provided by the multirotors UAVs which are essentially two[3]:

- The easier rotorhead mechanics which results in less maintenance.
- The reduced flight control complexity, in fact the flight control is provided by changing the rotation speed of the rotors.

On the other hand the efficiency of a multicopter is lower than conventional helicopters and this drives to an higher value of energy required. This amount of energy paired with the current batteries available on the market leads to the main limitation of the UAV: the short flight time and the low payload capacity.

Moreover due to the limited energy stored the UAVs have to be quite light and for this reason they are strongly sensitive to the mass fluctuations and wind disturbance, which drives to an hover performance loss [4].

In order to solve these limitations several solutions have been adopted, the simplest is to enhance the energy stored increasing the number of batteries on board.

This solution in particular isn't advantageous because increasing the flight time adding extra battery is in contrast with the objective of augmenting the payload capacity. In fact the extra battery mass leads to a reduction of payload capability.

Some wireless power solution are being studied but they are strongly affected by the low efficiency of the power transmission which is closer to 20% [5].

The solution analyzed in this project is a multicopter UAV tethered with a ground system. The ground system through the tether provides both power to the UAV and fast, secure data transmission. Tethered UAVs allow longer flight time, heavier payload, a reliable high-bandwidth communication channel thanks to optical fiber[6].

Furthermore the tether tension gives a stabilizing action against wind disturbance although it could make more complicated the control of the system[4].

On the other hand, tethered UAVs suffer limited operational range due to the cable con-



Figure 1.1: Tethered UAV example

strain: in fact the maximum operative range is fixed by the length of the cable and the horizontal range is also limited from the obstacles on the terrain that could narrow the tether range or in the worst case could lead to a fault, for example in case of contact with an overhead power line.

On the same time the tether provides a secure link to an immovable object, and prevents the unmanned aircraft from flying away in the event of loss of positive control.

Anyway the tethered solution is suitable for a lot of application both civilian and military in particular:

- Persistent surveillance of large areas with high resolution images.
- Flying relay for cellular signal coverage.

- Industrial monitoring for infrastructures inspections and operations management.

## 1.2 Industrial Tethered UAVs

Tethered UAVs are highly innovative and few industrial applications are today commercially available.

In the followings, a review of market solutions is provided. First of all it must be said that tethered drone technology is not mature so there is not a standardized configuration for the numbers and the kind of propellers; in this section are reported only the most common configurations. .

### 1.2.1 Zoe

Zoe is the first product analyzed which is a quadrotor produced by Acecore Technologies (figure 1.2).

This product allows unlimited flight time thanks to tether which transmits power and



Figure 1.2: Zoe tethered drone

data from the ground. The UAV has a Maximum take-off weight of 9kg and allows a payload up to 3.5kg. Zoe tethered drone solution presents four propeller and it permits to flight at on operating altitude of 80m also with rain and with 20 mph wind eliminating the "fly away potential" thanks to the tether.

About the power its allows continuous power up to 1800W and a temporary power peak up to 2500W for 2s.

Communication between ground and air module are done through ethernet cable at a



Figure 1.3: XD-motion tethered UAV camera

speed of 60Mb/s.

### 1.2.2 Orion

Orion is the second solution analyzed which is a hexarotor provided by Elistair (figure 1.1). This UAV is able to flight for more than 10 hours with an operating altitude of 80m also with 22 mph winds.

It has a total weight of 10.5kg comprehensive of a safety battery and the maximum power absorbed by the drone is 3000W.

### 1.2.3 XD-motion

Third solution analyzed is XD-motion tethered drone (figure 1.3) which is an hexarotor with an integrated camera and it is specialized full HD aerial shooting.

This drone could work for hours at a maximum height of 100m with a payload up to 10kg.

The producer sells together the drone also a motorized winch for rope tension.



Figure 1.4: Watt 200 tethered drone

### 1.2.4 Watt 200

Watt 200 is a octacopter with coaxial propeller produced by Drone Aviation Corp (figure 1.4).

This drone is able to fly for more than 8 hours with a maximum payload of 1.8kg at a maximum altitude of 60m.

### 1.2.5 Summary Table

	Zoe	Orion	XD-motion	Watt 200	
<i>Number of rotors</i>	4	6	6	8	-
<i>Max altitude</i>	100	80	100	60	m
<i>Power</i>	1800	3000	-	-	W
<i>Payload</i>	3.5	-	10	1.8	kg
<i>Output Voltage</i>	21-25	22	-	-	Vdc
<i>Deployment capabilities with wind</i>	34	22	-	20	mph

This four systems presents several advantages respect the typical customer drones:

1. Continuous operation

2. Un-hackable transmission of data
3. Redundant on-board power system
4. Enhance safety due to a link with the earth

## 1.3 Research Projects

On this section the focus is given to academic research on tethered UAV modelling. The literature on the power system of tethered UAV is not very wide but there are some papers about it, that have been read and analyzed.

### **A Micro Unmanned Aerial Vehicle (MUAV) for Rescue Mission**

To solve the short time duration of the usual multicopter the paper [7] proposes a MUAV for rescue mission is analyzed with a tether link between the UAV and an unmanned ground vehicle.

The length of each side of the MUAV is 470mm each side, the weight of the body, is 1140g and the power for hover is 300W.

The corresponding conventional UAV has usually a voltage supply of 12Vdc and a current for hover of 25A.

A lot of importance in the article is given to the cable sizing because it should be not too large in order not to exceed the payload capacity of the drone, but it shouldn't be neither too thin because otherwise the losses, due to Ohm's law, would be too significant. In order to have a light cable and a light air module on the ground system is considered a step-up converter, which reduce the circulating current on the tether allowing thinner cable. Aboard the vehicle the DC/AC transformation is done directly by ESC avoiding the use of a step-down converter that would have further increased the UAV's weight.

For this work a BLDC motor with current vector-drive method was chosen and some experiments were performed to determine the thrust trend in relation to the current, with various supply voltage which vary from 12 to 32 Vdc.

With a force-torque sensor were evaluated the required thrust, the maximum thrust produced by the propulsion system and the motor voltage necessary to obtain a certain thrust. Finally 4 different type of cable were analyzed because of different cable resistivity and density.

The cables have resistivity which varies from 0.015 to 0.03  $\Omega/m$ , line density from 13 to 119  $g/m$  and diameter from AWG16 to AWG20.

The paper shows that with different cables the UAV managed to reach different height and points out that cable weight and resistance really affect the system performance.

## The Power Supply Design and Ground Power Station

Power supply and ground power station design for a tethered hexarotor UAV is presented in [1].

On ground power station are present the following units: power generator or grid, AC/DC conversion unit(230AC to 380 VDC).

On aerial module there are the following unit: DC/DC converter module (380VDC to 48VDC) for brushless DC motors, DC/DC converter module (380VDC to 24VDC) for data acquisition device, DC/DC converter (380VDC to 24Vdc) for autopilot unit, charger unit 48 VDC storage battery used for emergency landing.

Focusing on UAV power conversion in this work is provided a solution to manage

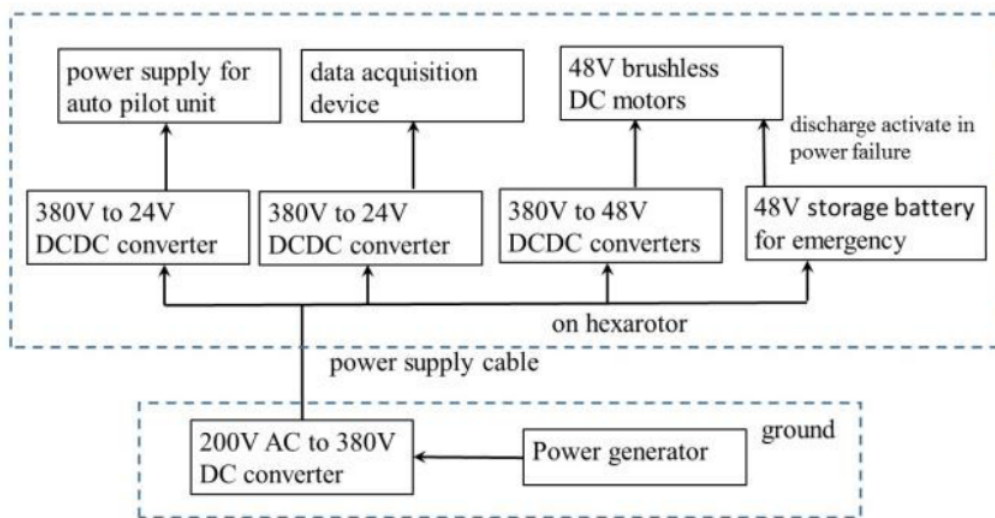


Figure 1.5: Power supply system of tethered Hexarotor [1]

the weight and the current peak of the major part of conversion that is the 380VDC to 48VDC conversion for hexarotors motors.

In fact using the converter unit proposed, which exploit a full parallel configuration of DC/DC converter (figure 1.6), leads to a lighter and more reliable solution than the existing approaches.

## The Motor Design

Motor Design for a large UAV is discussed in [8].

The method plans to first design before the mechanics part and then the electric part.

In the first designing phase it is decided the number of rotors, it is fixed the target weight, after that is estimates the dimension and the material of the body.

Then are designed the propeller and the motor which have to be able to overcome the

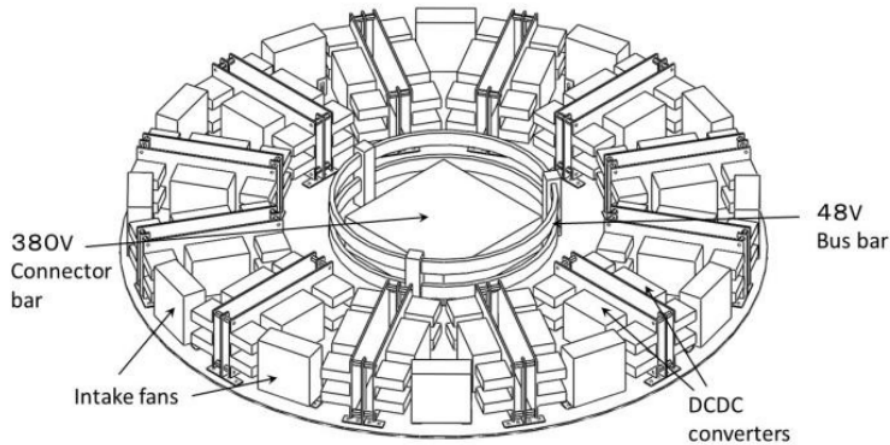


Figure 1.6: Power conversion unit proposed for UAV [1]

force exerted by the UAV weight. The thrust provided by the propeller depends mainly on the propeller diameter, propeller pitch and motor velocity. With this information is chosen the propeller and after a motor which is capable to provide enough torque and enough velocity to the propeller to lift the drone.

On the electric side the first design choice is on power distribution board and secondly the battery is sized.

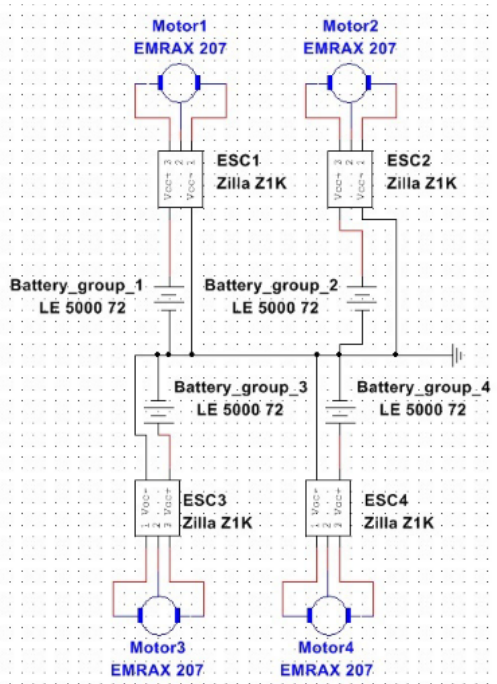
Finally is chosen an ESC which can handle the required voltage of the DC link and the peak current required by the motor. In figure 1.7a and 1.7b are shown the motor power supply schematic and the motor signal schematic of the system realized.

## 1.4 Thesis Objective

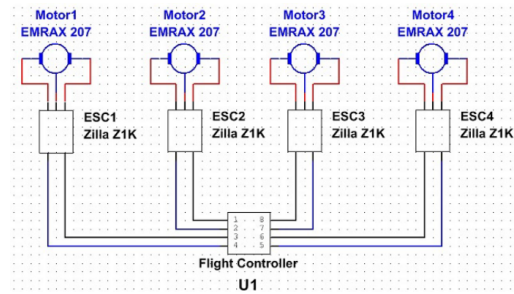
This research is developed as a collaboration between CNR IEIIT, Politecnico di Torino and Beijing Jiatong University.

The project deals with tethered UAV for industrial applications and consists of a feasibility study to design this system with the aim of tackling and overcoming the main limitations of traditional drones, i.e. limited load capacity and limited flight time.

In particular the thesis focuses on the analysis and sizing of the vehicle propulsion system. The propulsion system has to be designed to enable the UAV to hover at the maximum altitude for many hours. So the motors and the propellers must be sized to provide the necessary thrust and power with the appropriate dynamic for this operative condition. Furthermore the power electronic of the ground system and of the air module has to be designed. Crucial point is the voltage value of power transmission, because it affects the losses, the payload value and the on-board/off-board power electronics.



(a) Motor power supply schematic



(b) Motor signal schematic

For safety reason it is also has to be designed the back-up battery and the protection circuitry to guaranteed the security and the operativity of the UAV also in case of fault of the cable or of the supply.

The component of the power system chosen will be simulated and in a second time realized and tested.

<b>Project Overview</b>	<b>Description</b>
<i>Introduction</i>	Project presentation and description of the tethered UAV technology with a focus on industrial tethered UAVs and on research projects.
<i>Propeller choice and simulation</i>	Presentation of the blade element theory, design of the propeller and simulation of its performance.
<i>Motor choice and modelling</i>	Choice of the motor which fits better the project specifications, description of its construction, control features and presentation of its mathematical model.
<i>Motor simulation</i>	Explanation of the model used for the simulations and analysis of its performance.
<i>Quadcopter simulation</i>	Explanation of the quadcopter model and analysis of the system with the addition of electromechanical actuators.
<i>Cable sizing</i>	Analysis of the weight and of the losses of different types of cable with different voltage supply.
<i>Electrical failure analysis</i>	Analysis of the system in case of short circuit and sizing of the back-up battery.
<i>Conclusion and future works</i>	Main results achieved in the thesis, limitation and further developments

## Chapter 2

# Propeller Choice and Simulation

### 2.1 Blade Element Theory

In order to estimate the aerodynamic performance of a UAV propeller the Blade Element Theory (BET) will be implemented .

Through BET it is possible to analyse different kind of propeller and different kind of airfoils for finding the configuration that best meets the needs of the UAV.

Each propeller configuration exerts a different force on the flow-field and different torque at a certain speed.

BET method assumes that the propeller is split into several sections each of width  $dr$  along the radial axe as shown in Figure 2.1.

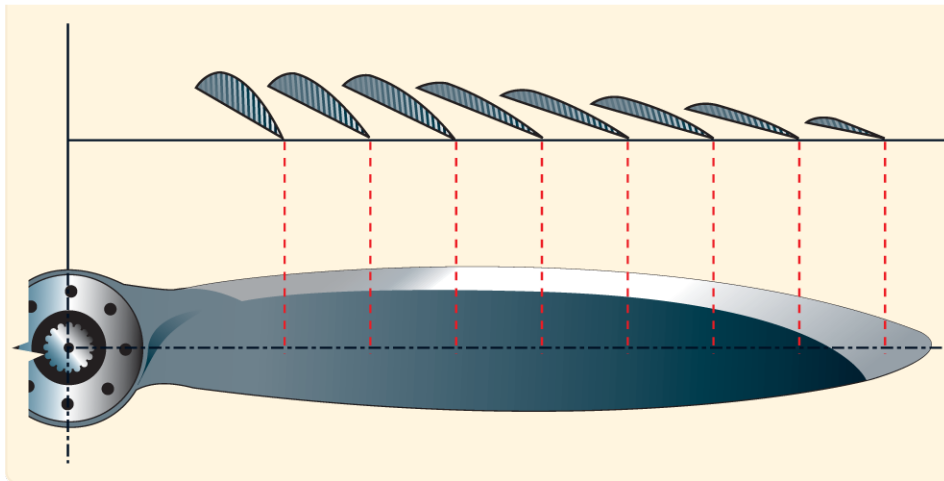


Figure 2.1: Propeller profile in BET

BET consider each section as a 2D airfoil that produce aerodynamic force and at each blade section is applied a force balance (Figure 2.2). Contemporary an axial and angular

momentum balance is applied.

These balances form a set of non-linear equations which are solved by iteration. For each blade section through a series of iteration is obtained a thrust and torque value.

Summing the result from each blade section is possible to estimate the global performance of the propeller.

The theory works only under the two following hypothesis:

1. There is no aerodynamic interaction between the analysis of each blade element.
2. The forces which are applied on the blade elements by the flow stream are determined only by the lift and drag characteristics of the blade element airfoil and by the orientation of the incoming flow.

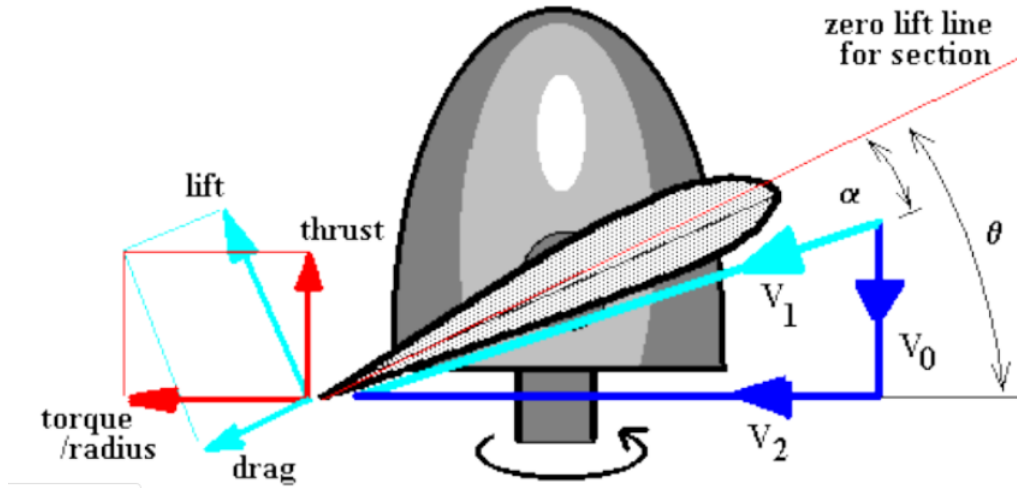


Figure 2.2: Propeller section in BET

In a design phase the BET is useful to size the rotor, in fact through it is possible to compare different blade and make a comparison between their performance on a large range of operating speeds.

For the blade is fixed a pitch angle ( $\theta$ ) and for each section there is a local flow velocity vector ( $V_1$ ). This speed comes from the summation of axial flow at the propeller disk ( $V_0$ ) and of the angular flow velocity vector ( $V_2$ ).

Lift and drag are obtained through 2-D aerofoil standard equations and they are projected on the normal and parallel axes of the propeller disk.

So is found the contribution of a single section on total thrust and total torque.

The difference between pitch angle and attack angle is:

$$\phi = \theta - \alpha \quad (2.1)$$

Section's thrust and torque are:

$$\Delta T = \Delta L \cos(\phi) - \Delta D \sin(\phi) \quad (2.2)$$

$$\frac{\Delta Q}{r} = \Delta D \cos(\phi) + \Delta L \sin(\phi) \quad (2.3)$$

Section's lift and drag can be written as ( $C_L$  and  $C_D$  for the given  $\alpha$ ):

$$\Delta L = C_L \frac{1}{2} \rho V_1^2 c dr \quad (2.4)$$

$$\Delta D = C_D \frac{1}{2} \rho V_1^2 c dr \quad (2.5)$$

So  $\Delta T$  and  $\Delta Q$ :

$$\Delta T = \frac{1}{2} \rho V_1^2 c (C_L \cos(\phi) - C_D \sin(\phi)) dr \quad (2.6)$$

$$\Delta q = \frac{1}{2} \rho V_1^2 c (C_D \cos(\phi) + C_L \sin(\phi)) dr \quad (2.7)$$

### 2.1.1 Inflow Factors

To make a realistic analysis the induced flow components are also considered in the BET. The axial flow at the propeller disk is equal to the multicopter's forward velocity ( $V_\infty$ ) but the propeller's induced axial flow increases its value.

The angular flow velocity vector is roughly equal to the blade section's angular speed ( $\Omega r$ ) but the propeller's induced flow is swirling and this reduces its value.

To take into account of the induced flow on  $V_0$  and  $V_2$  are defined the factors  $a$  and  $b$  which increases or decreases the major flow component where  $a$  is the axial inflow factor and  $b$  is the angular inflow factor (swirl factor).

So for the velocities  $V_0$  and  $V_2$  as said previously:

$$V_0 = V_\infty + V_\infty a \quad (2.8)$$

$$V_2 = \Omega r - b \Omega r \quad (2.9)$$

The local flow velocity and the angle of attack for the blade section are:

$$V_1 = \sqrt{V_0^2 + V_2^2} \quad (2.10)$$

$$\alpha = \theta - \tan^{-1} \frac{V_0}{V_2} \quad (2.11)$$

### 2.1.2 Axial and Angular Flow Conservation of Momentum

The conservation of flow momentum equations are applied both to axial and circumferential directions.

The change in flow momentum, on the axial direction, along the stream tube which starts upstream, pass through the propeller section and finally goes into the slipstream, has to be equal to the thrust produced by this blade's element.

$$\begin{aligned}\Delta T &= \text{Change in Momentum flow rate through tube at disk} \\ &= \text{Mass flow rate in tube} \times \text{Change in velocity along tube}\end{aligned}$$

$$\Delta T = \rho 2\pi r dr V_0 (V_s - V_\infty) \quad (2.12)$$

### 2.1.3 Iterative Procedure for Blade Element Theory

Applying the Bernoulli's equation on momentum conservation along the streamline to the three separate component of the tube, is obtained that axial velocity at the propeller disk is the average between freestream and slipstream velocities.

$$V_0 = \frac{V_\infty + V_s}{2} \quad (2.13)$$

Which becomes, using equation 2.8:

$$V_0 = V_\infty (1 + 2a) \quad (2.14)$$

Hence thrust change is:

$$\Delta T = 2\pi r \rho V_\infty (1 + a) (V_\infty (1 + 2a) - V_\infty) dr = 4\pi r \rho V_\infty^2 (1 + a) a dr \quad (2.15)$$

And angular momentum change is:

$$\begin{aligned}\Delta Q &= \text{Change in angular momentum rate of flow in tube} \times \text{radius} \\ &= \text{Mass flow rate in tube} \times \text{change in circumferential velocity} \times \text{radius}\end{aligned}$$

$$\Delta Q = \rho 2\pi r dr V_0 (V_{\theta(\text{slipstream})} - V_{\theta(\text{freestream})}) r \quad (2.16)$$

Analyzing the conservation of the angular momentum and the axial velocity change results that velocity in the splitstream it is double than the value at the propeller disk.

$$V_{\theta(\text{slipstream})} = 2b\Omega r \quad (2.17)$$

$$V_{\theta(\text{freestream})} = 0 \quad (2.18)$$

Therefore torque change becomes:

$$\Delta Q = 2\pi r \rho V_{\text{inf}}(1+a)(2b\Omega r)r = 4\pi r^3 V_{\infty}(1+a)b\Omega dr \quad (2.19)$$

Equations 2.19- 2.7- 2.15- 2.6- 2.11- 2.10 creates a system of non-linear equations containing the unknown terms  $\Delta T, \Delta Q, a, b$ . Iterating that system a solution for the unknown value is provided.

## 2.2 Propeller Design

Thanks to BET it is possible to determine thrust, power, torque and consequently the maximum speed needed to lift the drone paired with the cable.

The acceleration of this system is fixed by the Thrust Ratio at Max Takeoff Weight (TRMTOW).

In the first design phase let's consider a Maximum Take-Off Weight of 25 kg, as said in Chapter 1, and 5 kg of cable which is a cautelative value is possible to define through the Thrust Ratio at Max Takeoff Weight the thrust that every propeller has to exert.

In order to guarantee a good dynamic is chosen a TRMTOW equal to 2.5, this means that the UAV must supply a total force, at the maximum altitude, of:

$$T_{\text{tot}} = M_{\text{tot}} * TRMTOW * 9.81$$

$$T_{\text{tot}} = (25 + 5)2.5 * 9.81 = 735N$$

Some important parameters are chosen before performing a propeller design[9]. They include:

- Number of blades;
- Airfoil shape;
- Pitch and chord distribution;

After that the BET procedure follow the path:

- calculate local blade element setting angle ( $\theta$ )
- guess initial values of inflow and swirl factor  $a$  and  $b$
- Calculate axial and disk plane velocity ( $V_0$  and  $V_2$ )
- Calculate flow angle ( $\phi$ )
- Define the attack angle ( $\alpha = \theta - \phi$ )
- Determine the value of lift coefficient ( $C_L$ ) and drag coefficient ( $C_D$ ) from airfoil experimental data

- Calculate the local speed, the axial and thrust forces
- Re-calculate  $a$  and  $b$
- Check the convergence of new induction factors with the previous
- The process is repeated till the value of  $a$  and  $b$  have converged to within a specified tolerance

Using a MATLAB program which implements BET procedure, several configuration of multicopters with different kind of propeller are analyzed.

In a first time were considered the hexacopter configuration and the octacopter configuration in order to guarantee an higher reliability to the UAV also in case of breakage of a component and also because an higher number of rotor allow to minimize the power required for the performance. Results of this configuration with T-Motor MF3218 propeller are the following:

	Hexacopter	Octacopter	
<i>Mass</i>	30	30	kg
<i>TRMTOW</i>	2.5	2.5	-
<i>Total Power</i>	8740	7548	W
<i>Max speed</i>	3710	3210	rpm
<i>Hover Speed</i>	2144	1855	rpm
<i>Max Torque for each motor</i>	5.4	4.2	Nm

Table 2.1: System specifications with T-Motor MF3218 propeller

In a second time the choice is tacked on a quadcopter, because an easier control technique, an lower number of drives and motor leads to an higher reliability of the whole system.

As reference propeller on the quadcopter were taken the T-Motor P28x8.4", the T-Motor MF3218 and the T-Motor FA36.2x11.8" Push Type.

### First Analysis

In order to simplify the simulation, the chord and the pitch of the propeller are assumed constant. Radius and forward velocity are assumed very low.

Another simplification of the first analysis comes from the lift and drag coefficient used:

$$C_l = 6.2\alpha$$

$$C_d = 0.08 - 0.003C_l + 0.01C_l^2$$

From the analysis comes out that the torque, the maximum speed and consequently the power vary for every propeller. This is because each propeller through its diameter, pitch

and chord produces a different torque and different thrust.

Analyzing the T-Motor MF3218 propeller the system has the following results:

	<b>Quadcopter</b>	
<i>Mass</i>	30	kg
<i>TRMTOW</i>	2.5	-
<i>Total Power</i>	10648	W
<i>Max speed</i>	4535	rpm
<i>Hover Speed</i>	2619	rpm
<i>Max Torque for each motor</i>	5.6	Nm

Table 2.2: System specs with T-Motor MF3218

Analyzing the T-Motor P28x8,4” propeller the system has the following results:

	<b>Quadcopter</b>	
<i>Mass</i>	30	kg
<i>TRMTOW</i>	2.5	-
<i>Total Power</i>	13253	W
<i>Max speed</i>	6036	rpm
<i>Hover Speed</i>	3485	rpm
<i>Max Torque for each motor</i>	5.2	Nm

Table 2.3: System specs with T-Motor P28x8,4”

Since the results, decreasing the radius of the blade, get worst the last propeller analysed has to have a bigger radius than the previously configurations.

Analyzing the T-Motor FA36,2x11,8” propeller the system has the following results:

	<b>Quadcopter</b>	
<i>Mass</i>	30	kg
<i>TRMTOW</i>	2.5	-
<i>Total Power</i>	9875	W
<i>Max speed</i>	3514	rpm
<i>Hover Speed</i>	2029	rpm
<i>Max Torque for each motor</i>	6.7	Nm

Table 2.4: System specs with T-Motor FA36,2x11,8”

Is possible to see that the propeller T-Motor FA36,2x11,8” leads to the best results in terms of power required, maximum and hover speed. For this reason it is the propeller

chosen for the project.

The figures 2.3, 2.4 and 2.5 report respectively a comparison on torque, thrust and power in graphic form of the three different propeller analyzed.

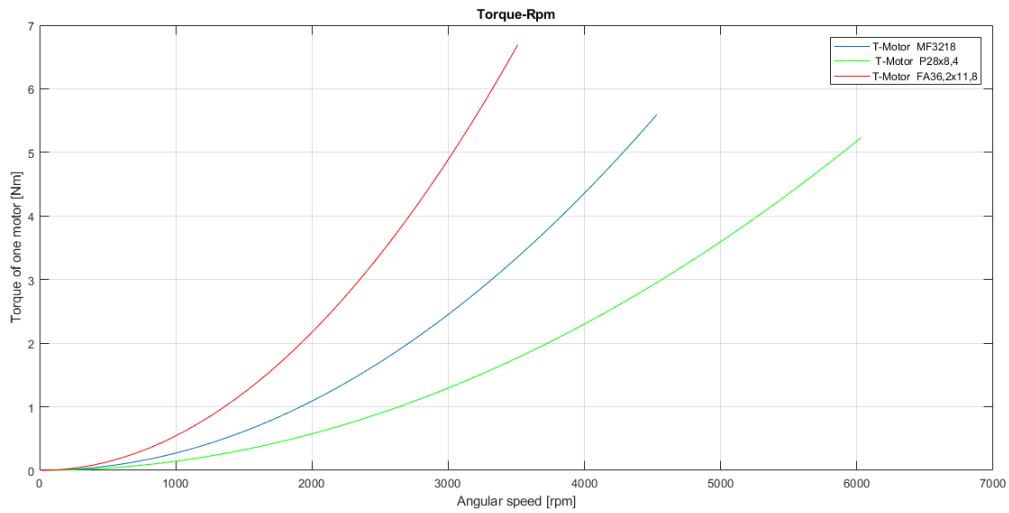


Figure 2.3: Torque comparison of a single motor with three different propellers

Figure 2.3 shows that the larger the propeller, the greater the torque it can provide and therefore also the one required to the motor.

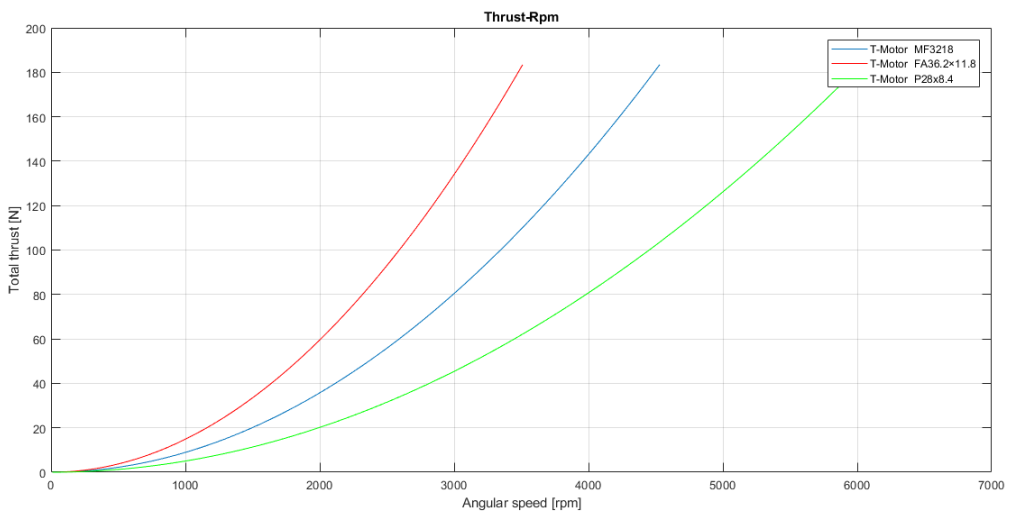


Figure 2.4: Comparison between thrust provided from a single motor of the UAV with different propellers

According to figure 2.4 the same thrust value is reached by different propellers at different speeds: the larger the blade, the lower the speed required to reach the de-weighted thrust.

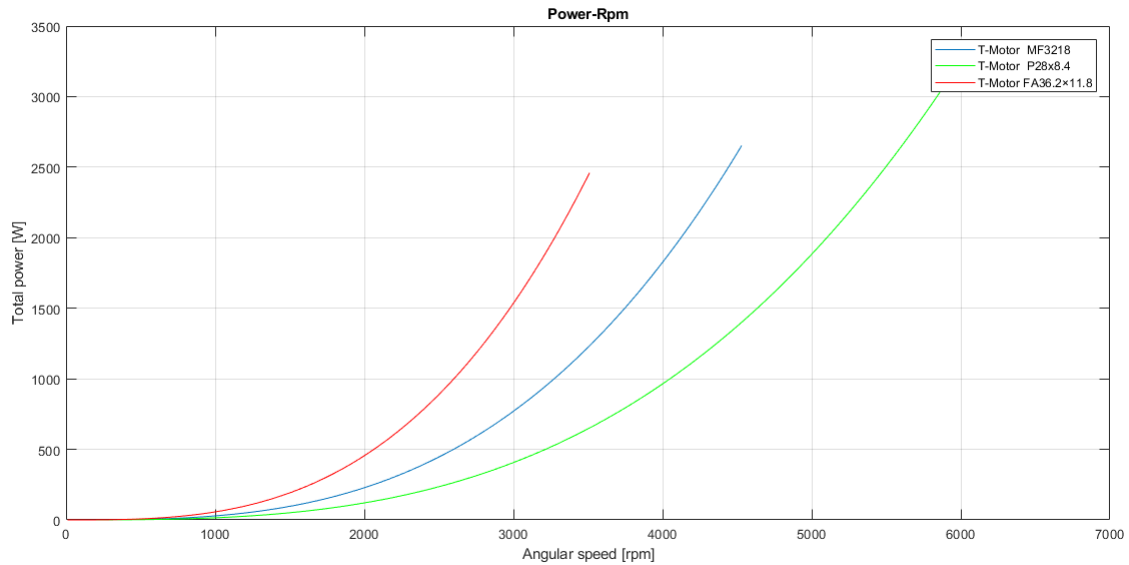


Figure 2.5: Power required by a single motor with different propeller

T-Motor FA36,2x11,8” provide advantages on several fronts. It provides bigger torque and the required thrust at lower speed with also a lower request of power.

### Second Analysis

In order to do a testing closer to the reality it was made a simulation with more specific blade’s parameters.

Three different type of airfoils were analyzed (figure 2.8):

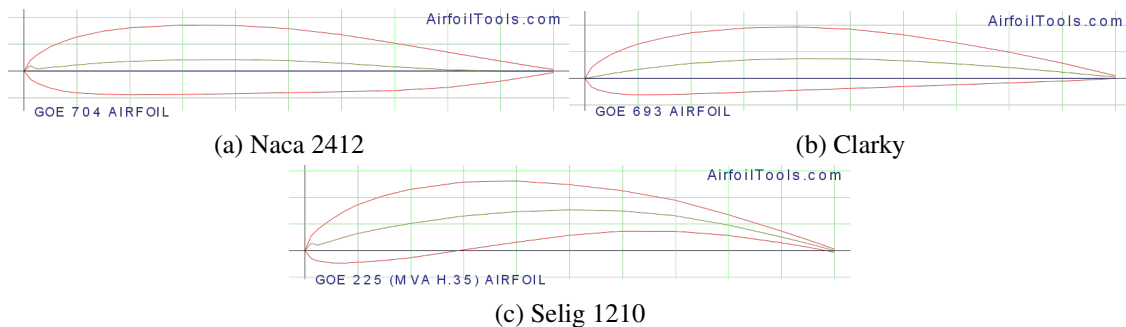


Figure 2.6: Propeller’s airfoils analyzed

- Naca 2412
- Clarky
- Selig 1210

The analysis is conducted with the same procedure as in the previous case, but with different airfoils are determined different lift and drag coefficient respect to the previous analysis. The lift and drag coefficient have been derived numerically with XFOil through computational fluid dynamics (CFD) analysis on the considered profiles. The best results are obtained with the Selig 1210 airfoil.

To conclude the analysis the last step for propeller design is to simulate the system with the following changes:

- Thrust Ratio at Max Takeoff Weight changes from 2.5 to 2
- The total system weight considering also the cable at the maximum length is 25kg
- The propeller's chord is no more constant but it varies along the radius following the profile of T-Motor FA36,2x11,8”(figure 2.7).

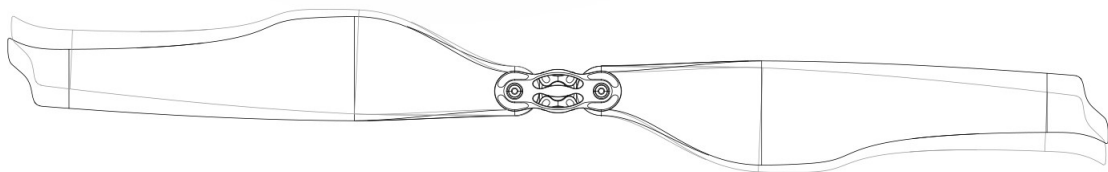


Figure 2.7: T-Motor FA36,2x11,8” profile

With this configuration are obtained the results that were searched and are defined the mechanical power, the torque and the speed required from the propeller to lift off and to hover.

The final value of power, maximum speed, hover speed and torque are:

<b>Quadcopter</b>				
	<b>Selig 1210</b>	<b>Naca 2412</b>	<b>Clarky</b>	
<i>Mass</i>	25	25	25	kg
<i>TRMTOW</i>	2	2	2	-
<i>Total Power</i>	4929	8416	5413	W
<i>Max speed</i>	1895	3772	2443	rpm
<i>Hover Speed</i>	1340	2667	1728	rpm
<i>Max Torque for each motor</i>	6.2	5.3	5.28	Nm

Table 2.5: System specs with T-Motor FA36,2x11,8”, selig airfoils and variable chord

The best configuration is with T-Motor FA36,2x11,8” propeller with Selig 1210 airfoils.

Lift, drag coefficient and the angle of attack along the blade of Selig 1210 airfoils are reported in figure 2.8.

### 2.2.1 Variable Pitch

For the majority of flight cases the differential RPM control is enough for an agile flight but in other cases not [10].

The main boundary is the control bandwidth which is limited from the rotational inertia. The control bandwidth becomes smaller and smaller proportionally with the increasing of the size of the quadcopter. As a matter of fact larger vehicle require larger propeller which has big inertia and consequently a slower response to the driver command.

This fact may lead to the instability of the quadrotor.

When the quadrotor size is too large the RPM is no longer sufficient to guarantee stability to the vehicle because is required to the motor a dynamic that exceeds its capacity.

The variable pitch allows better performance in fact with it the rate of change of the thrust is increased, the deceleration potential could become greater than gravity and it allows the inverted flight.

So the combined use of variable pitch and RPM voltage control increase the control range of the quadcopter leading to a more agile flight.

For large quadrotor some maneuvers are very difficult but thanks to variable pitch they might be obtainable.

Variable pitch allows an improvement of the acceleration and deceleration, performing more aggressive flight.

In our case in figure 2.9 is shown how the variable pitch helps in increasing the performance of the vehicle. In particular figure 2.9 shows as in previous cases the thrust has a quadratic relationship with the angular velocity (figure 2.4) while presenting a linear relationship with the pitch.

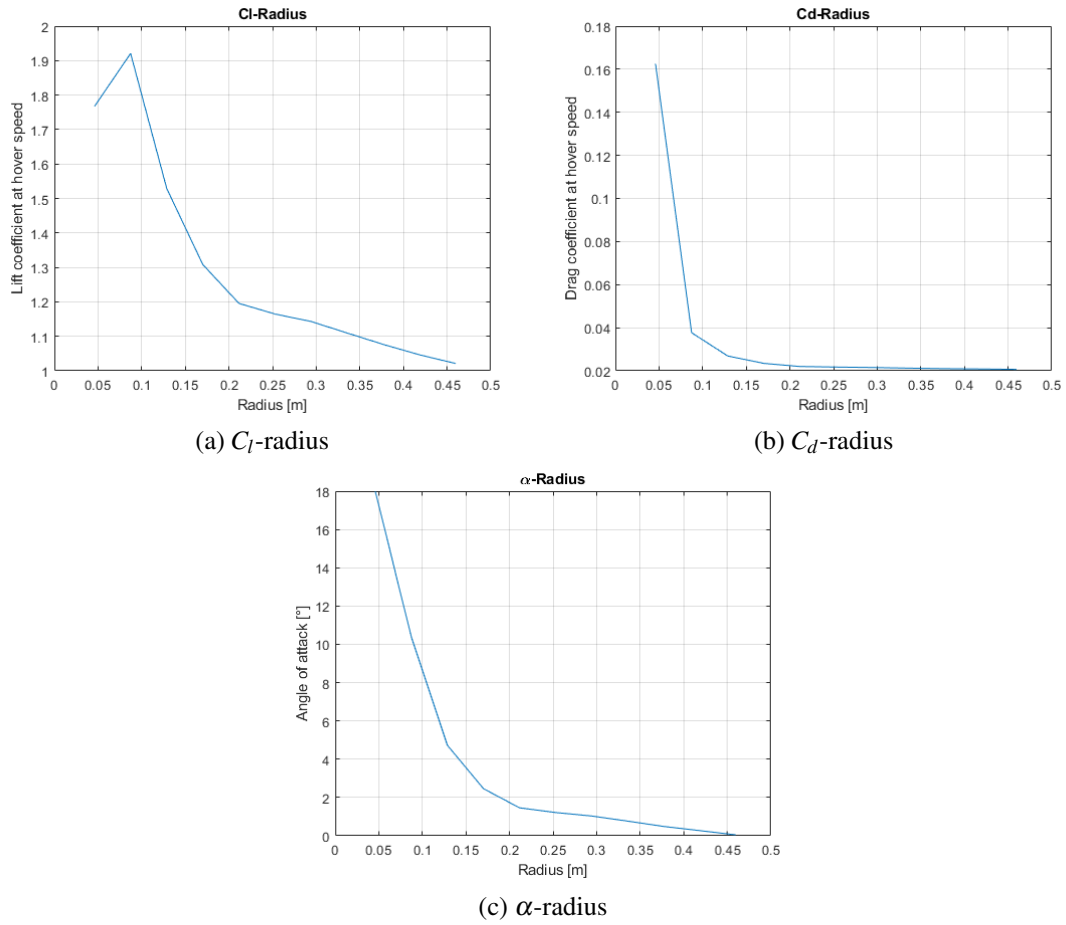


Figure 2.8: Lift and drag coefficient

To show better the influence of the variable pitch on the quadrotor performance it is analyzed the hover speed and the maximum speed as the pitch varies.

In figure 2.10 is possible to see that the hover speed (blue line) decreases increasing the pitch, and the maximum speed does the same. This is a direct consequence of the thrust increase shown in figure 2.9.

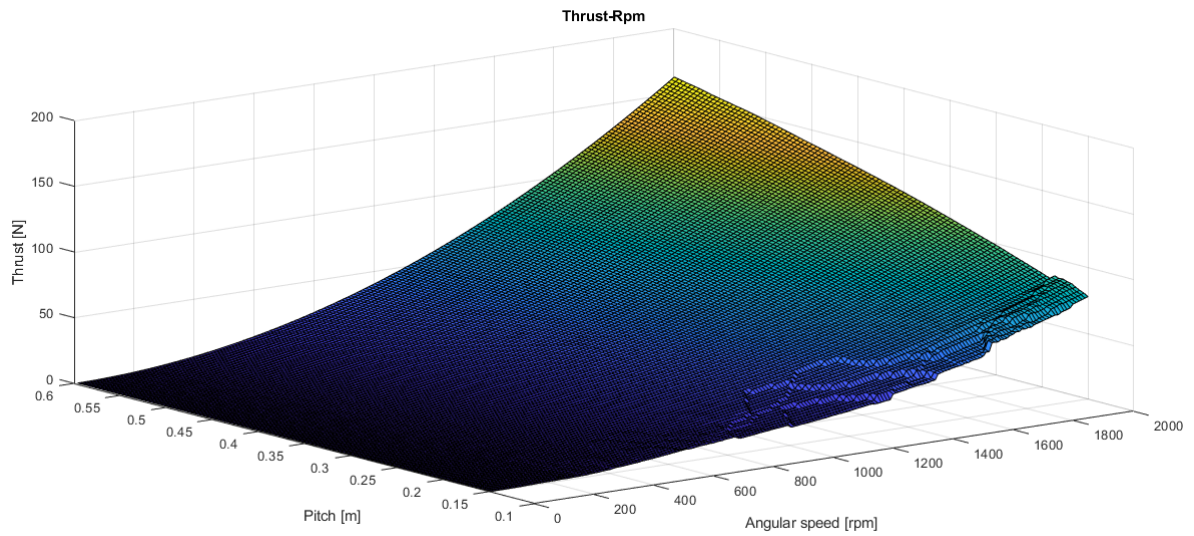


Figure 2.9: Thrust generated by the propeller in relation with its pitch and its angular speed

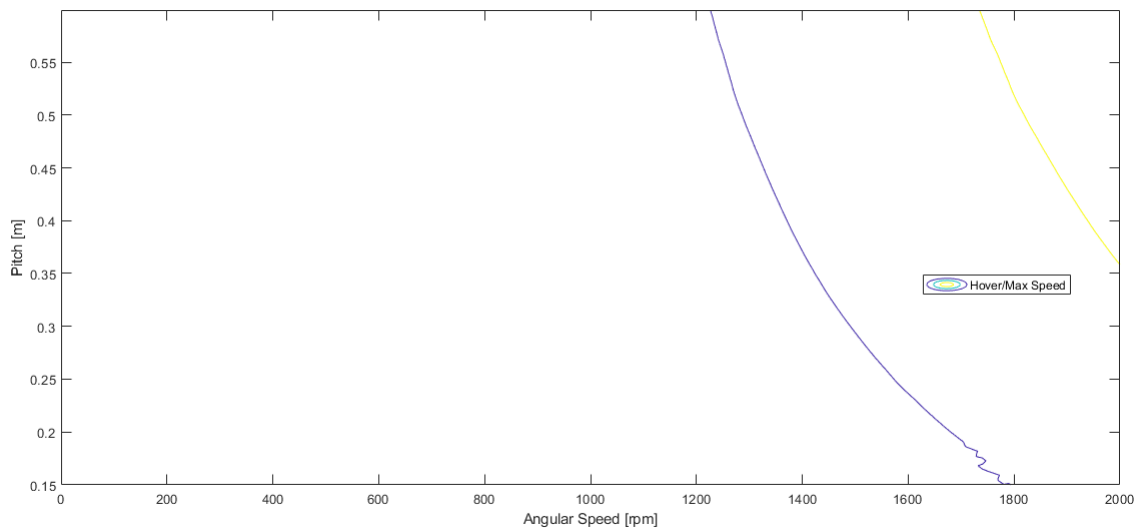


Figure 2.10: Iso-thrust curve at hover and maximum speed changing as the pitch varies

## Chapter 3

# Motor Type and Modelling

This chapter is about the choice of the motor in order to find out what kind of motor fits better the requirement of the project. A comparison between several kind of motors is done and is chosen the better one. Then will be illustrated its construction features, mathematical model and the control method used to drive it.

### 3.1 Motor Type

To decide motor is more suitable for this application we have to compare several kinds of motor available.

Significant criteria in the choice will be the power density, torque per ampere rating and the constant torque speed range (CTSR). Other criteria for comparing different motor but less important in the choice are cogging and ripple torque, parameter sensitivity, feedback devices and inverter rating [11].

The first step is to decide if the motor has to be a dc brush or a brushless servo.

The choice of a brushless servo motor drives over the brush type dc motor drives is related to higher robustness, torque, speed bandwidths, easier heat dissipation and lower maintenance.

Furthermore, the mechanical commutator enforce strong limitations on its reliability, on maximum speed and overcurrent tolerance.

Next step is the choice between ac motor and switched reluctance motor. Since the switched reluctance has pulsating torque for applications that require an almost flat torque output, like a UAV motor, ac motor is more suitable.

Next is necessary to choose between induction motor or PM motor. The PM motor has some advantages and some disadvantages compared with induction motors.

Advantages of the PM motors	Advantages of induction motors
Lower inertia and fasted dynamic thanks to a lighter rotor	Large flux weakening range and simple control of that range
Higher efficiency	Lower cogging torque
Inherent excitation from the permanent magnet	Cheaper feedback device
Smaller size	Lower cost
Negligible rotor losses	Higher rotor working temperature

Since for the UAV application fast dynamic, smaller size and weight are crucial variable the choice falls on PM motors.

There are two kind of permanent magnet motor, which are PMSM drive and BLDC motor. These two types of motor are sons of the same design philosophy which consists in replace the wound rotor with a permanent magnet in order to obtain excitations. But in practice these motors are realized in different way.

PMSM has a sinusoidal back electro-motive force instead BLDC has trapezoidal back electro-motive force. Shape of the magnet are different, BLDC has a magnet which produces a square induction wave whereas PMSM has a rounded trapezoid induction waveform (figure 3.1).

Also stator windings are different, in fact BLDC has concentrated windings and PMSM

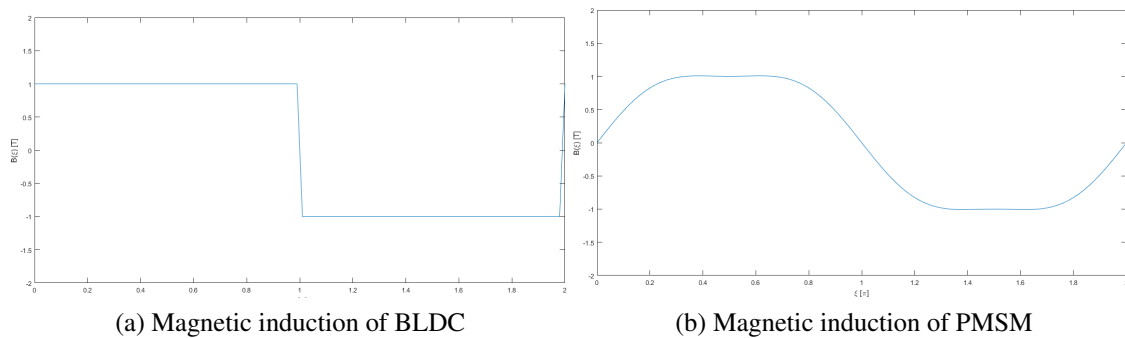


Figure 3.1: Comparison between BLDC and PMSM magnetic induction waveform

has sinusoidally distributed winding (figure 3.2).

Finally, BLDC needs rectangular-shaped current to obtain a steady torque on the contrary PMSM needs sinusoidal currents to produce steady torque.

To compare this machine are analysed the following criteria: power density, torque per inertia ratio, torque per unit current, cogging and ripple torque, choice of feedback device ([11]).

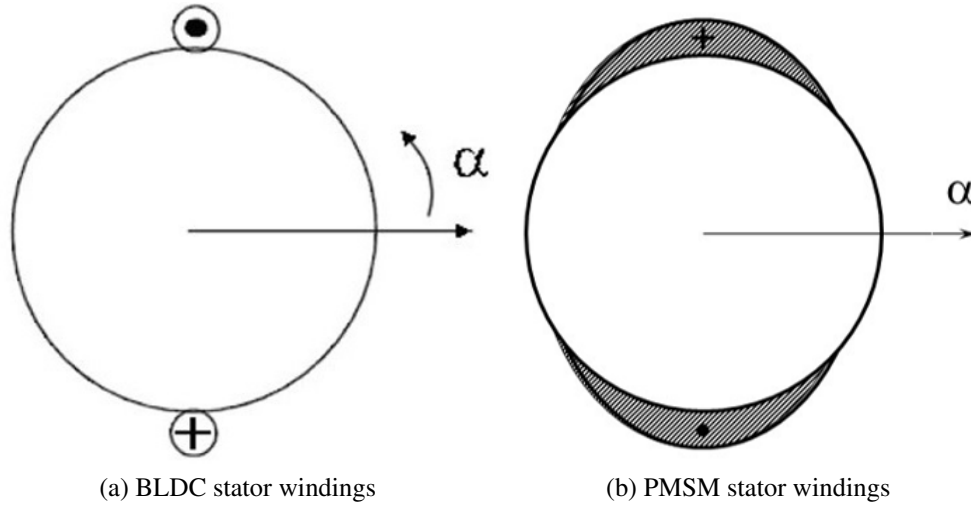


Figure 3.2: Comparison between BLDC and PMSM stator windings

### Power Density

Power density especially in aerospace actuators is fundamental in order to minimize the weight for a required power output.

Power density is limited by capability of the motor to dissipate the heat, so the power output of PMSM and BLDC motor are compared on the base of same copper losses. Are considered only copper losses because on the rotor losses are neglectable and in a first analysis we consider equal the eddy current losses and hysteresis losses of the two motors type.

Copper losses are related to the fundamental rms value of the current so assuming that the two machines have the same copper losses we can write:

$$3(I_{p1}/2)^2 R_a = 3(\sqrt{2}I_{p2}/\sqrt{3})^2 R_a \quad (3.1)$$

$$(I_{p1}/2)^2 = (\sqrt{2}I_{p2}/\sqrt{3})^2 \quad (3.2)$$

$$I_{p1} = 2I_{p2}/\sqrt{3} = 1.15I_{p2} \quad (3.3)$$

where  $I_{p1}$  is the sinusoidal current peak and  $I_{p2}$  is the trapezoidal current peak So the output power is:

$$\sqrt{2}\sqrt{2}E_p I_{p2} / (\sqrt{3}\sqrt{3}E_p I_{p1} / \sqrt{2}\sqrt{2}) = 1.15 \quad (3.4)$$

BLDC is able to provide 15% more power than PMSM.

### Torque per Inertia Ratio

Torque per inertia ratio with the same rotor inertia in BLDC is 15% bigger than PMSM.

### **Torque per Unit Current**

Torque per unit current is an important parameter because producing the same output torque with a smaller current means sizing the converter for a lower current and reducing copper, inverter, rectifier losses.

Comparing PMSM and BLDC motor with the same back electro motive force the torque current per unit of the BLDC is 33% higher than the PMSM one.

This result comes from the difference between the value of current and BEMF at the fundamental component, in fact both current and BEMF of BLDC are higher than 15% of the PMSM.

### **Torque Ripple**

Torque ripple is much more significant in the BLDC, because in the real case the current has a trapezoidal shape instead of the rectangular shape of ideal case. So, at each commutation the BLDC motor torque is subjected to a ripple which is absent in the PMSM.

### **Choice of Feedback Device**

Choice of Feedback Device is related to the control method. In BLDC motor the currents each phase conduct for  $120^\circ$  and it is at 0 for  $60^\circ$  so to control the motor it is necessary only to identify the angular sextant in which the rotor is.

In PMSM instead sinusoidal currents are needed so a continuous feedback rotor position is needed. So PMSM need high resolution position transducer and BLDC needs low resolution position transducer.

## **3.2 Brushless DC Motor**

The Brushless DC motor has replaced the traditional brushed DC motor to avoid the use of the mechanical commutator substituting it with an electrical switch circuit [12].

To realize the commutation without brush was placed a stator winding on the stator and magnet steel on the rotor. While for the speed control must be included a rotor position sensor, a control circuit and a power inverter.

### **3.2.1 Stator Cores**

Three phase symmetric windings are wounded on the iron core with a Y connection. The most common winding is concentrated at full pitch, in which the wires of the same phase

are wound on one cog. The Back-EMF generated by concentrated full-pitch winding is trapezoidal.

### 3.2.2 PM Rotor

The BLDC rotor is consisting in permanent magnet putted on the surface or inside an iron nucleus. Nowadays the more common material for permanent magnet are the rare earth like NdFeB which has a high coercive field and high remanence field. The magnets are used to produce the magnetic field at the air gap.

It will be analyzed the surface mounted PM rotor, where tile-shaped permanent magnet is mounted on the surface of the iron core. The result of this building strategy is to obtain a square flux density at the airgap.

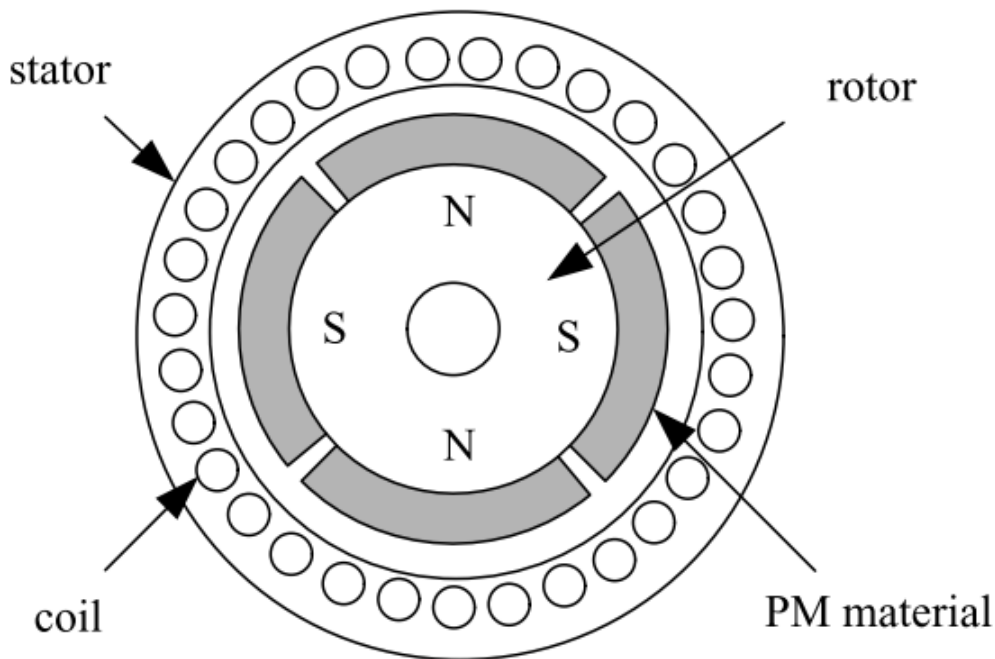


Figure 3.3: Cross sectional image of a BLDC

### 3.2.3 Position Sensors

In order to control correctly the inverter a position sensor is needed which detects the rotor position and communicate it to the logic switch circuit. So, the right current commutation is obtained according to the rotor position and the PM rotor can rotate because of the magnetic field generated by the stator current at the air-gap.

The sensor that will be used it is the Hall sensor because of its compact volume and low price.

### 3.2.4 Drive Mode

The motor is driven from a full bridge inverter where 6 power switches are used to turn on and off the currents of the windings following the logical command that comes from electronic speed controller's processor which are related to the signal produced by the Hall position sensors.

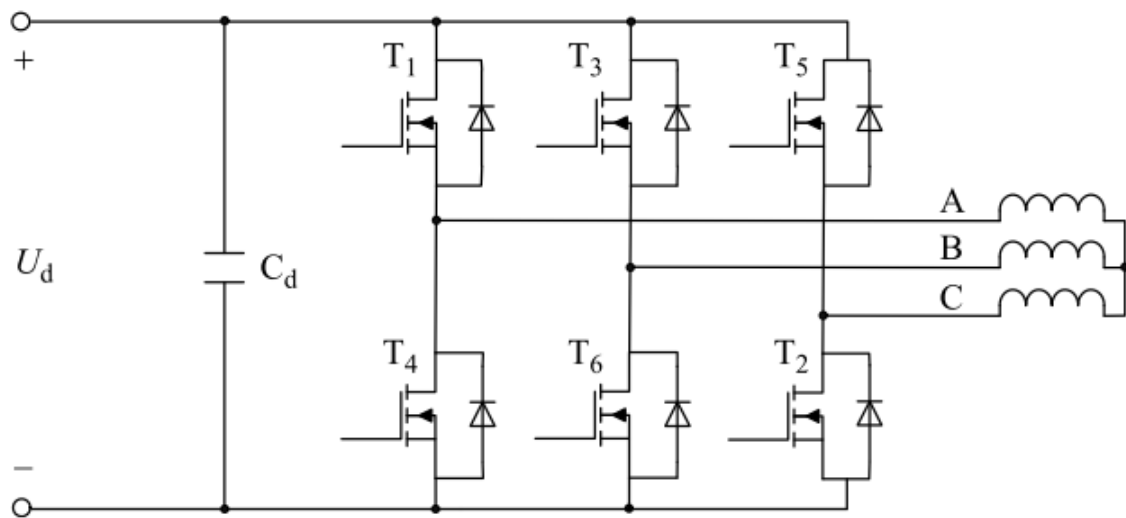


Figure 3.4: Full-bridge driving circuit

**Two-phase Conduction Mode** The drive philosophy is to conduct two phases at each time turning off the third one. The choice of the conducting or non-conducting phase are related to the rotor position. The bridge does a commutation every  $60^\circ$  electrical angle and each phase conducts continuously for  $120^\circ$  electrical angle after and before its commutation.

**Three-phase Conduction Mode** In this conduction mode there are always three conducting switches. With this mode is possible to reduce the torque ripple but it could increase the probability that the upper and the lower switch of the same leg are conducting at the same time.

The sinusoidal control is an example of this conduction mode.

### 3.2.5 Mathematical Model

The mathematical model is built for a three-phase BLDC motor, with a Y stator winding connection and concentrated full-pitch. The rotor is isotropic.

Hall sensors are placed symmetrically every  $120^\circ$ .

The mathematical model is built under the following hypothesis:

1. Core saturation and iron losses are neglected.
2. Armature reaction is neglected and the magnetic induction at the air gap is trapezoidal with a flat zone of  $120^\circ$  electrical angle.
3. Cogging effect are ignored.
4. Power switches and flywheel diodes are ideal.

Under positive direction reference shown in the picture 3.5c is possible to express each phase voltage as:

$$u_x = R_x i_x + e_x \quad (3.5)$$

where :

$x$  – Denotes the general phase A, B or C;

$u_x$  – Phase voltage;

$R_x$  – Phase resistance, all the phases have the same resistance;

$i_x$  – Phase current;

$e_x$  – Phase induced electromotive force (EMF);

The induced EMF is equal to the change rate of the magnetic flux:

$$e_x = \frac{d\Psi_x}{dt} \quad (3.6)$$

The magnetic flux is equal to:

$$\Psi_x = L_x i_x + M_{xy} i_y + M_{xz} i_z + \Psi_{pm}(\theta) \quad (3.7)$$

where:

$\Psi_{pm}(\theta)$  is the PM flux linkage of the phase  $x$ ;

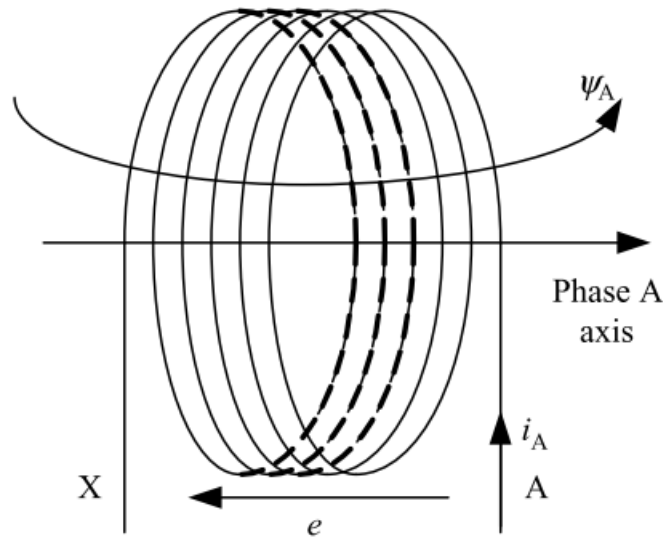
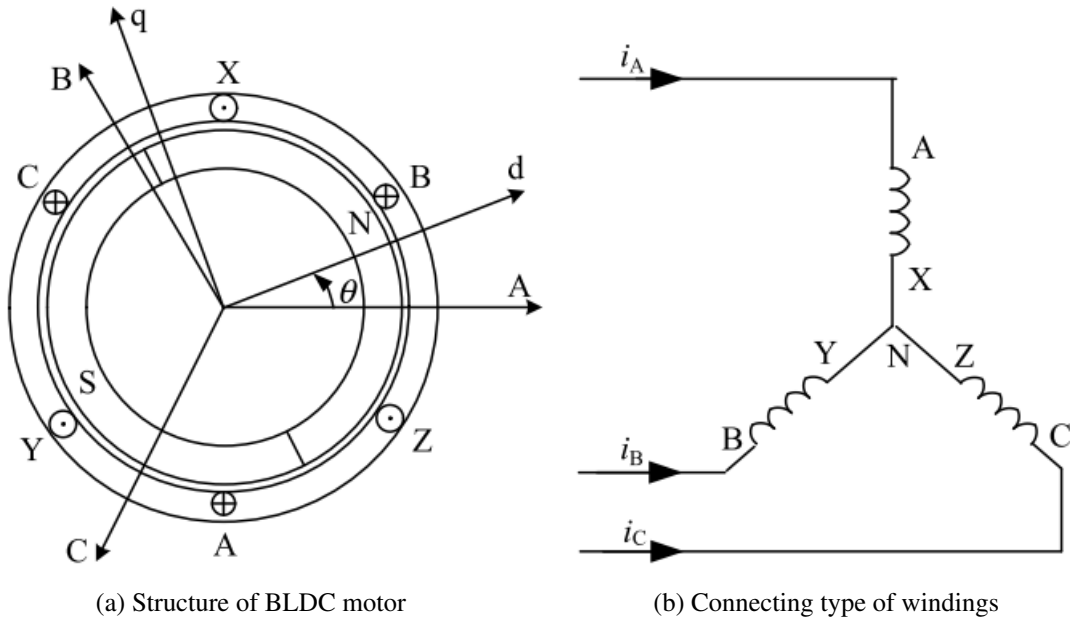
$\theta$  is the rotor angle position, is the angle between the d axis and the the x-phase axis;

$L_x$  is the self inductance of the phase  $x$ ;

$M_{xy}, M_{xz}$  are the mutual inductance of the phase  $x$  with the phase  $y$  and  $z$ ;

Since the motor is isotropic the inductance both self and mutual doesn't change with time and thanks to symmetry of the motor self inductance are equal and also all the mutual inductance.

$$L_A = L_B = L_C = L \quad (3.8)$$



$$M_{AB} = M_{BA} = M_{BC} = M_{CB} = M_{AC} = M_{CA} = M \quad (3.9)$$

So substituting them into voltage equation (3.5) for example for phase A we get

$$u_A = Ri_A + L \frac{di_a}{dt} + M \frac{di_B}{dt} + M \frac{di_c}{dt} + e_a \quad (3.10)$$

And due to the Y connection of the stator the current satisfy the condition

$$i_A + i_B + i_C = 0 \quad (3.11)$$

The equation is simplified as

$$u_a = Ri_A + (L-M)\frac{di_A}{dt} + e_A \quad (3.12)$$

Then the three phases expressed in matrix become

$$\begin{bmatrix} u_A \\ u_B \\ u_C \end{bmatrix} = \begin{bmatrix} R & 0 & 0 \\ 0 & R & 0 \\ 0 & 0 & R \end{bmatrix} \begin{bmatrix} i_A \\ i_B \\ i_C \end{bmatrix} + \begin{bmatrix} L-M & 0 & 0 \\ 0 & L-M & 0 \\ 0 & 0 & L-M \end{bmatrix} \frac{d}{dt} \begin{bmatrix} i_A \\ i_B \\ i_C \end{bmatrix} \begin{bmatrix} e_A \\ e_B \\ e_C \end{bmatrix}$$

where:

$L-M$  — synchronous inductance  $L_s$ ;

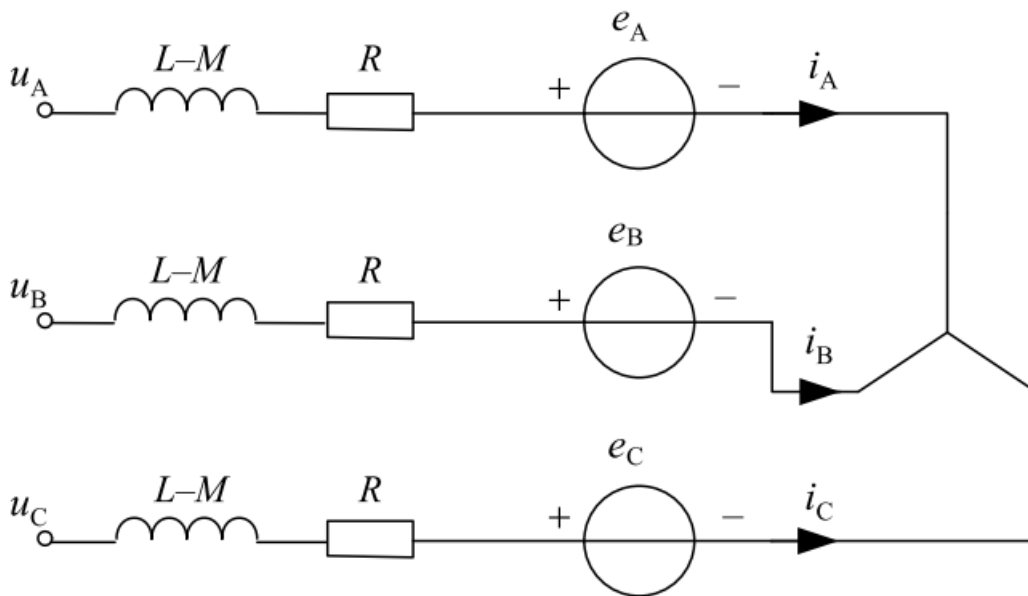


Figure 3.5: Equivalent circuit of the BLDC motor

Since in the practical system the neutral point of the Y connection is not accessible the phase voltages are difficult to detect.

So the mathematical model is based on the line-line voltage, and we obtain it from the subtraction of the phase voltage equations

$$\begin{bmatrix} u_{AB} \\ u_{BC} \\ u_{CA} \end{bmatrix} = \begin{bmatrix} -R & -R & 0 \\ 0 & R & -R \\ -R & 0 & R \end{bmatrix} \begin{bmatrix} i_A \\ i_B \\ i_C \end{bmatrix} + \begin{bmatrix} L_s & -L_s & 0 \\ 0 & L_s & -L_s \\ -L_s & 0 & L_s \end{bmatrix} \frac{d}{dt} \begin{bmatrix} i_A \\ i_B \\ i_C \end{bmatrix} \begin{bmatrix} e_A & e_B \\ e_B & e_C \\ e_C & e_A \end{bmatrix}$$

Power and torque are detected from power balance where power absorbed by the source is equal to copper loss, iron loss and power transferred to the rotor.

The power transferred is equal to

$$P_e = e_A i_A + e_B i_B + e_C i_C \quad (3.13)$$

And neglecting the strain loss and mechanical loss the electromagnetic power is totally turned into kinetic energy

$$P_e = T_e \omega \quad (3.14)$$

where  $T_e$  – electromagnetic torque;

$\omega$  – angular rotor velocity;

So

$$T_e = \frac{e_A i_A + e_B i_B + e_C i_C}{\omega} \quad (3.15)$$

Since EMF is

$$e_x = p\omega\Psi_{pm,x} \quad (3.16)$$

Torque can be written as

$$T_e = p[\Psi_{pm,A}I_A + \Psi_{pm,B}I_B + \Psi_{pm,C}I_C] \quad (3.17)$$

And since each Pm flux linkage at the flat top are opposite to each other winding and because of the Y connection the equation 3.17 can be simplified as

$$T_e = 2p\Psi_m i_A = K_T i_A \quad (3.18)$$

where  $\Psi_m$  – maximum PM flux linkage value of each winding;

$K_T$  – torque coefficient;

$i$  – steady phase current;

To complete the mathematical model of the electromechanical system is written also the motion equation

$$T_e - T_L = J \frac{d\omega}{dt} + B_v \omega \quad (3.19)$$

where  $T_L$  – load torque;

$J$  – rotor inertia moment;

$B_v$  – viscous friction coefficient;

### 3.2.6 Characteristic Analysis

Taking into consideration the BLDC controlled by full-bridge when phase A and B are conducted the line voltage equations are

$$u_{AB} = 2Ri + 2(L - M) \frac{di}{dt} + (e_A - e_B) \quad (3.20)$$

Whose equivalent circuit is

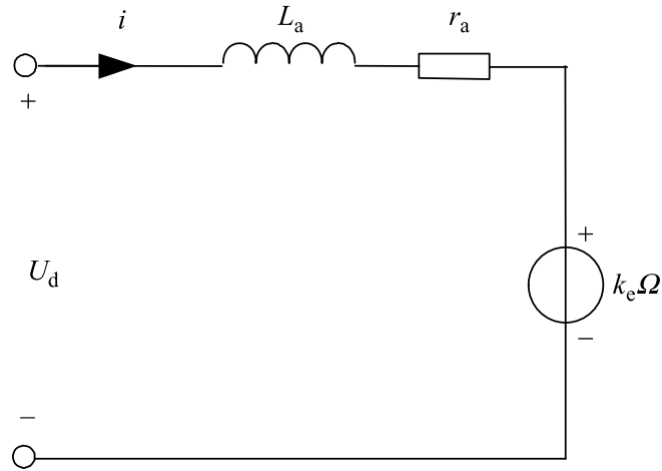


Figure 3.6: Equivalent circuit with two phase excited

So the equivalent circuit 3.6 can be expressed as

$$U_d = r_{eq}i + L_{eq}\frac{di}{dt} + k_e\omega \quad (3.21)$$

where

$U_d$  – DC bus voltage;

$r_{eq}$  – line resistance winding =  $2R$ ;

$L_a$  – line inductance =  $2(L - M)$ ;

$k_e$  – line BEMF constant =  $2p\Psi_m$   $\omega$  – motor velocity;

In steady state the equation 3.21 and 3.19 are simplified as

$$U_d = r_{eq}I + k_e\omega \quad (3.22)$$

$$k_T I - T_L = B_v\omega \quad (3.23)$$

Ignoring the viscous friction the round per second of the motor can be derived the mechanical characteristic of the motor which expresses the relation between speed and electromagnetic torque

$$\omega = \frac{U_d}{k_e} - \frac{R}{k_T k_e} T_e \quad (3.24)$$

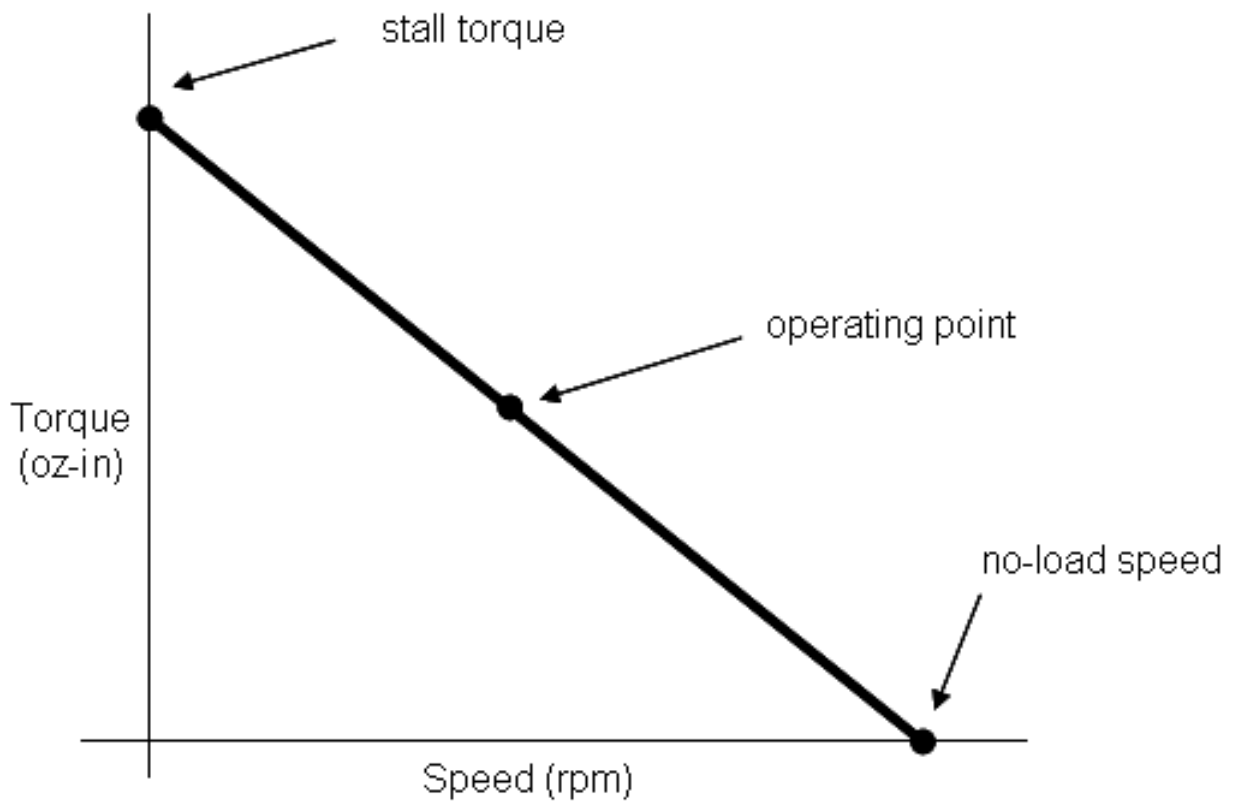


Figure 3.7: Mechanical characteristic

## Chapter 4

# Simulation for BLDC Motor Drives

In this chapter is provided the modelling of the BLDC motor in Simulink environment. The aim of this chapter is to analyze the performance of the electromechanical actuator in operating conditions, in terms of torque and speed.

A second purpose of this chapter is to find out the electrical features of the modelled system as the circulating currents, the phase voltage and the electric power.

The simulation phase is very important because, before a flight test simulation, tools provide a good method to verify the dynamic behaviour of the system.

In this way we can check the system in a fast and low-cost way, avoiding dangerous results.

The motor simulation is developed in MATLAB/Simulink R2017b.

### 4.1 Mechanical Model of the Electrical Motor

As said in the previous chapter the mechanical model is realized following the canonical Newton's equation of mechanics (3.17) and on the Simulink is modelled as:

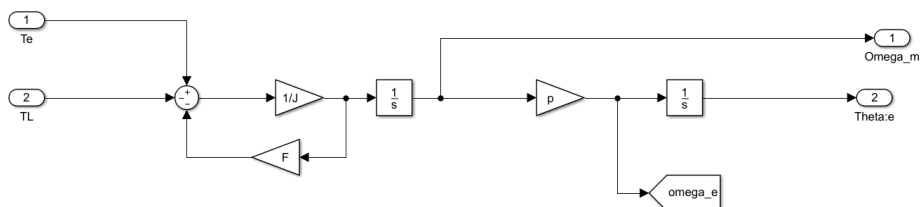


Figure 4.1: Motor mechanical model

The torque load is a function of the pitch and of the propeller velocity. The relation between speed, torque and velocity is reported in figure 4.2.

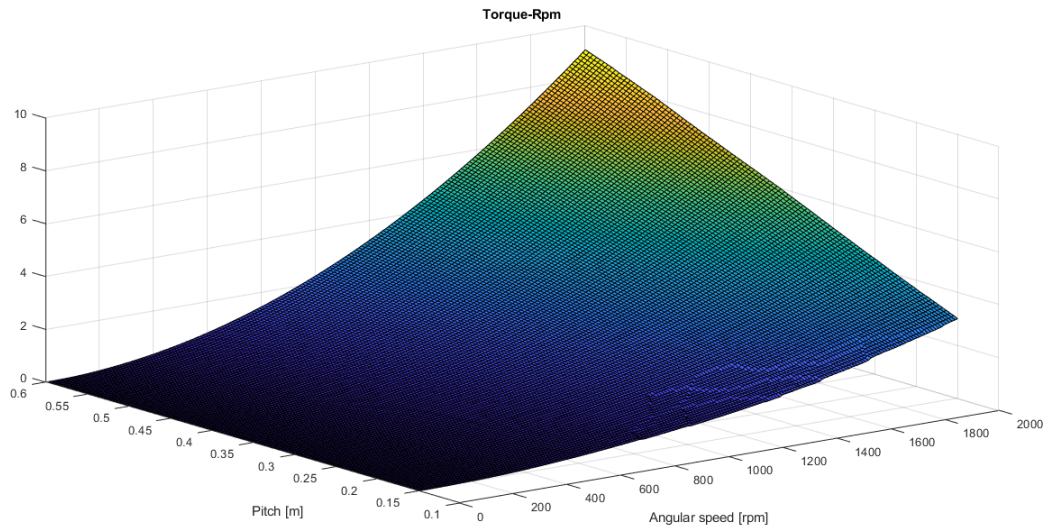


Figure 4.2: Torque load in relation with propeller pitch and velocity

As the thrust (figure 2.9) also the load torque is a function of both angular speed and pitch. Relation between torque and speed is quadratic as in figure 2.3 and is almost linear with pitch.

The friction torque, instead, is supposed at  $10^{-3}$  Nm.

## 4.2 Electromagnetic Model of the Motor

The electromagnetic model of the motor is divided into three main blocks: one which calculate the back electromotive force, one which calculate the currents and one for the computation of the electromagnetic torque.

### 4.2.1 BEMF Calculation

The aim of this block is to realize three trapezoidal waveforms with a flat range of  $120^\circ$  and shifted each other by  $\frac{2}{3}\pi$ .

The block receives as input the electrical speed in *rad/s* and the electric angle of the rotor position in radians.

The Back Electromotive Force (BEMF) of each phase depends on the rotor position and

on the motor angular speed with the following relation:

$$e_x = \omega_e \lambda_m f_x(\theta_e) \quad (4.1)$$

where:

$\lambda_m f_x(\theta_e)$  — Is the flux generated by the magnet linked with the phase x;

$\theta_e$  — Is the electric angle of the rotor;

The relation between BEMF and the rotor angle is expressed in the following table:

$\theta_e [^\circ]$	$f_a(\theta_e)$	$f_b(\theta_e)$	$f_c(\theta_e)$
0-60	1	1	$1 - \frac{6}{\pi} \theta_e$
60-120	1	$-3 + \frac{6}{\pi} \theta_e$	-1
120-180	$5 - \frac{6}{\pi} \theta_e$	1	-1
180-240	-1	1	$-7 + \frac{6}{\pi} \theta_e$
240-300	-1	$9 - \frac{6}{\pi} \theta_e$	1
300-360	$-11 + \frac{6}{\pi} \theta_e$	-1	1

Table 4.1: Function of the BEMF in relation to the rotor position

With the relation shown in table 4.1 we obtain a linked flux with a trapezoidal trend and a flat range of  $120^\circ$ .

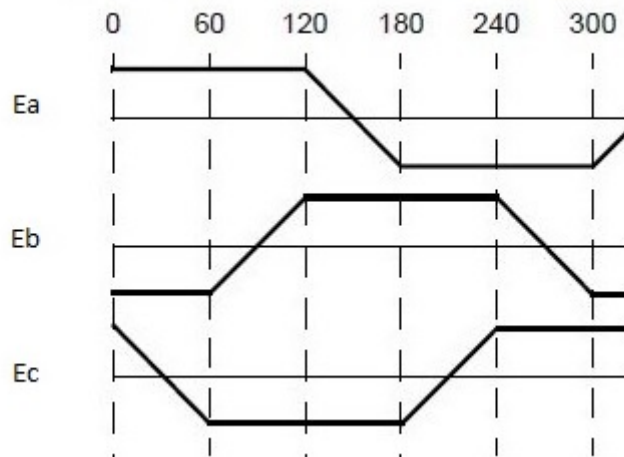


Figure 4.3: BEMF trends

## 4.2.2 Current Calculation

From the equation of the phase voltages:

$$\begin{bmatrix} u_A \\ u_B \\ u_C \end{bmatrix} = \begin{bmatrix} R & 0 & 0 \\ 0 & R & 0 \\ 0 & 0 & R \end{bmatrix} \begin{bmatrix} i_A \\ i_B \\ i_C \end{bmatrix} + \begin{bmatrix} L-M & 0 & 0 \\ 0 & L-M & 0 \\ 0 & 0 & L-M \end{bmatrix} \frac{d}{dt} \begin{bmatrix} i_A \\ i_B \\ i_C \end{bmatrix} \begin{bmatrix} e_A \\ e_B \\ e_C \end{bmatrix}$$

Currents are calculated in the Simulink environment from the electrical circuit realized by Simscape element:

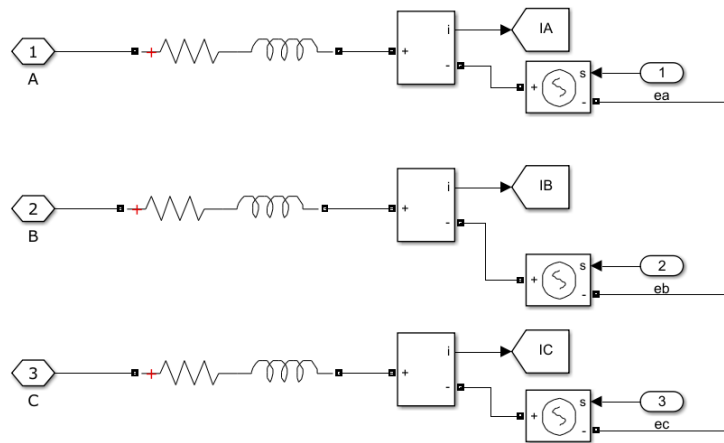


Figure 4.4: Electrical circuit of the motor

Where the BEMF of the three phases are the one calculated in the upper section and are considered as a voltage source.

Instead the currents are calculate through a current measurement after the RL branch.

As is shown in figure 4.4 the motor has a Y connection.

## 4.3 Hall Effect Sensor

The following block is the hall effect sensor which returns 3 bit and each triad correspond to a sextant as shown in figure 4.5.

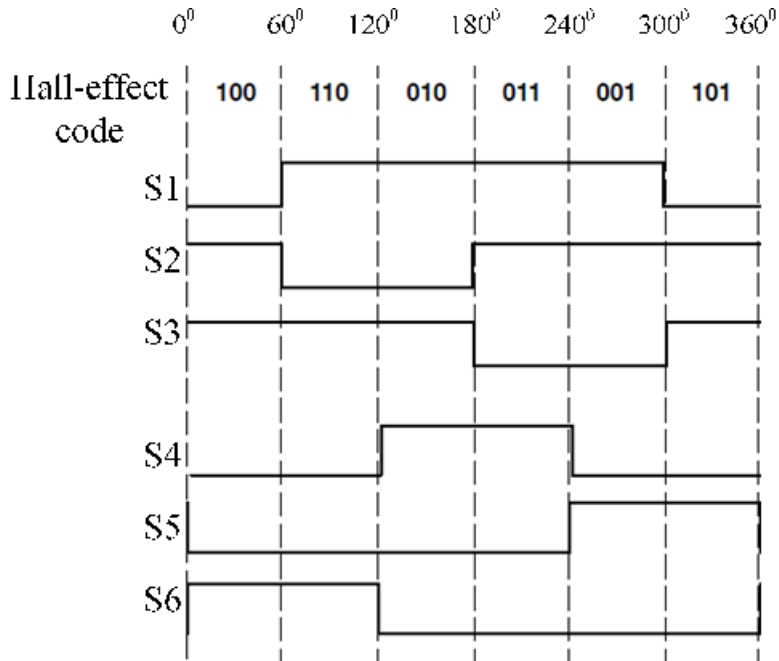


Figure 4.5: Sector evaluation with hall effect sensor

In Simulink it is implemented thanks to logical operators (figure 4.6). Compared to the figure 4.5 the angle goes from  $-180^\circ$  to  $180^\circ$  because the transformation from rad/s to degree is done through the arctangent function.

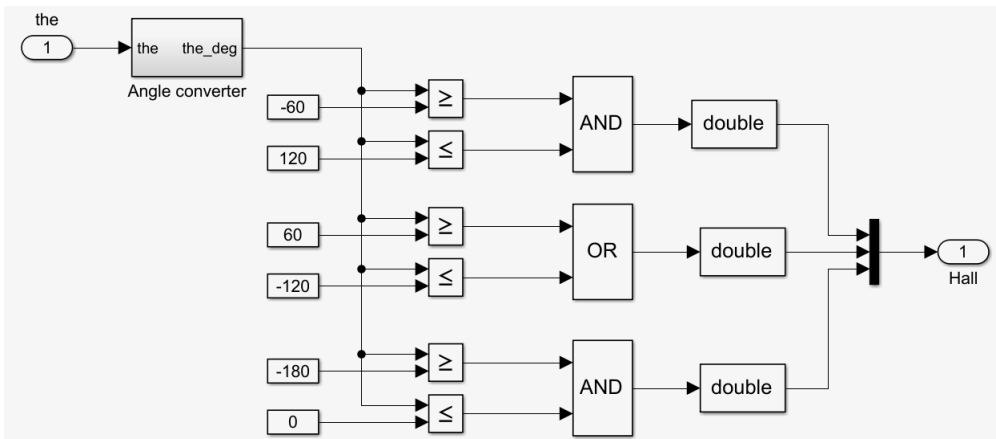


Figure 4.6: Hall effect sensor block

## 4.4 Torque Computation

As written in previous chapter the torque is calculated as:

$$T_e = \frac{e_A i_A + e_b i_B + e_C i_C}{\omega}$$

Which becomes:

$$T_e = p[\Psi_{pm,A} i_A + \Psi_{pm,B} i_B + \Psi_{pm,C} i_C]$$

In Simulink blocks becomes:

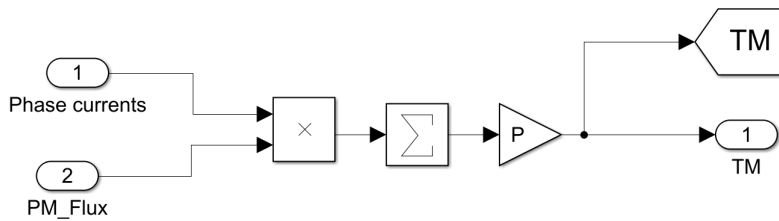


Figure 4.7: Torque computation

## 4.5 Inverter

The last part of the electromechanical model is out of the motor model and it is the inverter block.

The three phase inverter is built with six power MOSFET, two for each leg.

Each power switch has an internal diode in parallel with a series RC snubber circuit.

When a gate signal is applied the MOSFET conducts and acts as a resistance ( $R_{on}$ ) in both directions. If the gate signal falls to zero when current is negative, current is transferred to the antiparallel diode.

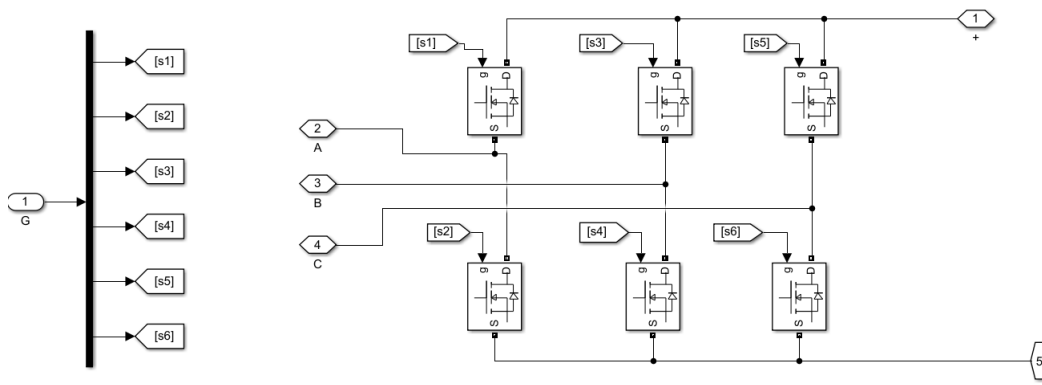


Figure 4.8: Inverter block

## 4.6 Simulation Results

From the specifications defined in Chapter 2 each motor must provide almost 1.25kW, 6.2Nm torque and 1895rpm.

Furthermore, the motor has to be compatible with the T-Motor FA36,2x11,8”.

To satisfy all this request the motor chosen U15II KV100.

Motor parameters	Value	Unit
Internal resistance	12	$m\Omega$
Weight	1740	g
Max power	9942	W
Synchronous Inductance	13	$\mu H$
Pole Pairs	21	

### 4.6.1 Open Loop

The open loop control strategy is driven by the decoder block and by the gates block.

The decoder block implements the following PWM command in relation with the hall effect input:

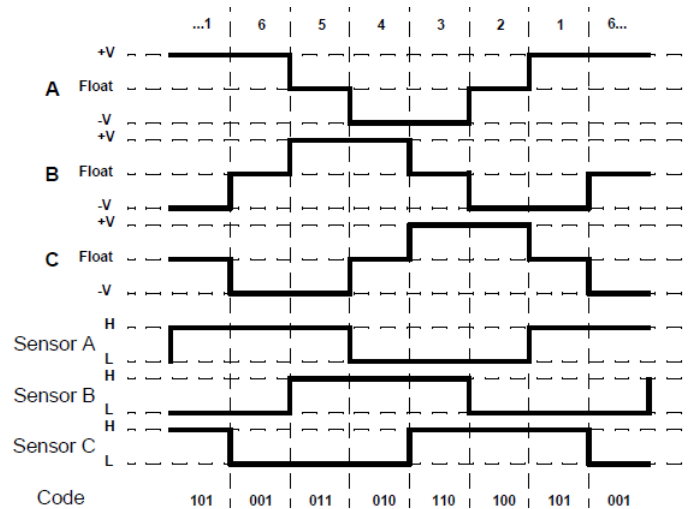


Figure 4.9: Decoder block

The second block instead generates the gate pulses. The pulses are generated by following the table 4.2.

$PWM_a$	$PWM_b$	$PWM_c$	Q1	Q2	Q3	Q4	Q5	Q6
0	0	0	0	0	0	0	0	0
0	-1	+1	0	0	0	1	1	0
-1	+1	0	0	1	1	0	0	0
-1	0	+1	0	1	0	0	1	0
+1	0	-1	1	0	0	0	0	1
+1	-1	0	1	0	0	1	0	0
0	+1	-1	0	0	1	0	0	1
0	0	0	0	0	0	0	0	0

Table 4.2: Gate state

This six states will drive the inverter. The response in speed and torque of the open-loop motor, without load and without propeller attached, to a step input are shown in figure 4.10 and 4.11.

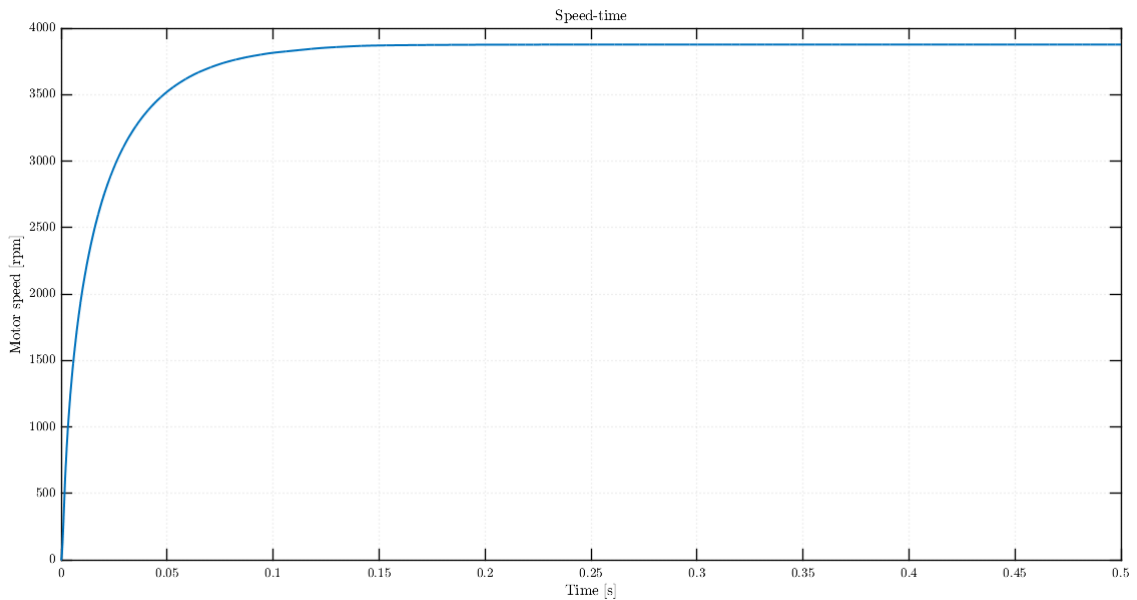


Figure 4.10: Speed response to a step in open loop

The speed response (figure 4.10) shows an over-damped system which reach the

steady state in 0.15s.

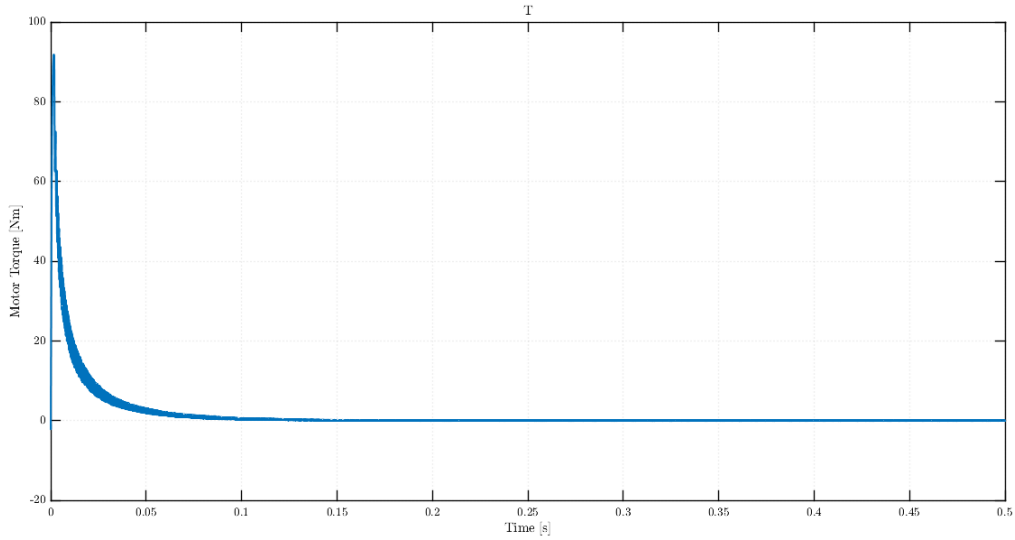


Figure 4.11: Torque response to a step in open loop

Figure 4.11 shows that motor torque is specular at speed, it has an initial spike and then a natural decay until it reaches zero in steady state conditions. After speed and torque is analyzed the current response to a step (figure 4.12).

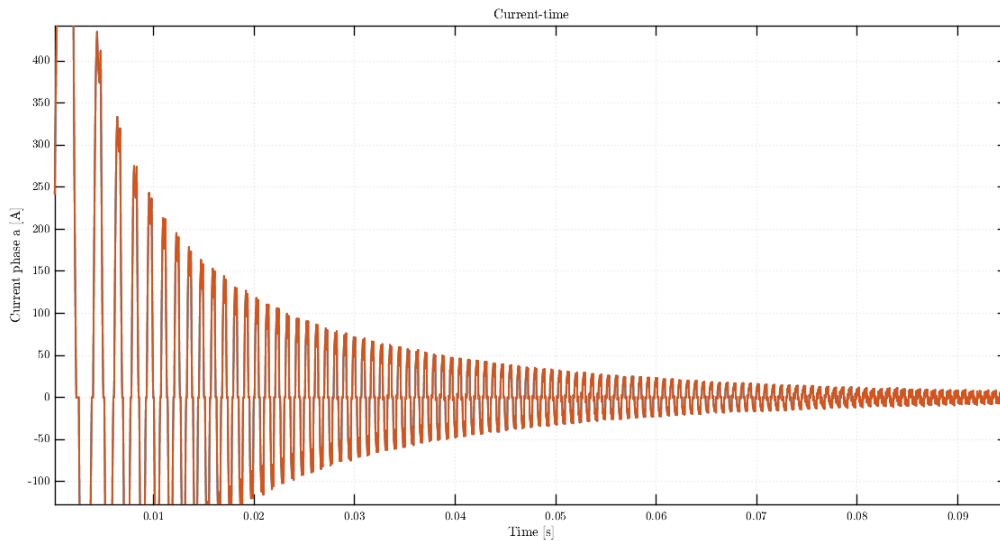


Figure 4.12: Current response to a step in open loop

The current, as the torque, hasn't any limitation so at the cue they have a very high

peak and they tend to zero in steady state.

An important feature which emerges from this graphics is the ripple which characterise both the current and the torque (figure 4.12 and 4.11).

The current shape is not a perfect rectangular wave because of the ripple that overlaps with the average value and because of the inductance that does not allow the current to rise and decrease instantaneously.

## 4.6.2 Characteristic

In order to fully characterize the motor are needed the torque-speed curve and the power-speed curve.

The mechanical characteristic is obtained from the open loop control, by imposing a gradually increasing load and going to see the generated torque value at steady state.

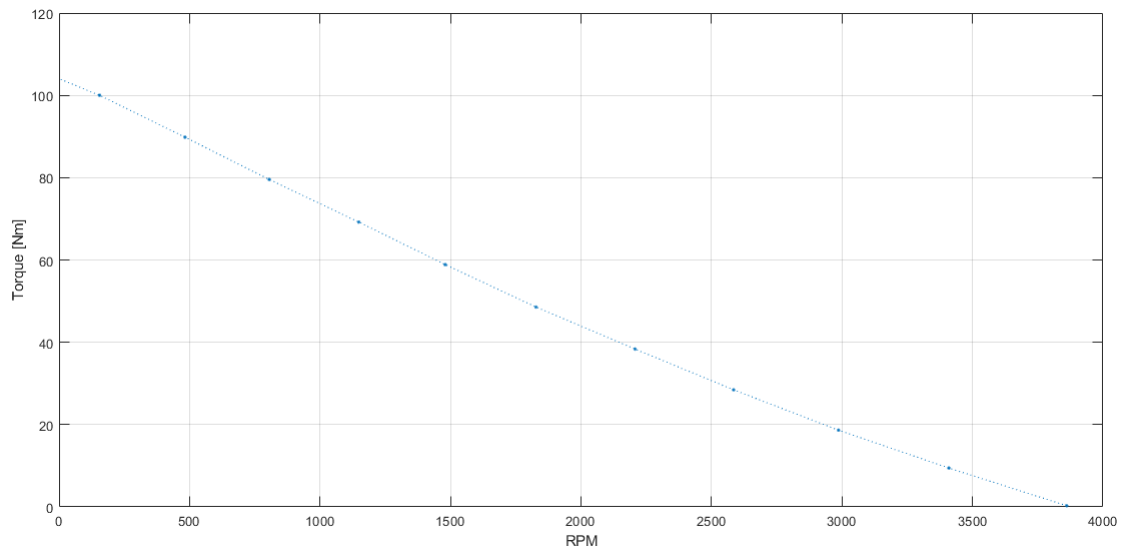


Figure 4.13: Mechanical characteristic

As shown in the ideal brushless DC characteristic in figure 3.7 also from the Simulink model the characteristic results linear and it is reported in figure 4.13.

From the characteristic we can define the stall torque and the maximum speed:

<b>Maximum speed</b>	3800	rpm
<b>Stall Torque</b>	105	Nm

### 4.6.3 Closed Loop with Trapezoidal Control

This control is widely used in low cost sensor-based application because it uses only three hall effect sensors to define the angular position of the rotor.

To close the loop the rotor speed is fed back, and the error between the reference speed and the feedback speed is the input of a PI regulator.

The controller generates the voltage reference for the DC link. Then the model is identical to the previous case of the open loop control.

To limit the overcurrent at the stall the reference speed is given as a ramp with a slope of 10000 rms/s.

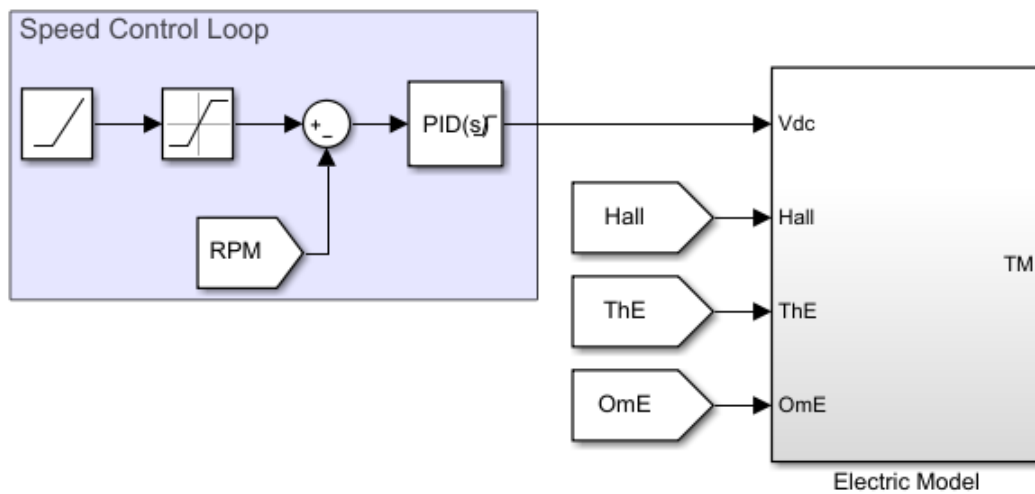


Figure 4.14: Speed regulator

From the propeller analysis we get the maximum speed of the motor so we can observe the response of the motor to the maximum speed.

Differently from the previous case in this analysis will be considered both the resistance load and the propeller inertia.

The load torque is provided from the propeller analysis (figure 2.3) and it is related to the motor speed.

In a first analysis the variable pitch is not considered and in the Simulink environment the resistant torque is chosen through a look up table.

### Speed Response to a Ramp

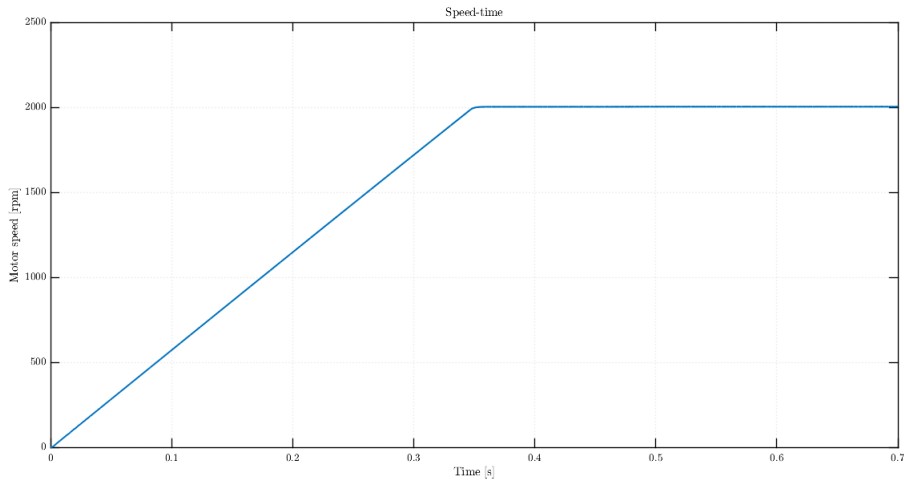


Figure 4.15: Speed response to a ramp in closed loop

Figure 4.15 shows that the motor follows well the reference ramp till the saturation once reached the maximum speed.

### Torque Response to a Ramp

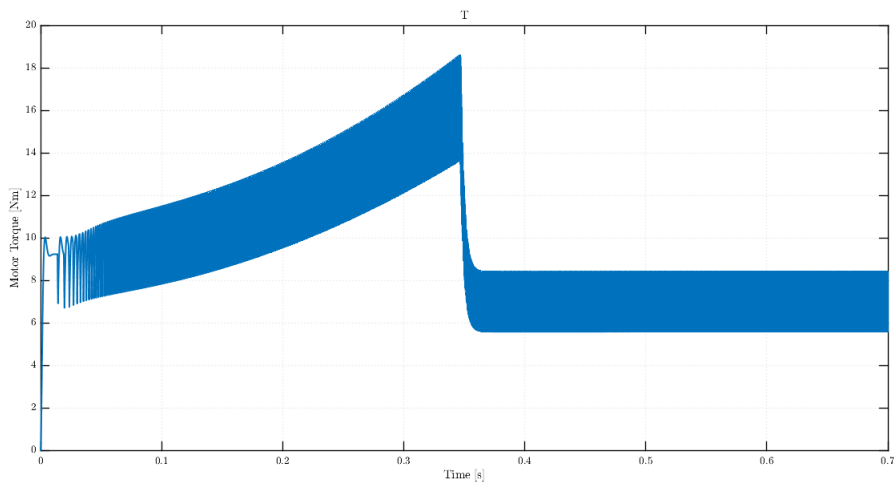


Figure 4.16: Torque response in closed loop

If the motor needs to accelerate the torque increases, once the speed becomes constant the torque drops and is adjusted to its steady state value. Figure 4.16 shows this trend which, however, is characterized by a strong ripple that overlaps with the average value.

### Current Response to a Ramp

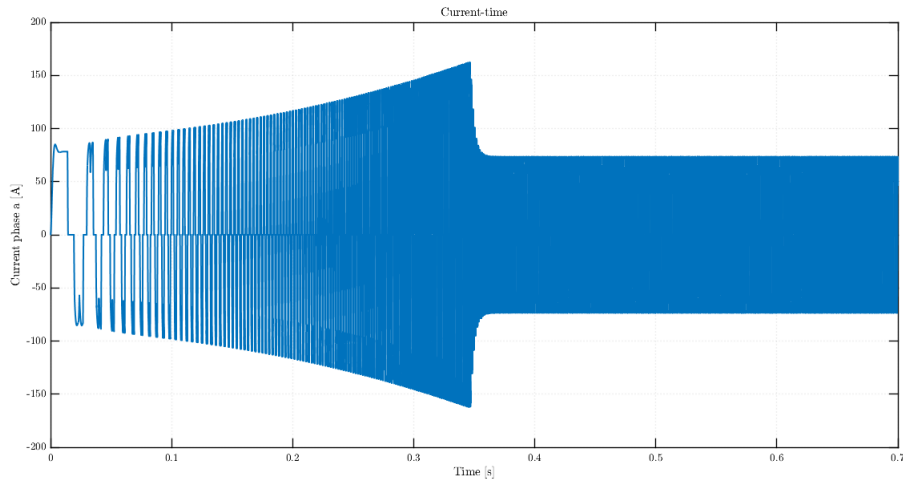


Figure 4.17: Current response to a ramp

The trend presented in figure 4.17 is similar to the torque one in figure 4.16, in fact the current amplitude increases until the motor reaches the maximum speed and then decreases up to the steady state value. Also, in this case the waveform is characterized by a ripple every 60 electrical degrees. The ripple is caused by the commutation of the phases which do not take the same time to switch and so for a short period during commutation there are three phases on instead of two.

### Power Response to a Ramp

To analyze the power required by the system is applied the method of the three wattmeters, because the waveforms are not sinusoidal, so the conventional formulas are not worth. This method consists in the summation of the instantaneous product between the phase voltage and the phase current:

$$P_{inst} = v_{1n}i_1 + v_{2n}i_2 + v_{3n}i_3 \quad (4.2)$$

The active power is the mean value of  $P_{inst}$ .

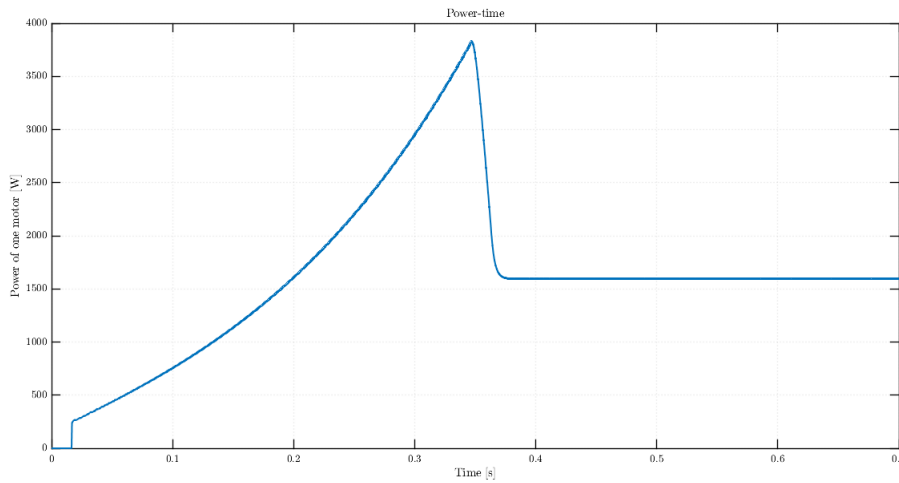


Figure 4.18: Power response to a ramp

$$P_{max} = 3800W$$

#### 4.6.4 Hysteresis Control

To correct the problem of the torque ripple is analyzed another control technique which is based on current regulators.

The philosophy of this control technique is to drive the inverter with the output of the hysteresis regulator, which compare the feedback current with the reference one.

The purpose of the control is to make the feedback current follow the reference current. Reference currents depend on the operating position of the rotor, which can be detected by the hall sensors, and they have to be synchronized with the back emf of their phases to produce constant torque (figure 4.19).

The amplitude of the reference current is provided by the output of the speed regulator, which receives in input the error between reference speed and feedback speed.

The speed regulator is a PI regulator with the output saturated.

The output of the speed regulator is the reference torque and it is saturated at 13Nm which is the torque associated to the maximum current.

Dividing the torque for the motor torque constant is obtained the reference current amplitude.

Each phase reference current is scaled to the value of the reference current amplitude and are send to the hysteresis regulator.

The hysteresis regulator gives a low output when the error between feedback current and reference current is higher than the hysteresis band. On the contrary it gives a high output when the error is lower than the hysteresis band (figure 4.20).

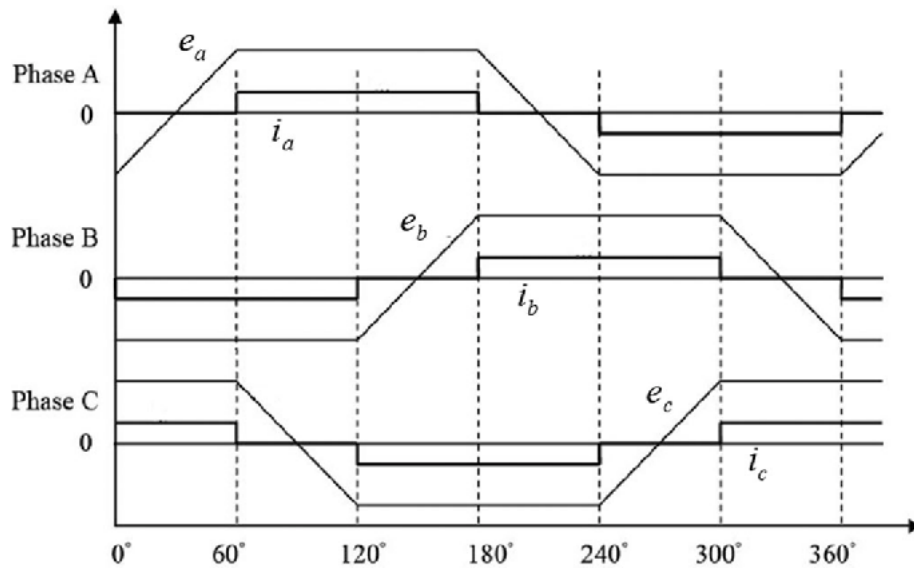


Figure 4.19: Reference current

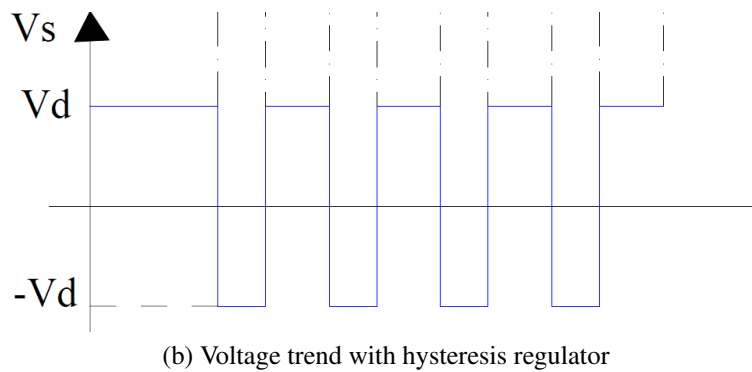
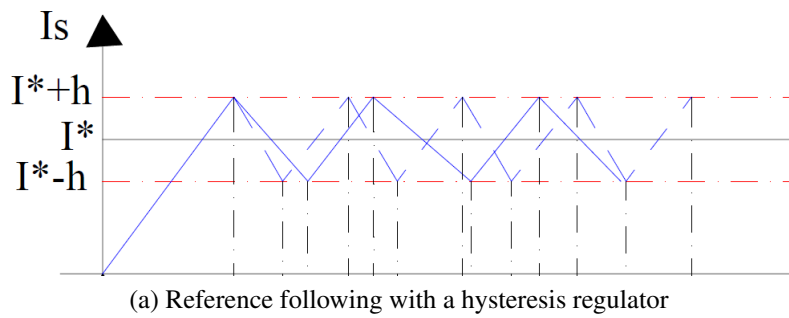


Figure 4.20: Inverter's current and voltage behaviour with an hysteresis regulator

The hysteresis output drive the gates of the inverter's MOSFET in the following way:

$$i > I_{ref} + h \longrightarrow \text{switch off}$$

$$i > I_{ref} - h \longrightarrow \text{switch on}$$

where:

$h$  — hysteresis bandwidth;

In this way when the power switch is on there is a positive voltage supply vice versa when the power switch is of there is a negative voltage supply.

### Speed Response to a Ramp

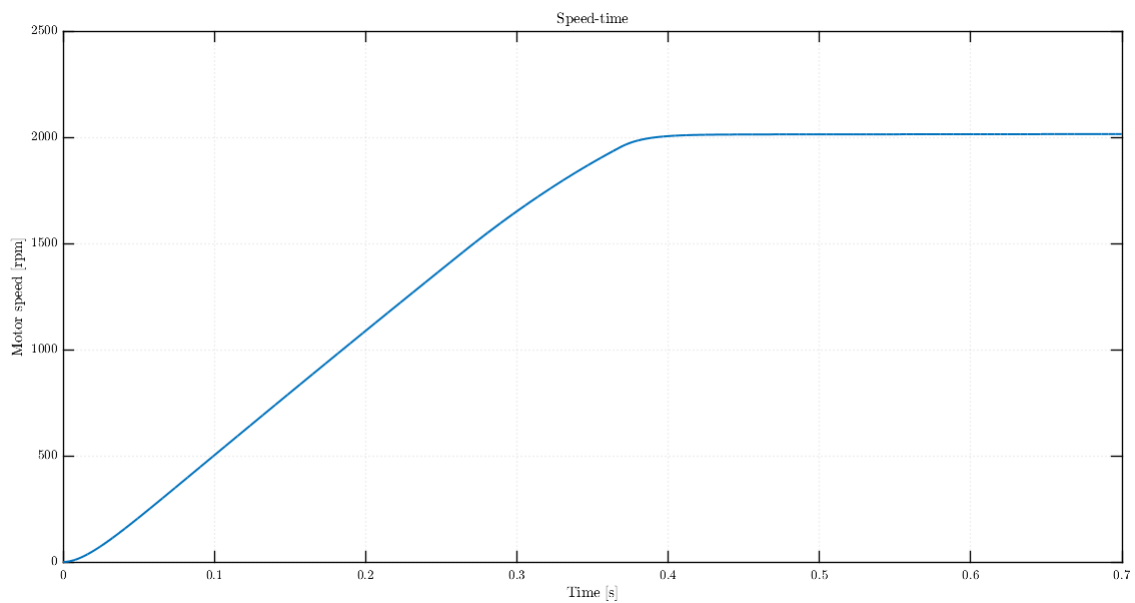


Figure 4.21: Speed response to a ramp in closed loop with hysteresis control

The speed performance presented in figure 4.21 is very similar to the one provided for the trapezoidal control (figure 4.15), in fact the reference ramp is well followed by the motor speed which rises till maximum value in almost the same time.

This is a good result because the good acceleration of the motor is maintained.

### Torque Response to a Ramp

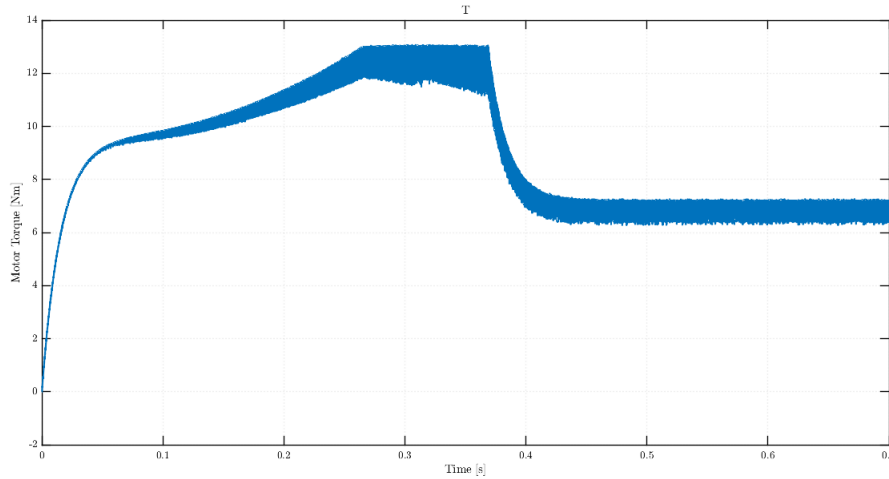


Figure 4.22: Torque response to a ramp in closed loop with hysteresis control

Figure 4.22 shows that the torque increase but at a certain time it saturates and maintains that value until the motor speed has reached its maximum value. After which, as in the previous case (figure 4.16), the torque decreases up to the steady state value.

### Current Response to a Ramp

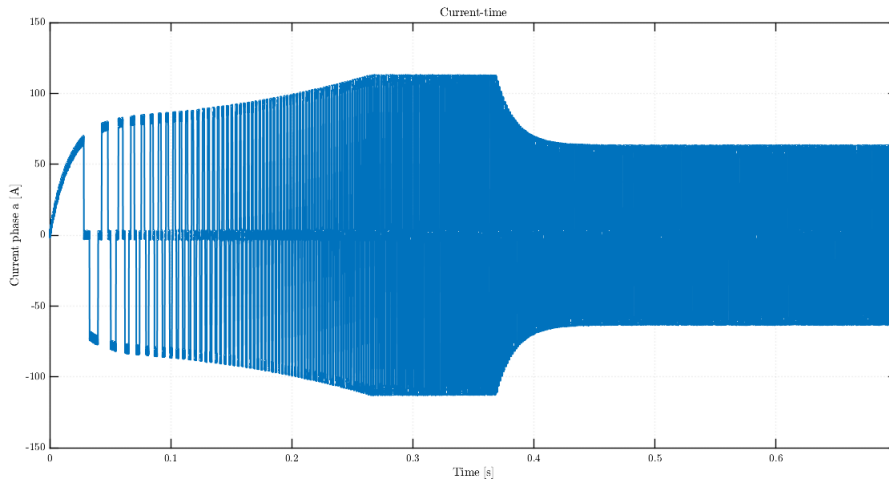


Figure 4.23: Current response to a ramp in closed loop with hysteresis control

As the torque also the current rises till its maximum value where it is saturated. When the motor stop to accelerate and the speed becomes constant the current descends to its

steady state value. From figure 4.22 and 4.23 also with this kind of control both the torque and the current are subjected to a ripple.

### Power Response to a Ramp

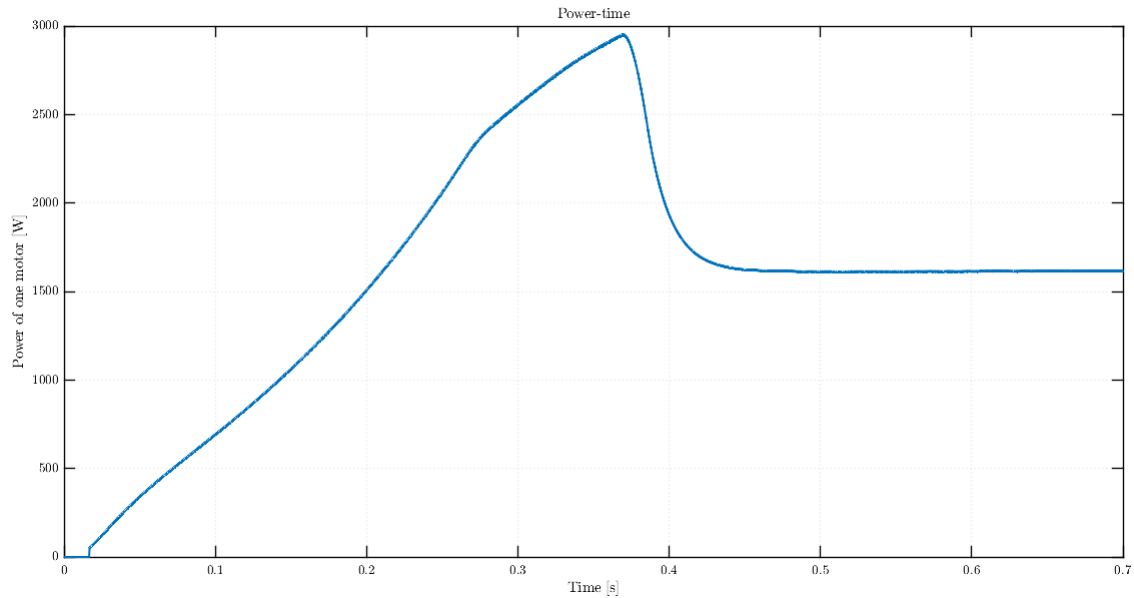


Figure 4.24: Power response to a ramp in closed loop with hysteresis control

Power is calculated as in the previous case with the method of three wattmeters. In this case the maximum power results:

$$P_{max} = 2900W$$

## 4.7 Result Comparison

### Current Comparison

As shown in the figure 4.25 the red trend is the phase current with hysteresis regulator, the blue one is the phase current without hysteresis regulator.

The current ripple is changed from more than 20A to less than 5A.

About the current is possible to see in figure 4.26 that with the second type of control has not only a lower ripple but also the current is saturated by the speed regulator, in fact after reaching 120A amplitude the current doesn't grow anymore.

For this reason the dynamic of the motor with the hysteresis current regulator will be more slow.

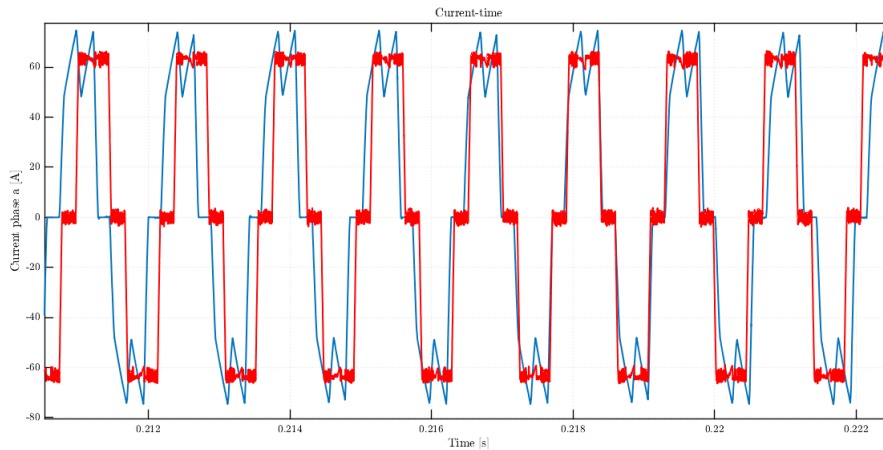


Figure 4.25: Current comparison with and without hysteresis current regulator

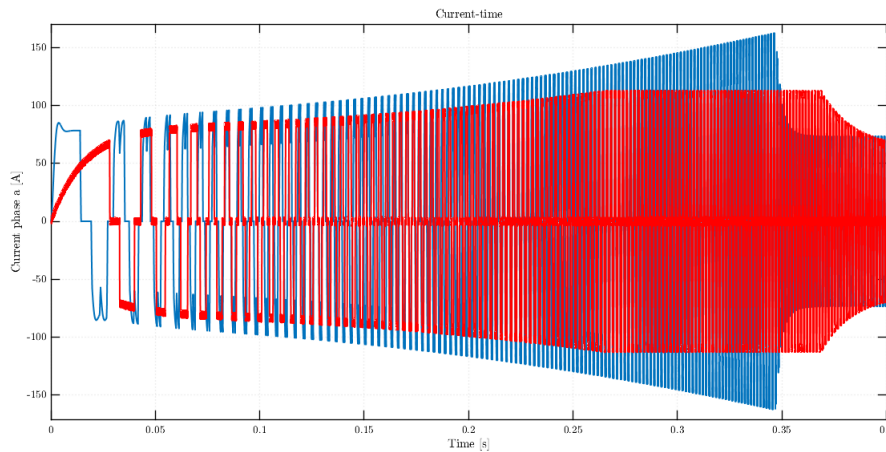


Figure 4.26: Current comparison with and without hysteresis current regulator

### Torque Comparison

As a direct consequence of the reduced current ripple the torque ripple is reduced. The red line is the trend of the torque with current hysteresis regulator and the blue one is the torque without current regulator.

Is possible to see that the ripple is much better with hysteresis controller, and it pass from almost 3Nm to less than 1Nm.

Because of the slower dynamic of the motor the torque reaches the steady state after more time than in the previous case but it has also a lower peak.

On the other hand, the lower dynamic of the motor leads to a lower power requirement, so the power peak is lower with hysteresis control.

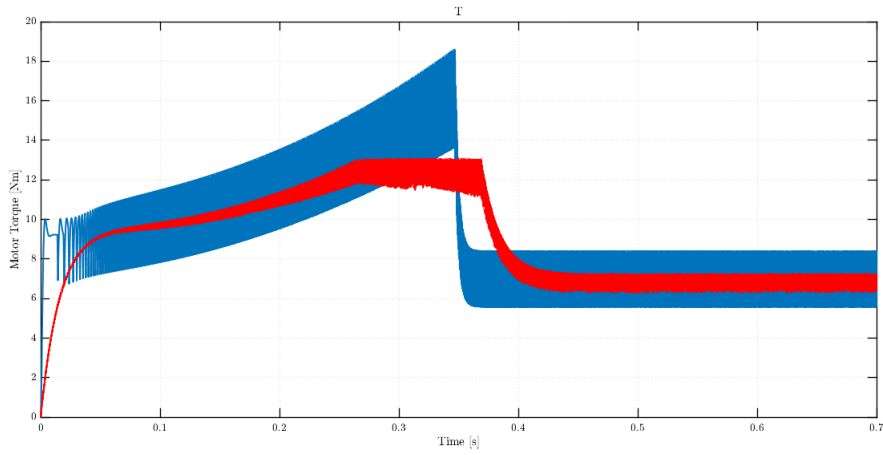


Figure 4.27: Current comparison with and without hysteresis current regulator

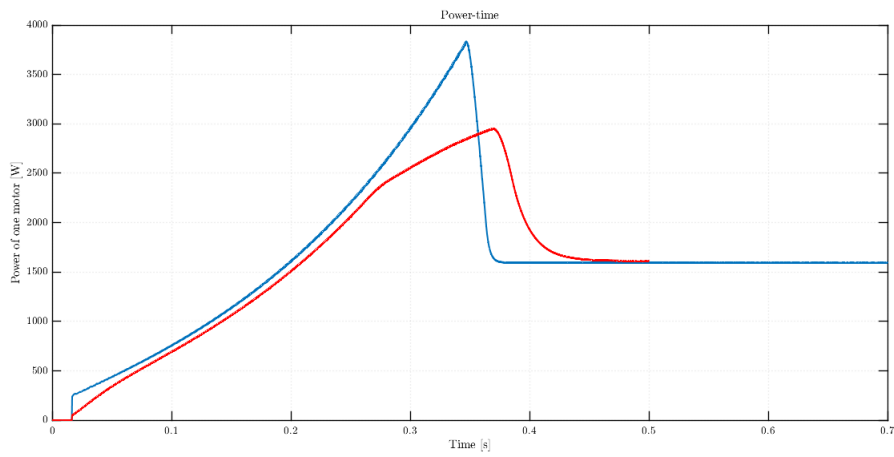


Figure 4.28: Power comparison with and without hysteresis current regulator

# Chapter 5

## Quadcopter Simulation

After the realization of the model of one electromechanical actuator, it is added four times in the overall system of the tethered drone in order to model the propulsion system.

The aim of this chapter is to check the behaviour of the system in operative conditions. In the first part there is the model blocks description. Then will be analyzed dynamic performance and the trends of the power required by the propulsion system at various heights.

### 5.1 Notation and Assumptions

The simulation is made with the following notation and under the following assumptions.

#### Notations

- $N - E - D$ : Position is expressed in N,E,D frame;
- $X_b, Y_b, Z_b$ : Position is expressed in body frame;
- $u, v, w$ : Velocity expressed in body frame;
- $p, q, r$ : Body angular rate;
- $\Phi, \Theta, \Psi$ : Euler angle;
- $T_p, C_p$ : Thrust and torque control vector;
- $l$ : Quadrotor arm;
- $q$ : Quaternion vector;
- $g$ : Gravity acceleration in NED frame;

### Assumptions

- The quadcopter has X quadrotor frame;
- The quadcopter has geometric and inertial symmetry;
- Earth is considered flat;
- The cable model has some simplifying hypotheses: the cable attached to the NED origin and UAV center of gravity and cable is considered always taut.
- The angular speed convention of the UAV are shown in figure 5.1



Figure 5.1: Angular speed convention

## 5.2 Model Description

The system is composed by five main blocks which makes the aerial system. This blocks are:

- Autopilot
- Electromechanical actuators
- Quadcopter dynamics
- Navigation and sensors

- Tether cable

The following blocks will not be described in detail because they are not specific topics of this thesis.

### 5.2.1 Autopilot

This system consists of two blocks: the controller and the motor mixer. The controller returns the desired thrust and control torque instead the motor mixer divides the desired value of thrust and torque among the four motors.

#### Controller

Block Input	Variable	Unit	Dimension	Note
<i>Desired position</i>	$p_{des}$	m	Vector 3xN	N is the total number of desired waypoint. The desired position is given in NED reference frame
<i>Current position</i>	$p_{true}$	m	Vector 3x1	Current position in NED frame computed by Navigation Equations
<i>Quadcopter NED velocity</i>	$v_n$	m/s	Vector 3x1	NED reference frame
<i>Quadcopter body velocity</i>	$v_b$	m/s	Vector 3x1	Body reference frame
<i>Attitude (Euler Angle)</i>	$att$	rad	Vector 3x1	-
<i>Stabilize mode flag</i>	$atti$	-	Scalar 1x1	Flag to activate attitude control

Block Output	Variable	Unit	Dimension	Note
<i>Desired thrust</i>	$T_z$	N	Scalar 1x1	-
<i>Control roll torque</i>	$\tau_R$	Nm	Scalar 1x1	-
<i>Control pitch torque</i>	$\tau_P$	Nm	Scalar 1x1	-
<i>Control yaw torque</i>	$\tau_Y$	Nm	Scalar 1x1	-

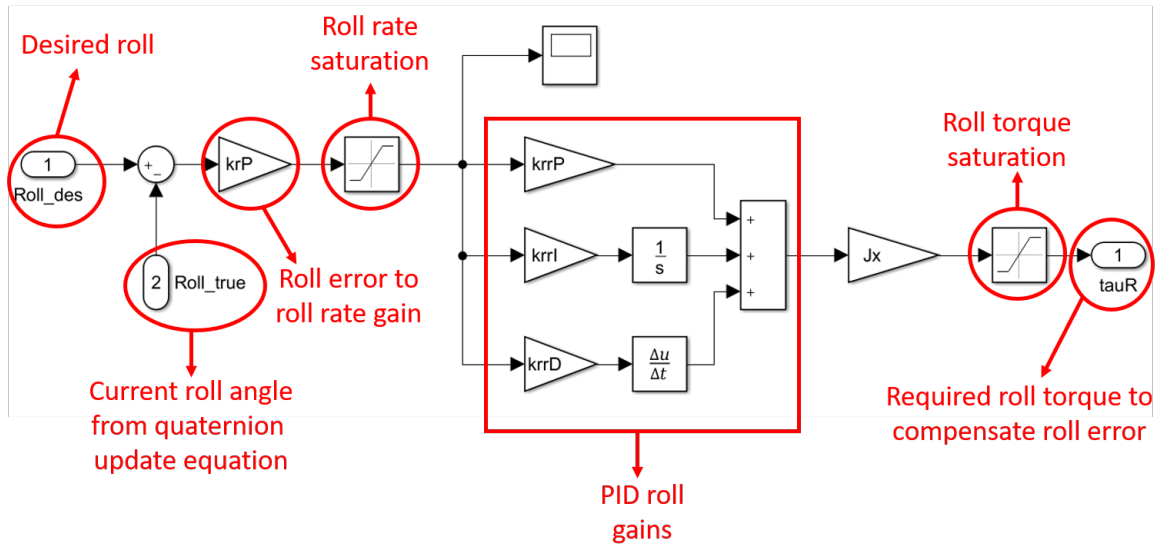


Figure 5.2: Roll Controller

The most important blocks of the controller are the attitude controller, the altitude controller and the position controller.

### Attitude Controller

The attitude controller is divided in three parts: the roll controller, the yaw controller and the pitch controller. They all have the same structure and the aim of each one is to guarantee the desired attitude to the drone.

The core of this controller is a PID regulator. In figure 5.2 is shown the roll controller.

### Altitude controller

This controller aim is to guarantee that the quadrotor maintains the desired altitude. As in the attitude controller the core of the controller is a PID regulator. The structure of this controller is shown in figure 5.3.

### Position Controller

This block is divided in two parts: the forward controller and the lateral controller. The first provides the desired pitch, the second provides the desired roll. In fact, this block guarantees that the quadrotor remains at the desired NED position. Position control is called the outer loop, because it provides to the attitude controller the desired roll, pitch and yaw angle. This block is fundamental because to move in a desired position

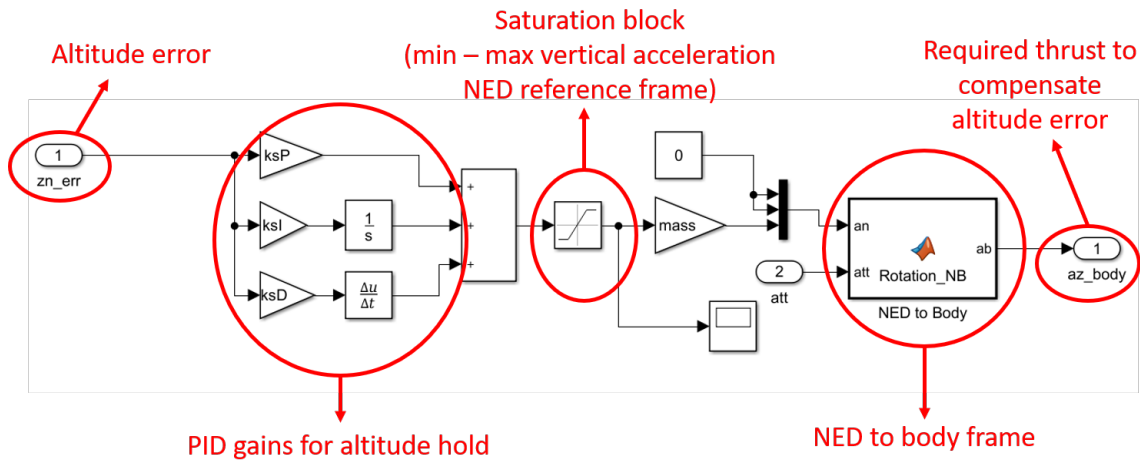


Figure 5.3: Altitude Controller

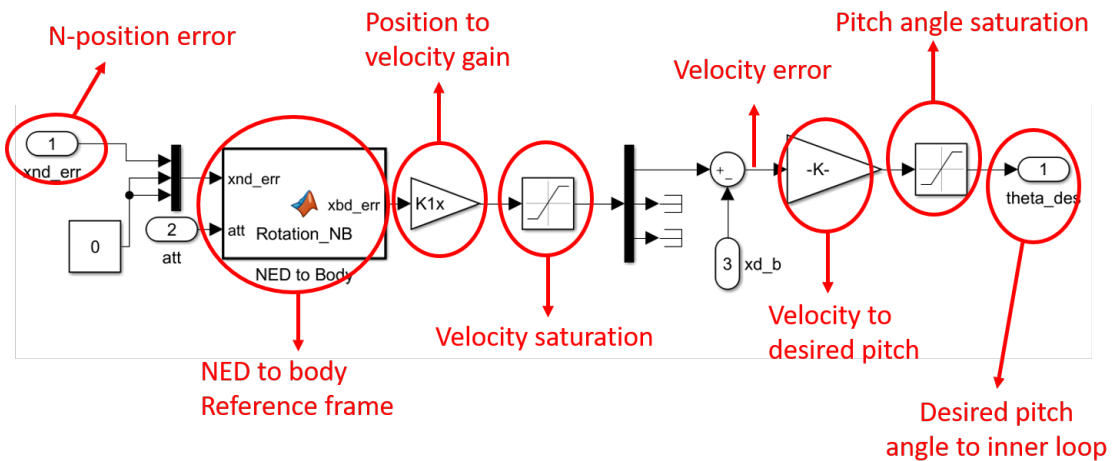


Figure 5.4: Forward Controller

the copter needs precise angle of roll and pitch.

In figure 5.4 is presented the forward controller which provide the desired pitch.

### Motor Mixer

The motor mixer receives as inputs the desired thrust and the three control torques.

The result of this block is the thrust required of each propeller to obtain the performances required by the controller.

Block Input	Variable	Unit	Dimension	Note
<i>Desired thrust</i>	$T_z$	N	Scalar 1x1	-
<i>Control roll torque</i>	$\tau_R$	Nm	Scalar 1x1	-
<i>Control pitch torque</i>	$\tau_P$	Nm	Scalar 1x1	-
<i>Control yaw torque</i>	$\tau_Y$	Nm	Scalar 1x1	-

Block Output	Variable	Unit	Dimension	Note
<i>Required thrust of propeller</i>	$T_p$	N	Vector 4x1	-
<i>Torque of each propeller</i>	$C_p$	Nm	Vector 4x1	-

The thrust of each propeller is calculated as:

$$T_{p1} = \frac{T_z}{4} + \frac{\tau_P}{l} - \frac{\tau_R}{l} \quad (5.1)$$

$$T_{p2} = \frac{T_z}{4} - \frac{\tau_P}{l} + \frac{\tau_R}{l} \quad (5.2)$$

$$T_{p3} = \frac{T_z}{4} + \frac{\tau_P}{l} + \frac{\tau_R}{l} \quad (5.3)$$

$$T_{p4} = \frac{T_z}{4} - \frac{\tau_P}{l} - \frac{\tau_R}{l} \quad (5.4)$$

$$C_{p1} = C_{p2} = -\frac{\tau_Y}{4} \quad (5.5)$$

$$C_{p3} = C_{p4} = \frac{\tau_Y}{4} \quad (5.6)$$

Where:

$l$  — is the distance between the rotor and the center of mass of the UAV;

## 5.2.2 Electromechanical Actuators

This is the propulsion system of the vehicle and it mainly consist in four electromechanical actuators identical to those presented in Chapter 4.

There is some difference which are related to the input and output data.

In fact, in this model the input results from the motor mixer is a reference thrust and not a reference speed like in the previous electromechanical model.

So is needed a passage from thrust to speed and it is realized starting from the thrust-pitch-speed map in figure 2.9.

On the Simulink environment a MATLAB function receives as input the desired torque and results the maximum speed with the minimum pitch provided by the map.

The function results the minimum pitch in order to minimize the load torque. In fact, the resistant torque applied to the motor is extrapolated, with a 2-D look up table (LUT), from torque-pitch-speed map in figure 4.2 where is shown that the smaller the pitch the smaller is the resistant torque. Instead if we want to increase the acceleration and perform a more aggressive flight we have to maximize the pitch, in this way the rising time of the vehicle will be faster but on the other hand the load torque will be maximized and the power request will grow.

The pitch is one of the main differences respect the previous model analyzed in Chapter 4, as a matter of fact it wasn't considered and it affects both the input and the output of the system.

The output of the previous electromechanical actuator was a speed, but the overall system requires a thrust as result from the motor and the propeller so, as for the input, is needed the calculation of the thrust. The required thrust is extrapolated from figure 2.9 thanks to a 2-D LUT.

The single actuator model is shown in following figure:

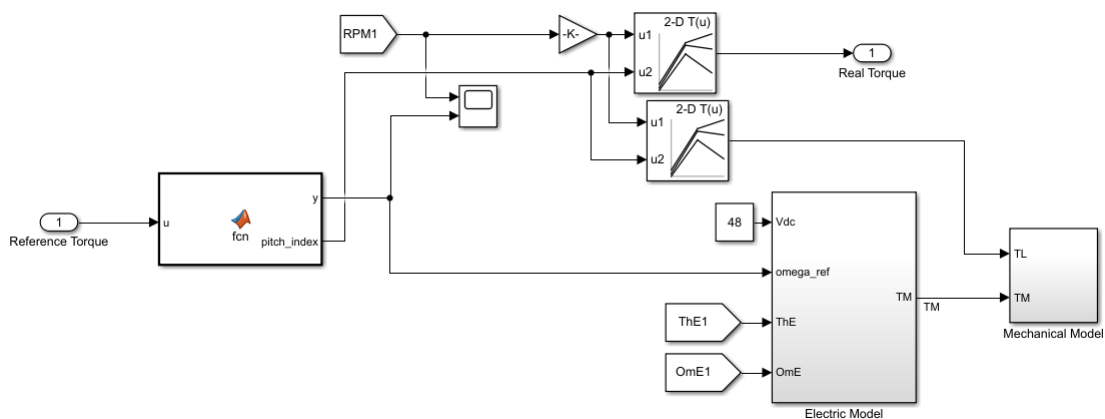


Figure 5.5: Single electromechanical actuator

### 5.2.3 Quadcopter dynamics

In this block there are two MATLAB functions which implement the translation dynamic equations and the rotational dynamic equations in body frame.

The equations derives from the Newton's law under the following hypothesis:

- Propeller forces are always along z-body axis

- The inertia matrix is constant and diagonal because of geometrical and inertial symmetry

$$\begin{cases} \dot{u} = rv - qw - g \sin \theta + T_{cableX} \\ \dot{v} = pw - ru + g \sin \Phi \sin \theta + T_{cableY} \\ \dot{w} = qu - pv + g \cos \Phi \cos \theta + \frac{1}{m} \sum_{i=1}^4 T_{pi} + R_v + T_{cableZ} \end{cases} \quad (5.7)$$

$$\begin{cases} \dot{p} = \frac{1}{J_x} [(T_{p2} + T_{p3} - T_{p1} - T_{p4}l + qr(J_y - J_z))] \\ \dot{q} = \frac{1}{J_y} [(T_{p1} + T_{p3} - T_{p2} - T_{p4}l + pr(J_z - J_x))] \\ \dot{r} = \frac{1}{J_z} [(C_{p3} + C_{p4} - T_{p1} - T_{p2}l + pq(J_x - J_y))] \end{cases} \quad (5.8)$$

where:

$$\begin{cases} R_v = -mg, \text{ if altitude} \sim 0 \\ R_v = 0, \text{ if altitude} > 0 \end{cases}$$

The output of this block is the translational acceleration in body reference frame and the body angular rate computed at the previous step time.

## 5.2.4 Navigation and Sensors

This block is composed by an Inertia Measurement Unit (IMU), navigation equations and an altimeter.

Block Input	Variable	Unit	Dimension	Note
<i>Translational acceleration</i>	<i>acc</i>	<i>m/s<sup>2</sup></i>	Scalar 3x1	body reference frame
<i>Body angular rate</i>	<i>ω</i>	rad/s	Scalar 3x1	Computed at the previous step time

Block Output	Variable	Unit	Dimension	Note
<i>Translational velocity</i>	<i>v<sub>b</sub></i>	m/s	Vector 3x1	Body reference frame
<i>Translational velocity</i>	<i>v<sub>n</sub></i>	m/s	Scalar 3x1	NED reference frame
<i>Translational position</i>	<i>p<sub>n</sub></i>	m	Scalar 3x1	NED reference frame
<i>Euler angle</i>	<i>EA</i>	rad	Vector 3x1	-
<i>Altitude</i>	<i>alt</i>	m	Scalar 1x1	-

### 5.2.5 Tether cable

This block provides a simple modellization of the tether cable. The block calculates the centre of gravity by subtracting the cable anchor point from the quadcopter NED position, the module of the result is the cable length.

$$l_{cable} = \|p_n - p_{cable}\| \quad (5.9)$$

The result of the subtraction divided for its module results the unit vector of the force that the cable exercise on the UAV.

$$n_{cable} = \frac{p_n - p_{cable}}{\|p_n - p_{cable}\|} \quad (5.10)$$

Multiplying  $l_{cable}$  for the cable weight per unit length, for  $g$  and for  $n_{cable}$  is obtained the cable forces applied to the centre of gravity of the UAV.

Block Input	Variable	Unit	Dimension	Note
<i>Quadcopter NED position</i>	pn	m	Vector 3x1	-
<i>Cable anchor point</i>	pcable	m	Vector 3x1	NED reference frame
-	cable flag	-	Scalar 1x1	Flag to enable cable simulation

Block Output	Variable	Unit	Dimension	Note
<i>Cable force</i>	Tcable	N	Vector 3x1	Body reference frame

## 5.3 Results

To verify the behaviour of the system in operating conditions are simulated 3 different working situation of the vehicle, maintaining constant the north, east condition at 0.5m and -0.5m respectively:

- At 10m in height
- At 50m in height
- At 100m in height

The north and east component are kept constant because the application mainly foresees displacements in the down direction while in the other two directions only small displacements.

The vehicle mass is considered of 25kg plus the variable mass of the cable. The mass of the cable depends on the working altitude.

This simulation is important because based on the results obtained will be sized the power cable and the power electronics aboard and off board.

The most important results of this simulation are:

- The power request in different working condition and in particular in worst case condition, at the maximum altitude;
- The dynamic response of the vehicle under different input conditions;

Let's start analyzing the multicopter performance when the required height is 10m.

The behaviour of the quadcopter with a desired position of  $[0.5, -0.5, -10]$  in NED reference frame is showed in figure 5.6.

The system reaches the steady state condition at 12s but is possible to see that before 2s

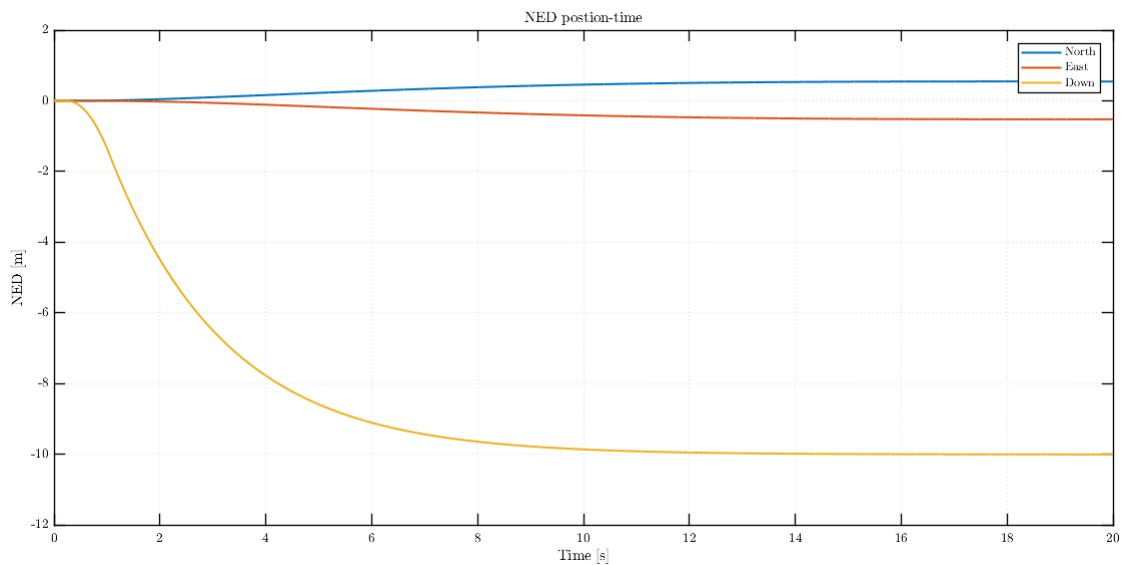


Figure 5.6: Quadcopter behaviour with  $NED=[0.5, -0.5, -10]$  input

the down line has an inflection point and the trend of the line is almost hyperbolic. This trend is setted by the controller, it could be faster or slower in relation to the tuning of the altitude controller gain. In the present simulation the response to the inputs could have been faster but then it would have had problems of instability in operating conditions at greater heights e.g. at 50 or 100m. So, a slower response was preferred but that still leads to an acceptable performance.

The north and east component are slower but they also reach the steady state at 12s.

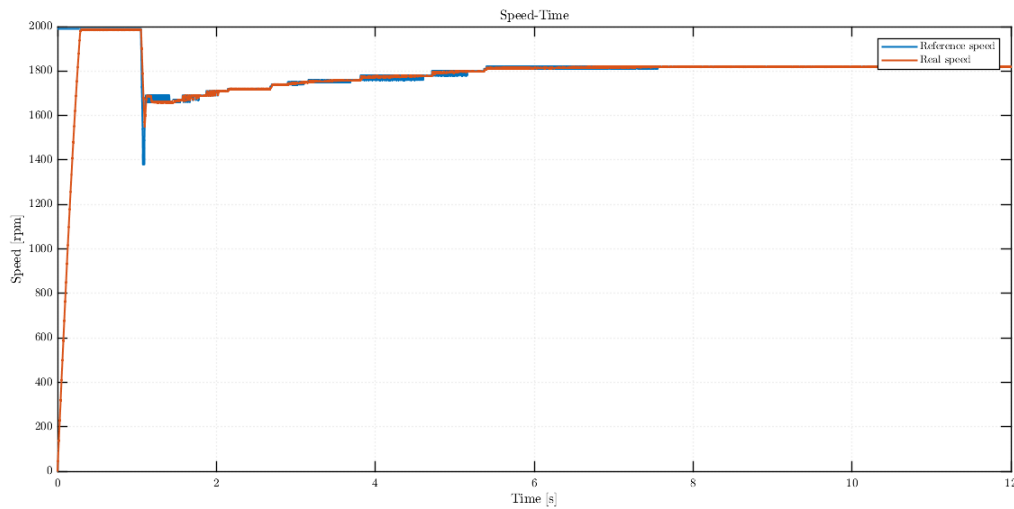


Figure 5.7: Speed trend with NED=[0.5,-0.5,-10] input

The following analyzes are performed until the steady state condition is reached because the values are constant afterwards.

Before analyzing the power consumption is useful analyze the speed required to each motor of the quadcopter (figure 5.7).

In the very first time we see the quadcopter motor that accelerates till reaching the reference speed and so the thrust required by the motor mixer. In this phase the reference speed is set to the maximum in order to obtain the maximum thrust.

Once reached the maximum speed this is maintained for a certain period, then falls because the autopilot set a lower thrust.

After the speed slowly rises up to its steady state value. As said previously speed is

<b>Maximum Power</b>	11680	W
<b>Power at hover at 10m</b>	3100	W

Table 5.1: Power results summary

related to thrust and in figure 5.8 is shown its trend. Is possible to see that at steady state the thrust required to each motor is 63N, which multiplied by 4 is the gravity force of the UAV and cable.

To higher speed correspond higher thrust and vice versa. Since the down reference use negative value, the related thrust has always to be negative.

Now it is possible to analyze the power consumption of the system in this working operation (figure 5.9). The power grows rapidly in the first moments as the speed till touching its maximum. Then, once the speed reached the reference the motor stops accelerating, the power falls and remains constant for a period until the required thrust has a drastic

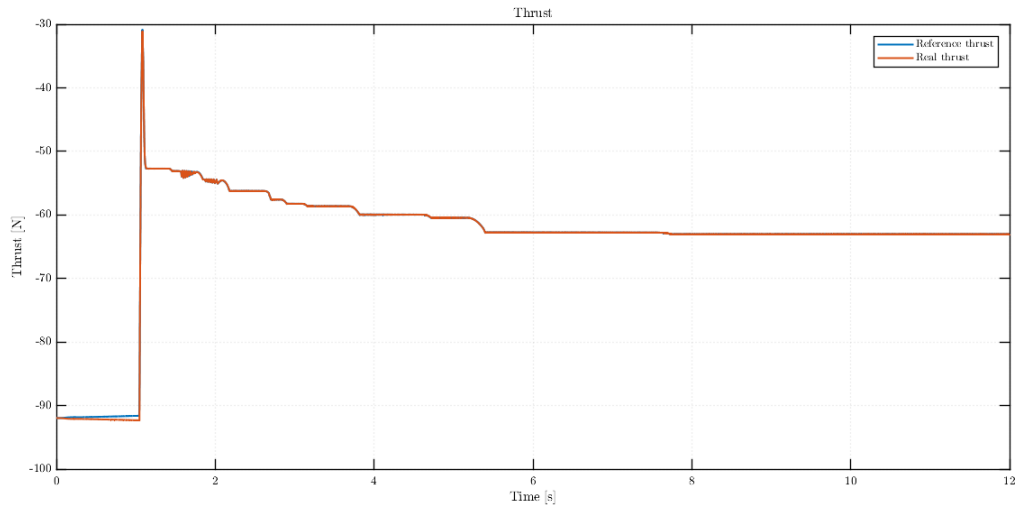


Figure 5.8: Thrust trend with NED=[0.5,-0.5,-10] input

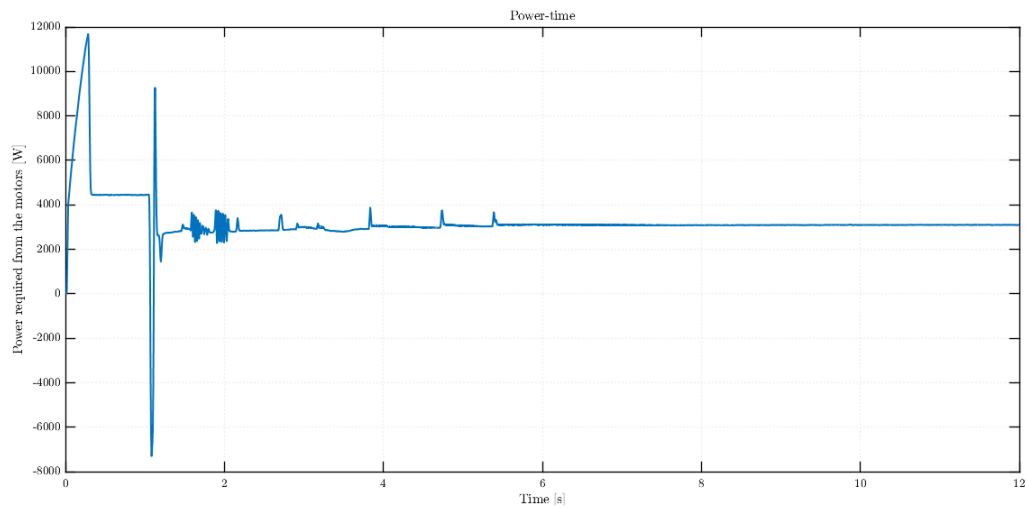


Figure 5.9: Power trend with NED=[0.5,-0.5,-10] input

drop and this translates in power into a spike of negative, which means a sudden deceleration. The power becomes negative because is required a negative torque with a positive speed, so in this phase the motor is doing a regenerative braking. Following the controller command after the drastic drop the thrust restart growing so there is a positive power spike, which causes a positive increment in reference speed, and then power slowly grow till its steady state value. After analyzing the operating conditions at a height of 10m, other working conditions are analyzed: 50m and 100m.

Starting from the dynamic response in position to an input of NED=[0.5,-0.5,-50] and the NED=[0.5,-0.5,-100] (figure 5.10). The multicopter has a good dynamic and it reach

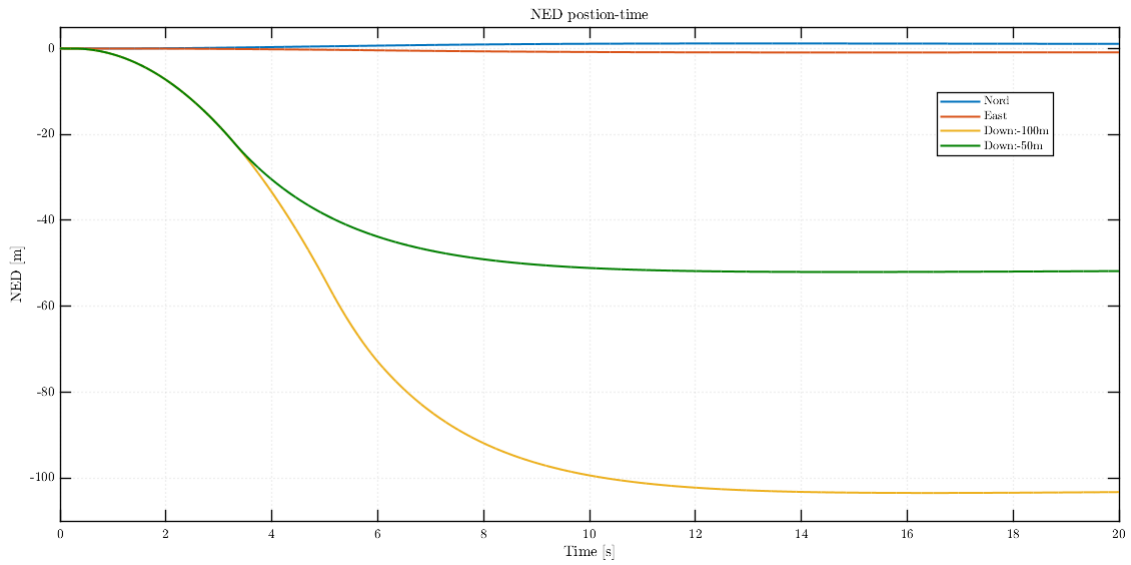


Figure 5.10: Dynamic response with different NED input

the steady states condition in almost 15 seconds in both cases.

The main difference between the operating heights is the required thrust from the autopilot, in fact the higher is the desired position the longer the autopilot maintains the request of maximum reference thrust (figure 5.11). The graph in figure 5.11 show well that the

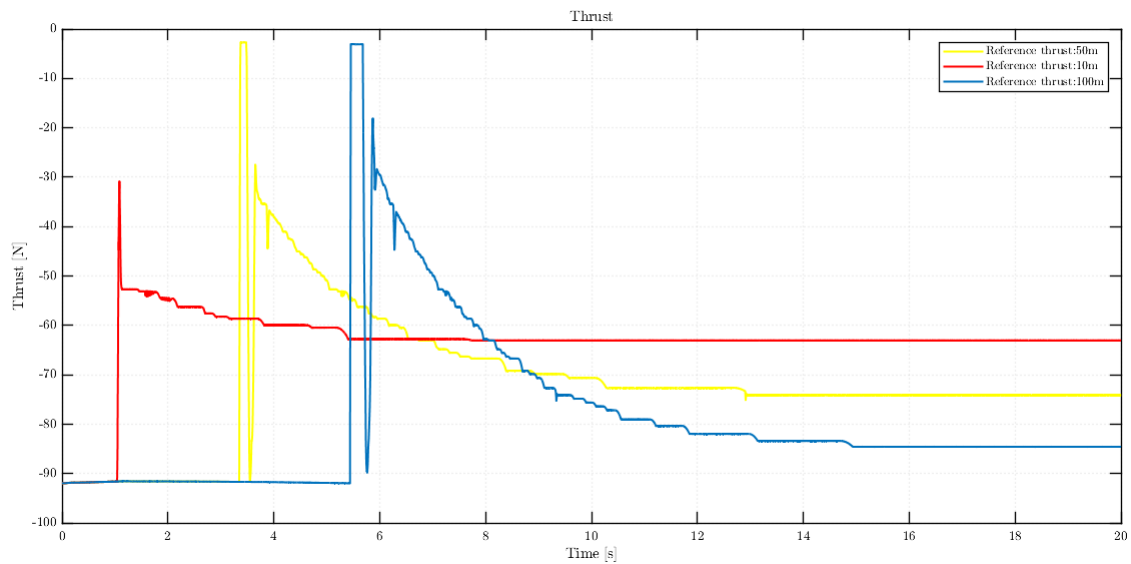


Figure 5.11: Comparison between reference thrust with different desired altitude

higher the UAV flies the more the power tether weights and then the required thrust in steady state takes into account also of this variable. The thrust request influence directly

the speed (figure 5.12) and the power request too (figure 5.13). Is important to underline

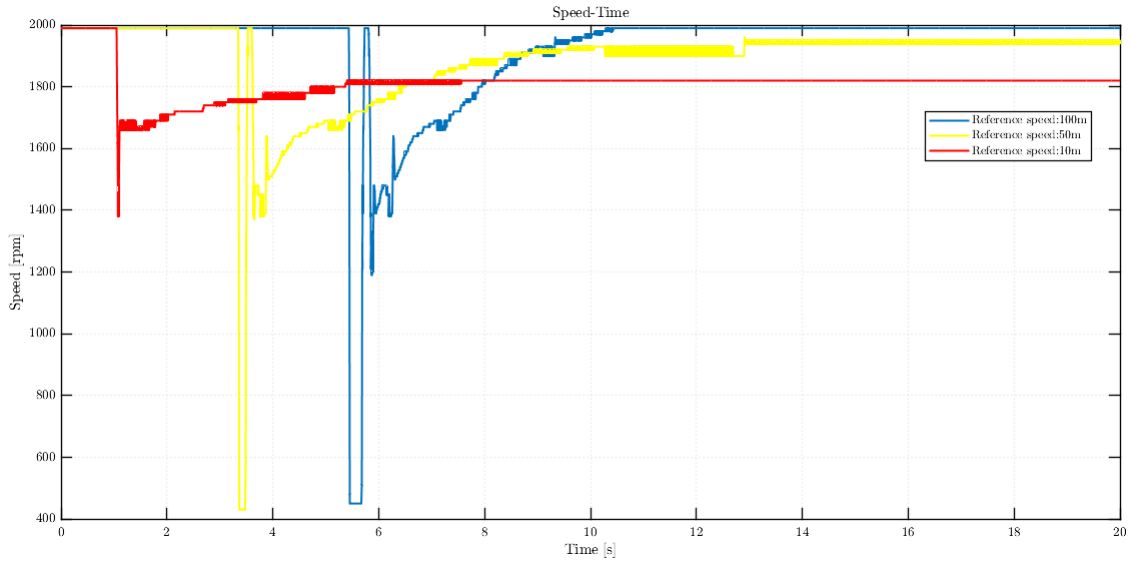


Figure 5.12: Comparison between reference speed with different working altitude

that the power peak remains unchanged for all the working condition and it is reached in the first moments of flight in which the maximum acceleration to the maximum speed is required from the motors (figure 5.13). The difference between the power required in different working conditions are after reaching the maximum speed, so after the power

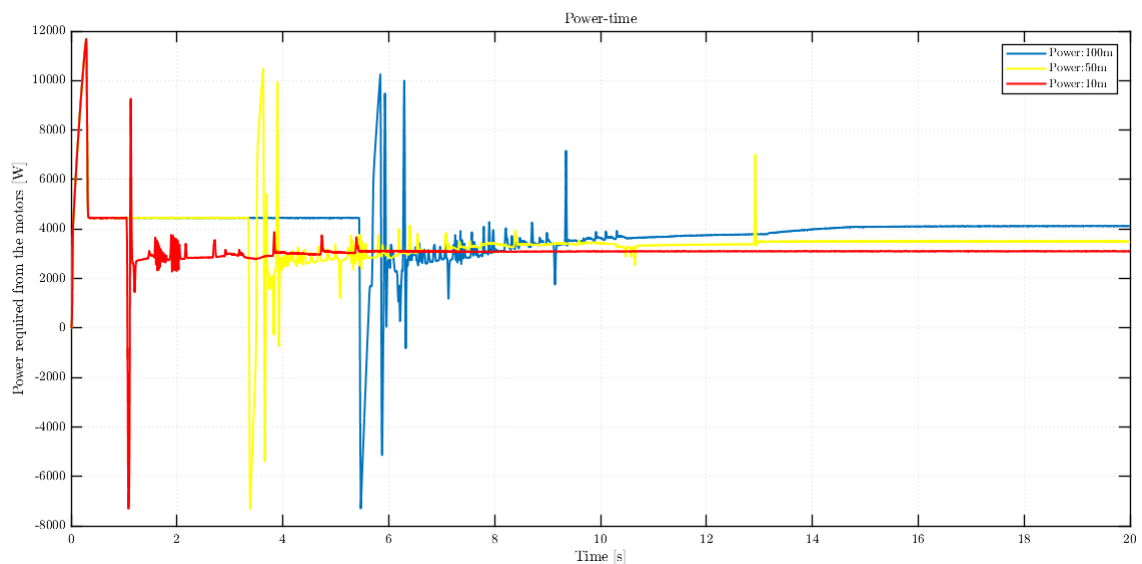


Figure 5.13: Comparison between required power with different working altitude

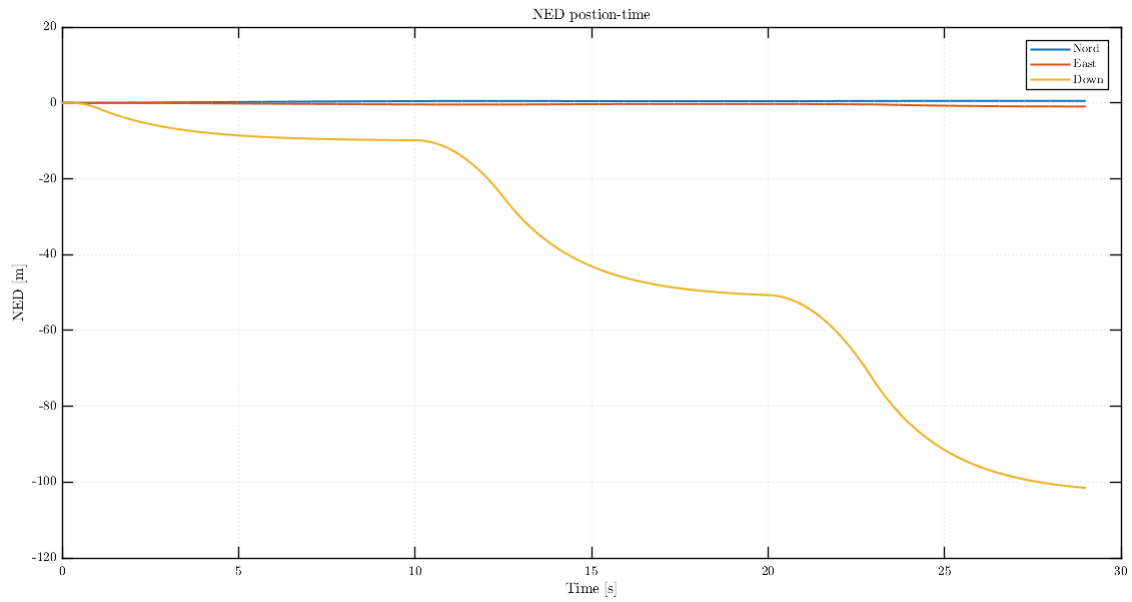


Figure 5.14: Dynamic response to variable NED input

peak. In the case of -100m Down, as desired position, the maximum speed is kept constant for a longer period than other cases which means a longer constant power range after the power peak.

Then, in relation on the required thrust decided by the autopilot, the power is modulated in different ways, but they tend asymptotically to the value of steady state power.

	Maximum Power	Power at Hover	Measurement Unit
<i>50m altitude</i>	11680	3500	W
<i>100m altitude</i>	11680	4125	W

Table 5.2: Power results summary

To conclude this chapter is simulated the performance of the vehicle for 30s with constant North and East reference, as in the previous case, and the Down reference which is -10m for first 10s, -50m for the following 10s and -100m till the end (figure 5.14).

Also with this input the dynamic performance is good.

# Chapter 6

## Power Supply System

The power supply system is composed by three main blocks: the ground power supply, the power supply cable and the aerial power system.

In the ground power supply, we have a power generator or a grid connection and an ACDC converter.

In the aerial power system, we have a DCDC converter which feeds the 48V DC link of the ESC and the step down converter that supply the 12V DC link of the autopilot, the sensors etc.

Regarding the maximum power that can be used by the air system we consider the power required by the propulsion system plus the power required by the sensors and by the autopilot, this power is estimated at around 12000W. This is the power worst case and for this reason the cable and the DCDC converter, must be sized for this power value.

### 6.1 Voltage Level for Power Transmission

The voltage level of the power transmission is a crucial choice for the power supply system of this kind of drone. Because in order not to strongly affect the payload capacity of the drone the cable is wanted as light as possible which means thin cable. To have a thin cable high-voltage supply is needed because it reduces the circulating current according to the ohm law  $P = V \cdot I$  (figure 6.1); lower current means also lower joule losses since they have a quadratic proportionality:  $P_{Joule} = R \cdot I^2$ .

On the other hand the use of high-voltage involves the use of a step-down converter aboard the UAV [13].

The worst side effects of thin cable and high-voltage power transmission are mainly two, related one to the cable thickness and one to the voltage level:

- High resistive losses produced by the small section of the cable, because thinner sections has bigger resistivity;

- Big weight and big dimension of the on-board power electronics, caused by high-voltage which affects power switches mechanical features;

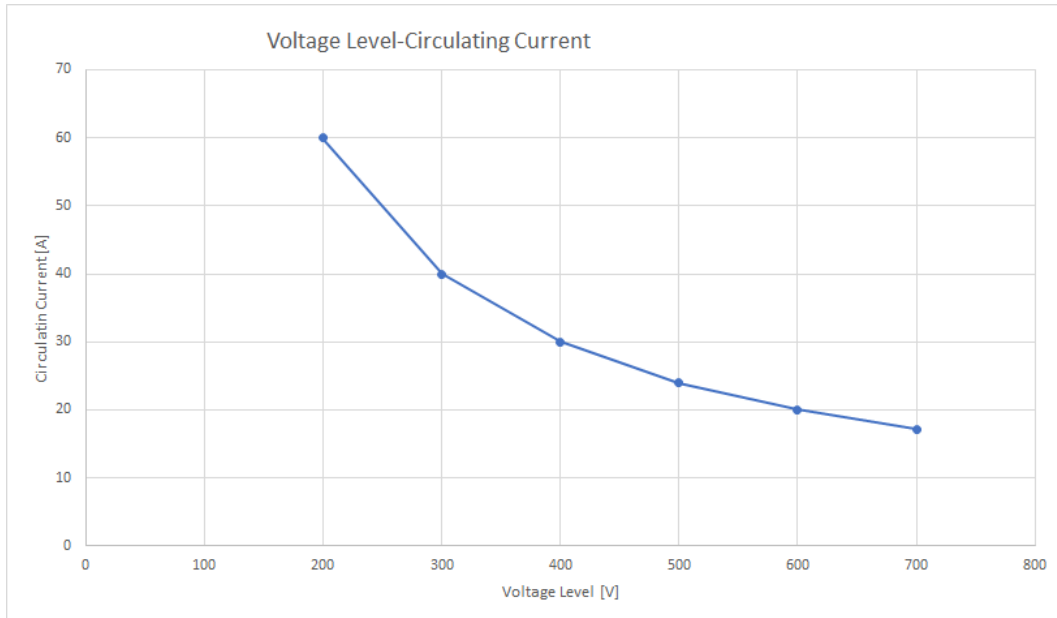


Figure 6.1: Current circulating in the cable with different voltage levels

So, it is searched a trade-off voltage which allows for lower weights in the cable and in power electronics on board and lower losses.

## 6.2 On-Off Board Power Electronics

### 6.2.1 On-Board Power Electronics

#### DCDC Converter

About the on-board power electronics the most important feature is the weight. In fact, on aerial application and in particular for the drone the weight have an high importance, because it affect the payload capacity and the power consumption.

Due to the great powers involved the classic DCDC converters cannot be used because they have too high weights. Consider that the typical weight of a DCDC converter for 12kW with input voltage at 400V-600V has a weight of about 20kg, which is too high for our application.

For this reason, after extensive research on products available on the market the choice is fell on resonant converter.

Resonant converter works at high operating frequency which allows to reduce the size of

the reactive components. The DCDC converter chosen is the BCM6123xD1E5135yzz produced by Vicor. This is a high efficiency isolated fixed ratio DCDC converter which is modular and can operate in parallel with other converter of the same family for manage high power applications.

Note the maximum power allowed by the converter (table 6.1), for the required power

Attribute	Notes	Min	Max	Unit
<b>Electrical specifications</b>				
<i>Primary Input Voltage Range (Continuous)</i>	-	260	410	V
<i>Transformation Ratio</i>	$K = V_{secDC}/V_{priDC}$	1/8	-	-
<i>Secondary Output Current (Continuous)</i>	-	-	35	A
<i>Secondary Output Power (continuous)</i>	Specified at $V_{priDC}=410V$	-	1750	W
<i>Switching Frequency</i>	Frequency of the output voltage ripple = $2x F_{SW}$	1.05	1.14	MHz
<b>Mechanical specifications</b>				
<i>Lenght</i>	-	62.96	63.72	mm
<i>Width</i>	-	22.67	22.93	mm
<i>Height</i>	-	7.11	7.31	mm
<i>Weight</i>	-	-	41	g

Table 6.1: Electrical and mechanical specifications of BCM6123xD1E5135yzz

is needed an array of seven BCM converter, which means a total weight of 287g. In terms of weights this solution is very good especially when compared to a classic PWM converter solution where the weighs would have exceeded 20kg.

The working principle of the resonant converter is to move energy from the primary to the secondary thanks to a high frequency resonant tank. Due to the high operating frequency a small value of capacitance in the primary and secondary stages is enough for full functionality and for reaching high power density (figure 6.2). Thanks to the great advantage in terms of weight, compared to other converters, the voltage level for power transmission is set by the maximum allowable input voltage of the converter, which is 410Vdc. However, by increasing the voltage to use a cable less often it would not get a similar advantage in weighing.

The BCM converter provide a stable DC bus voltage on the aerial vehicle which is used to supply the Electronic Speed Controller (ESC) of each motor and the DCDC converter for feeding the on-board equipment, the ESC and DCDC converter specifications are reported in table 6.2 and 6.3 .

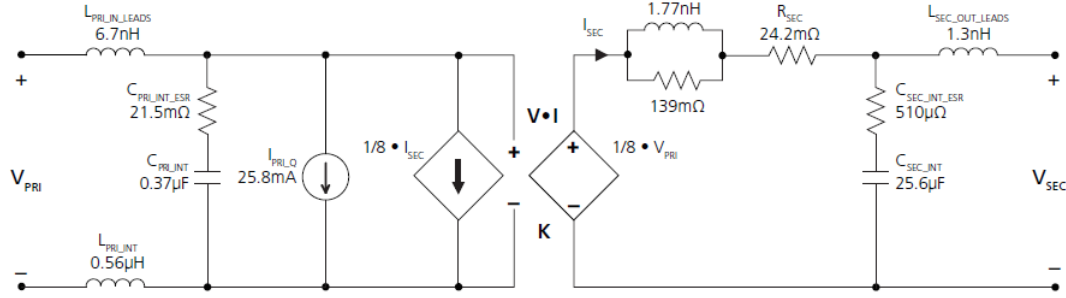


Figure 6.2: Simplified model of the BCM

**ESC**

Model	Continuous Current	Voltage Range	Weight
FLAME 180A HV	180A	22.2V-51.8V	139g

Table 6.2: ESC electrical and mechanical specifications

**DCDC converter**

Model	Input Voltage	Output Voltage	Power	Weight
DCM3632x75H13C2yzz	36-75V	12V	320W	24g

Table 6.3: DCDC converter for on-board equipment electrical and mechanical specifications

**6.2.2 Off-Board Power Electronics**

The power electronics off-board consists in a generator that receives input voltage from the grid and transforms it into DC voltage at 410Vdc to be transmitted to the drone. The TDK Genesys fits well all the specification required.

**ACDC converter**

Model	Input Voltage	Output Voltage	Power
Genesis 3U 15kW	230VAC	150-1500VDC	15kW

**6.3 Cable Sizing**

The first step to size the cable is the to evaluate the maximum current that can circulate in it.

$$I_b = \frac{P_{max}}{V_{DC}} = \frac{12000}{410} = 29.2 \tag{6.1}$$

Calculated the maximum current that the cable must be able to carry out, proceed with the sizing of the cable according to CEI-UNEL 35024/1 and the CEI 64-8 standards.

Once a cable has been chosen:

- Check that the operating current is lower than the cable capacity(CEI-UNEL standard 35024/1):  $I_z > I_b$ ;
- That the voltage drop along the cable is less than 4% (CEI standard 64-8):  $\Delta V < 4\%$ ;

However since the DCDC converter has a wide input range the second condition is not very important.

The choice of the cable for the given the application, must also consider the weights that has to be as small as possible. The cable chosen is a specific cable for tethered drone produced by a Chinese manufacturer (Hefei Haoxiang Intelligent Technology Co., Ltd.) and the cable model is 1B6X1.2. This cable is composed by 6 cores and one optical cable (figure 6.3). This cable is very suitable for the application of the project because

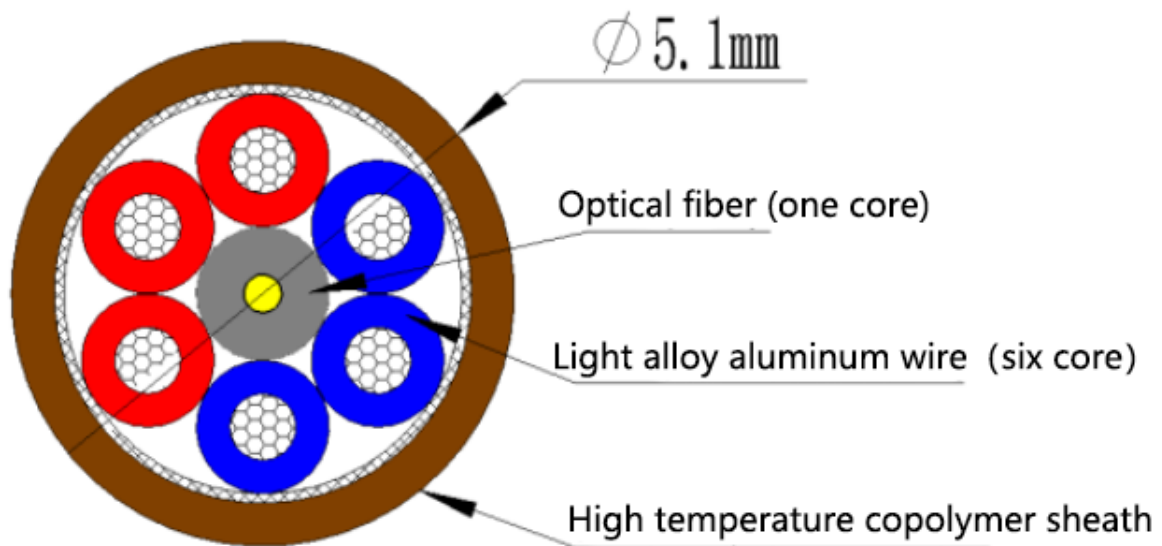


Figure 6.3: 1B6X1.2 cable section

it has small external diameter, light weight, resistance to aging, mechanical resistance, resistance to chemical corrosion and ease of use. In particular in order to have the lower weight as possible the core is made in aluminium which is lighter than copper. The mechanical and electrical specifications of the cable are reported in table 6.4.

Once the cable has been chosen, it is necessary to see if the sizing criteria of the CEI-

<b>Mechanic Specifications</b>	<b>Value</b>	<b>Unit</b>
<i>Structure</i>	6 power core and one core optical fiber	-
<i>Material</i>	Aluminium alloy wire	-
<i>Single core Section</i>	1.2	mm <sup>2</sup>
<i>Insulation</i>	EPR	-
<i>External Protection Layer</i>	Aviation reinforcement fiber	-
<i>Outer diameter</i>	5.8	mm
<i>Weight</i>	85	g/m
<b>Electrical Specifications</b>		
<i>Rated Voltage</i>	1000	VDC
<i>Equivalent DC Resistance of 3 cores at 20°</i>	0.005	Ω/m
<i>Insulation Resistance</i>	500	MΩ
<i>Carrying capacity</i>	40	A

Table 6.4: Mechanical and electrical specifications of the cable

UNEL 35024/1 and CEI 64-8 standards are met.

To verify that  $I_z > I_b$  also in the worst temperature condition is needed a correction factor for the carrying capacity: with a EPR insulating sheath at a temperature of 45° (which is supposed to be the worst temperature) the correction factor is 0.87.

$$I'_z = KI_b = 0.87 \cdot 40 = 34.8A \quad (6.2)$$

$$I'_z > I_b$$

The first condition is verified.

Also the second condition, concerning the voltage drops on the line, must be traced back to the worst case of temperature.

$$\Delta V = \frac{P_{max} \cdot R_{45^\circ}}{V_{DC}^2} \quad (6.3)$$

Where the resistance at 45° is calculated as:

$$R_{45^\circ} = R_{20^\circ} \cdot (1 + \alpha(\Delta T)) = 0.05 \cdot (1 + 0.004(45 - 20)) = 0.55\Omega \quad (6.4)$$

where:

$\alpha$ —Is a temperature coefficient;

So the drop voltage is:

$$\Delta V = \frac{P_{max} \cdot R_{45^\circ}}{V_{DC}^2} = \frac{12000 \cdot 0.55}{410^2} = 0.039 \quad (6.5)$$

$$\Delta V < 4\%$$

The voltage drop is 3.9%, so also the second condition is verified. Anyway, as said previously this requirement is not very important because the DCDC converter aboard has a wide range of input voltage. Furthermore, this condition has been designed for power lines in which the voltage drop from the power supply node to the delivery point must not exceed a certain limit in order not to cause problems to the end user equipment. In any case, to ensure that the desired voltage of 410V always arrives on the on-board converter, a 4% increase can be set in the ground converter to compensate for voltage drops. Therefore the output voltage from the ground station will be:

$$V_{output} = V_{DC} + 0.039V_{DC} = 410 + 16 = 426V \quad (6.6)$$

Since the generator on the ground can supply up to 1500V of voltage there are no problems in providing this compensation.

# Chapter 7

## Safety System

In this chapter are analyzed the calibration of the protections in case of short-circuit of the power supply and the dimensioning of the back-up battery to allow a safe landing. The circuit breaker against over-current is mounted on board the UAV.

### 7.1 Short-Circuit Protection

One of the most important requirements in terms of safety for the product is the protection of the cable both to guarantee its regular operation and to avoid damage to persons and property. The CEI 64-8 standard define the features of the protection against:

- Overload;
- Short circuit;

#### 7.1.1 Overload Protection

The standard CEI 64-8/3 expect that each electrical system is equipped with protection devices that intervene when the circulating current is such as to cause heating and therefore damage to the insulation of the cable.

To guarantee the protection against overloads the following two rules must be verified:

$$1. I_B \leq I_n \leq I_Z$$

$$2. I_f \leq 1.45I_Z$$

where:

$I_B$  – Operating current of the circuit;

$I_n$  – Rated current of the circuit-breaker;

$I_Z$  – Carrying capacity of the cable;

$I_f$  – Safe circuit-breaker operating current;

The first rule is needed to satisfy the overload protection conditions. The second rule is always verified because  $I_f \leq 1.45I_n$  and must be checked only if the protection device is a fuse.

After specifying the conditions of the standard, a switch is selected. The choice falls on the A9N61535 circuit breaker provided by Schneider Electric. The type C intervention

Electrical Specifications	Value	Unit
<i>Model</i>	A9N61535	-
<i>Poles Number</i>	2	-
<i>Rated Current</i>	32	A
<i>Current Type</i>	DC	
<i>Release technology</i>	Magneto-thermal	-
<i>CEI 64-8 Curve Type</i>	C	-
<i>Breaking Capacity (at 440V)</i>	10	kA
<i>Rated voltage</i>	500	VDC

curve in CEI 23-3 standard has a intervention threshold between  $5I_n \div 10I_n$  (figure 7.1).  
Verification of the first condition:

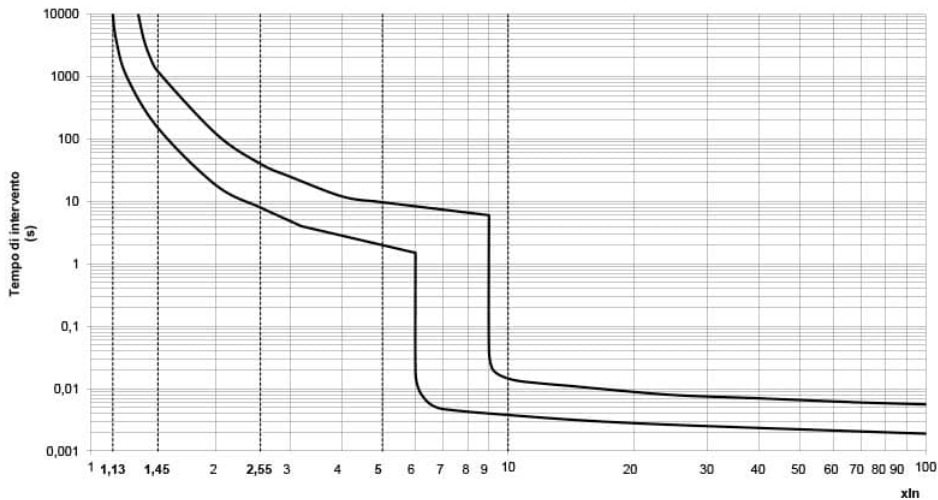


Figure 7.1: Intervention range of the C curve

$$I_B \leq I_n \leq I_Z$$

$$29.26A \leq 32A \leq 34.8A \quad (7.1)$$

This condition is verified.

### 7.1.2 Short Circuit Protection

CEI 23-3 standard expect for the protection against short circuit that are verified the following conditions:

1.  $I_B \leq I_n$ ;
2.  $I_{sc} \leq I_{sc,n}$ ;
3.  $I^2t \leq K^2S^2$ ;

where:

$I_{sc}$  – Presumed short circuit current at the installation point;

$I_{sc,n}$  – Rated breaking capacity of the switch;

$K$  – Cable constant related to the conductor and insulation material;

$S$  – Cable section;

$t$  – Total duration of the interruption;

The first condition is verified from the overload protection instead the others allow the short-circuit current to be interrupted regardless of where the fault occurs, also preventing the insulators from taking excessive temperatures and being damaged.

Short circuit current at the installation point is calculated as:

$$I_{sc} = \frac{V_{DC}}{R_{cable}} = 820A \quad (7.2)$$

Since the rated breaking capacity of the switch is 10 kA the second condition is checked, and the system is protected in the event of a short circuit at any point on the cable.

The third condition allows to verify that the device intervenes in such a way that all the currents caused by a short circuit that occurs in any point of the circuit are interrupted in a time not exceeding that which leads the conductors to the maximum admissible temperature. In order to verify this condition it is necessary that, for each possible short circuit value, the specific energy passing from the interruption device ( $I^2t$ ) is less than the specific short-circuit energy that can be tolerated by the cables ( $K^2S^2$ ).

For the constant K the value relative to an aluminium conductor with EPR insulation was taken, which is: 87. The total duration of the interruption can be extrapolated from the curve in figure 7.1.

$$I^2t = 1344As^2$$

$$K^2S^2 = 10899As^2$$

So, the condition  $I^2t \leq K^2S^2$  is verified. Having verified the condition for the short-circuit current at the beginning of the line, which is the maximum one, the condition is verified for short circuits in each point of the cable.

## 7.2 Backup Battery Sizing

In case of overload or short circuit the tethered UAV remains without power. For this reason, for people safety, it is necessary a backup battery on board.

In order not to burden the maximum power required by the drone, the batteries are recharged on the ground or during the hover phase. In both cases the power used by the UAV is far from the maximum power so the battery can be recharged without over-sizing the cable and on-board and overboard converters.

To check the amount of energy and the amount of power required by the air system to land, a simulation was done in which the UAV climbed up to maximum height and then landed (figure 7.2). From the simulation of these trends are obtained the powers required

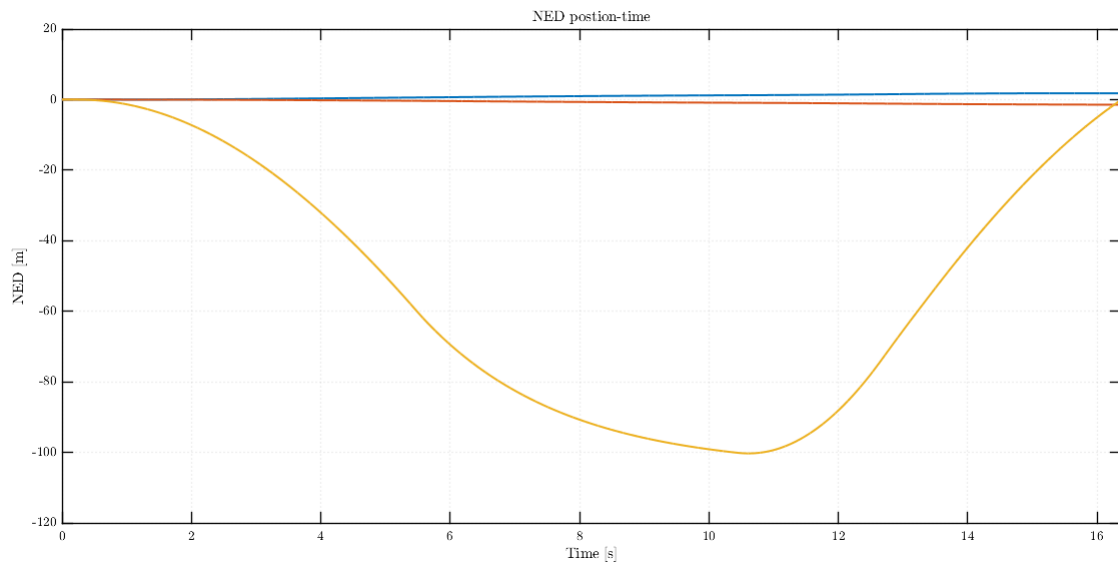


Figure 7.2: Position trend from 0m to 100m and from 100m to 0m

by the quadcopter and then the energy necessary to land the drone starting from a maximum altitude of 100m. The figure 7.2 shows the landing time is around 6 seconds.

The power peak as in the previous simulation is 11680 W, which means that with the electronic on-board power consumption the backup battery has to supply 12000W of power peak.

The mean power during the landing phase from 100m to 0m is 3479W (figure 7.3). Known the average power and the descent time of the drone it is possible to calculate the energy needed for landing.

$$E_{landing} = P_{mean} \cdot \Delta t = 20772Ws \quad (7.3)$$

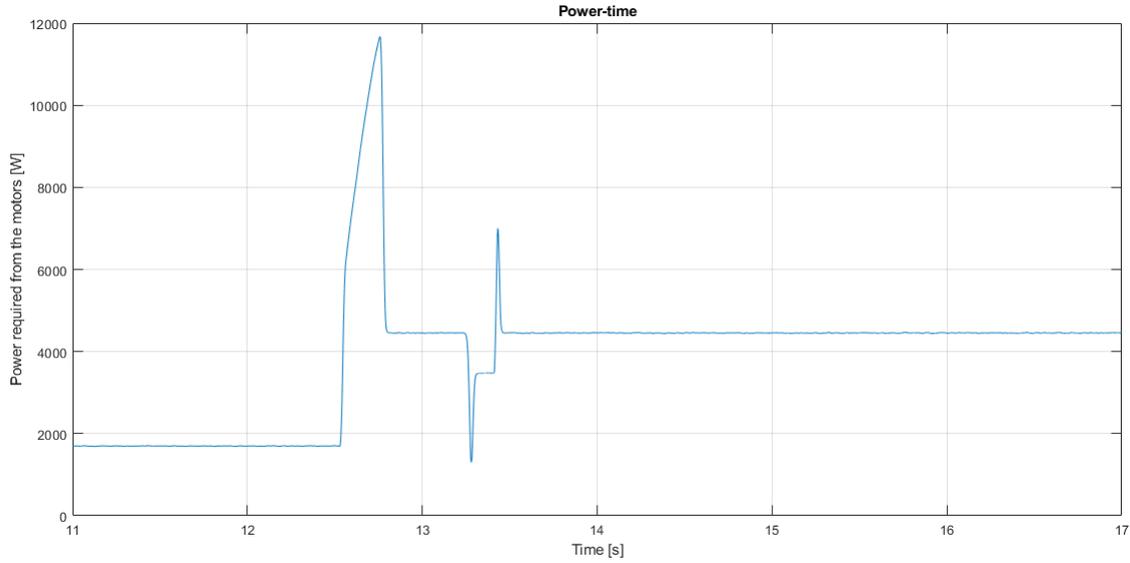


Figure 7.3: Power consumption for the landing phase

To transform the amount of energy in standard measure units the  $Ws$  are divided by 3600 thus obtaining  $Wh$ .

$$E'_{landing} = \frac{E_{landing}}{3600} = 5.77Wh \quad (7.4)$$

Fixed the amount of power and energy required we can size the battery pack.

In order not to exceed the costs and weights of the system we want to realize a battery pack such that it has a voltage of 48V. In this way it can supply the motors and the DCDC converters for the on-board equipment without an additional conversion stage. To realize this voltage level are required:

$$n_{cell} = \frac{48}{3.7} = 13 \quad (7.5)$$

Set to 3.7 V as nominal voltage of a single cell are needed 13 cells in series to realize the desired level voltage.

The desired cell is searched on the cell's catalogue of Kokam, which is a leader of the market for battery solutions. The ideal cell is characterized by the high-power density and by the low weight. The best product founded on catalogue are:

Model	Capacity at 1C [Ah]	C-Rate [C]		Weight [kg]
		Continous	Pulse	
SLPB78205130H	16	8	16	0.395
SLPB98188216P	30	20	30	0.78

From this specifications we can evaluate the power that can be delivered by each cell

in continuous mode and in pulse mode:

$$P_{s1} = Capacity \cdot C_{Rate_{cont}} \cdot V_{nom} \quad (7.6)$$

$$P_{s3} = Capacity \cdot C_{Rate_{pulse}} \cdot V_{nom} \quad (7.7)$$

The SLPB98188216P has a higher power both in continuous service and in intermittent.

Results	SLPB78205130H	SLPB98188216P	Unit
Power in S1	473	2220	W
Power in S3	888	3330	W
Cell duration in S1	7.5	3	min
Cell duration in S3	4	2	min

The fixed number of cells is thirteen in order not to use a further DCDC converter to supply power to the motors. So from this conditions each cell of the battery pack must be able to provide:

$$P_{pulse-single-cell} = \frac{P_{peak}}{13} = 923W \quad (7.8)$$

$$P_{cont-single-cell} = \frac{P_{cont}}{13} = 343W \quad (7.9)$$

The power peak in pulse mode and the maximum continuous power are shown in figure 7.3.

The cell SLPB98188216P is over sized for this application but it satisfies well the power requirements. A pack made with SLPB98188216P cells has a total weight of 10.14kg. The cell SLPB78205130H it does not completely satisfy the power requirements in fact, it meets the demand for power continuously but cannot work up to peak power in pulse mode. The weight of this cell is lower than the previous one and as for all the components of the drone the weights are very important. For this reason, the SLPB78205130H cell was chosen.

To fully satisfy the peak power requirement it was added another cell in parallel to the last one, with this solution the total voltage remains 48V, but the pack capacity is increased, the power request for each cell becomes:

$$P_{pulse-single-cell} = \frac{P_{peak}}{14} = 857W \quad (7.10)$$

Which is lower than the cell limit in continuous operating power.

The flight time with this battery pack 38 times higher than the required one therefore also in case of emergency the drone is able to remain in the air a much higher amount of time than the one required to land, this in order to have a precautionary margin in case of landing time increase.

# Chapter 8

## Conclusions and Future Developments

### 8.1 Thesis Results

This project presented a feasibility analysis for the propulsion system of a tethered UAV. Results that it is possible.

Propellers and motors sized to fulfil all the requirements in terms of thrust, torque, speed and power. Thanks to the propulsion system designed the dynamic of the drone is excellent at all altitudes and even the ascent to the maximum height of 100m is carried out in a few seconds.

The motor system coupled to the propeller has been designed in such a way as to minimize the demand for power, increasing the size of the blade but paying attention to the inertia of the system to maintain a fast response from the engine.

As a matter of reliability, all the components of the propulsion system have been sized to work continuously in worst case condition.

The motor simulation shows the large torque ripple which the BLDC motor was subjected to, when it was driven by the trapezoid control technique. This problem was solved by implementing a control technique based on hysteresis current regulators which has greatly reduced the ripple of torque making them acceptable.

The power transmission system was also designed to complete the project. This includes the ACDC converter in the ground station, the cable and the DCDC converter in the vehicle to power the DC link of the drone.

The choices made in this phase were all aimed at meeting the required power requirements being careful not to exceed the weights, which are essential for an aerial vehicle. And thanks to the choice of voltages, components and technologies available on the market, a light and performing power transmission system has been obtained.

Safety devices have also been dimensioned together with the power transmission system. To ensure prompt intervention in the event of a short-circuit on the power supply cable,

a circuit breaker has been inserted on the UAV and a back-up battery has been dimensioned to ensure a safe landing in the event of protection tripping.

## **8.2 Future Development**

The project foresees the next development of a more complex model of the cable. In fact, in the current situation the cable is always considered taut and with only the weight force applied to the UAV. In parallel to my thesis project another member of the project team is working, precisely, on the realization of a model that simulates a more complex cable model, which takes into account the weight force and wind force.

The ultimate goal will be to create a cable control system that considers all the incoming forces and manages a winch to keep the cable taut.

# Bibliography

- [1] G. Wang and S. Wang, “Heavy Payload Tethered Hexarotors for Agricultural Applications: Power Supply Design,” *International Research Journal of Engineering and Technology*, pp. 2395–56, 2015.
- [2] J. T. Mfiri, J. Treurnicht, and J. A. Engelbrecht, “Automated landing of a tethered quad-rotor UAV with constant winching force,” *2016 Pattern Recognition Association of South Africa and Robotics and Mechatronics International Conference, PRASA-RobMech 2016*, pp. 1–6, 2017.
- [3] P. G. Ioppo, *The Design, Modelling and Control of an Autonomous Tethered Multi-rotor UAV*. PhD thesis, University of Stellenbosch, 2017.
- [4] D. Santamaria, K. Kondak, L. A. Sandino, A. Viguria, M. Bejar, and A. Ollero, “First experimental results on enhancing hovering performance of unmanned helicopters by using a tethered setup,” *Robotics and Autonomous Systems*, vol. 79, pp. 147–155, 2016.
- [5] T. J. Nugent, Jr. and J. T. Kare, “Laser power beaming for defense and security applications,” *Unmanned Systems Technology XIII*, vol. 8045, no. May 2011, p. 804514, 2011.
- [6] S. Lupashin and R. D. Andrea, “Stabilization of a Flying Vehicle on a Taut Tether using Inertial Sensing,” *2013 IEEE/RSJ International Conference on Intelligent Robots and Systems*, pp. 2432–2438, 2013.
- [7] S. Kiribayashi, J. Ashizawa, and K. Nagatani, “Modeling and design of tether powered multicopter,” in *SSRR 2015 - 2015 IEEE International Symposium on Safety, Security, and Rescue Robotics*, no. July, IEEE, 2016.
- [8] D. Hedlund, M. Senkovski, and J. Brynolf, *MOTOR SYSTEM DESIGN FOR LARGE UAV Examiner: Mikael Ekström*. PhD thesis, Malardalen University, 2017.
- [9] F. Mahmuddin, “Rotor Blade Performance Analysis with Blade Element Momentum Theory,” *Energy Procedia*, vol. 105, pp. 1123–1129, 2017.
- [10] M. Cutler, N.-K. Ure, B. Michini, and J. How, “Comparison of Fixed and Variable Pitch Actuators for Agile Quadrotors,” 2013.
- [11] R. Krishnan, “Application Characteristics of Permanent Magnet Synchronous and Brushless dc Motors for Servo Drives,” *IEEE Transactions on Industry Applications*, vol. 27, no. 5, pp. 986–996, 1991.
- [12] C. L. Xia, *Permanent Magnet Brushless DC Motor Drives and Controls*. 2012.

- [13] S. Kiribayashi, K. Yakushigawa, and K. Nagatani, “Design and Development of Tether-Powered Multicopter Micro Unmanned Aerial Vehicle System for Remote-Controlled Construction Machine,” pp. 637–648, 2017.